

Integrated Mapping of Rare Earth Element Mineralization Using Hyperspectral Imaging and Laser Induced Fluorescence Spectroscopy in Drill Cores from the Storkwitz Carbonatite, Germany

Aditya Easwaran Krishnan



HiF

HELMHOLTZ INSTITUTE FREIBERG
FOR RESOURCE TECHNOLOGY

 **TU Delft**

Integrated Mapping of Rare Earth Element Mineralization Using Hyperspectral Imaging and Laser Induced Fluorescence Spectroscopy in Drill Cores from the Storkwitz Carbonatite, Germany

By

A.E. Krishnan

in partial fulfilment of the requirements for the degree of
Master of Science
 in Applied Earth Sciences
 of the European Mining, Minerals and Environmental Programme
 at the Delft University of Technology,
 to be defended publicly on August 03, 2023

Supervisor	:	Dr. T. Schmiedel	TU Delft
Thesis committee	:	Dr. T. Schmiedel, Dr. M.W.N. Buxton, Prof. Dr. B. Lottermoser, Dr. J. Leveinen	TU Delft TU Delft RWTH Aachen University Aalto University
Advisors	:	Dr. M. Kirsch, Dr. S. Lorenz, Dr. M. Fuchs	Helmholtz Institute Freiberg Helmholtz Institute Freiberg Helmholtz Institute Freiberg

An electronic version of this thesis is available at <http://repository.tudelft.nl/>.

Preface

This thesis presents the results of research conducted by Aditya Krishnan on the integrated mapping of rare earth element mineralization using hyperspectral imaging and laser induced fluorescence spectroscopy in drill cores from the Storkwitz Carbonatite, Germany. The research was conducted under the supervision of Tobias Schmiedel (TU Delft), and Moritz Kirsch, Sandra Lorenz, and Margret Fuchs (Helmholtz Institute Freiberg) in Freiberg, Germany. This research was completed as a requirement for the degree in Master of Applied Earth Sciences (European Mining Course) at TU Delft.

Title	:	Integrated Mapping of Rare Earth Element Mineralization Using Hyperspectral Imaging and Laser Induced Fluorescence Spectroscopy in Drill Cores from the Storkwitz Carbonatite, Germany	
Author	:	Aditya Krishnan	
Date	:	03-08-2023	
Supervisor	:	Dr. T. Schmiedel	TU Delft
Thesis committee	:	Dr. T. Schmiedel, Dr. M.W.N. Buxton, Prof. Dr. B. Lottermoser, Dr. J. Leveinen	TU Delft TU Delft RWTH Aachen University Aalto University
Advisors	:	Dr. M. Kirsch, Dr. S Lorenz, Dr. M. Fuchs	Helmholtz Institute Freiberg Helmholtz Institute Freiberg Helmholtz Institute Freiberg
Address	:	Section of Resource Engineering Department of Geosciences & Engineering Delft University of Technology Stevinweg 1 2628CN Delft The Netherlands	

*All rights reserved.
No parts of this publication may be reproduced,
Stored in a retrieval system, or transmitted,
In any form or by any means, electronic,
Mechanical, photocopying, recording, or otherwise,
Without the prior written permission of the
Section for Resource Engineering*

Acknowledgments

I would like to express my sincere gratitude to my academic supervisor, Tobias Schmiedel, for his unwavering support, valuable feedback, and continuous guidance throughout the entire duration of my masters thesis. His encouragement and insights have been instrumental in shaping the direction and success of this project. I would also like acknowledge my supervisors at the institute, Moritz Kirsch, Sandra Lorenz, and Margret Fuchs, for their invaluable feedback, expert guidance, and generous help. Their insights and discussions have enriched the research process and added depth to the final outcomes. Without everyone's support this project would not have been completed in time.

I am deeply grateful to everyone in the exploration department at Helmholtz Institute Freiberg, especially Sam Thiele, Laura Tusa, René Booyesen, and Filipa Simões for all their support and encouragement. I would also like to extend my thanks to Erik Herrmann for his help in acquiring the hyperspectral data and Titus Abend for his help in calibrating and performing the laser induced fluorescence measurements. I would like to thank the Saxony State Office for Environment, Agriculture and Geology (LfULG) for providing access to the Storkwitz cores.

My heartfelt thanks go out to my family for their encouragement throughout this academic journey. I also want to express my gratitude to all my friends, especially those in my EMC cohort, for their unwavering support, motivation, and camaraderie throughout my masters journey. I would particularly like to acknowledge Sibren Dieters for being an exceptional colleague and a dear friend throughout this entire project.

To all those mentioned above and countless others who have contributed to my growth and development during this time, your support has been immeasurable.

Table of Contents

List of Figures	8
List of Tables	9
Abstract	10
Chapter 1 – Introduction	11
1.1 Project Specifications	14
Chapter 2 – Instrumentation & Technique Background	15
2.1 Hyperspectral Imaging (HSI) Spectroscopy	15
2.1.1 Spectral Properties of Minerals	16
2.1.2 Previous Research and Toolboxes	19
2.2 Laser Induced Fluorescence (LiF) Spectroscopy	20
2.2.1 Behavior of REEs in LIF	20
2.2.2 Previous LiF Research and Combined Approach	23
Chapter 3 – Geological Setting	24
3.1 Regional Geology	24
3.2 Geology and Magmatic Evolution of the Delitzsch complex	25
3.3 Exploration History	26
3.4 Previous Research on SES 1/2012 Drill core	27
Chapter 4 – Methods	30
4.1 SEM-MLA Data Acquisition	31
4.2 Hyperspectral Data Acquisition	31
4.2.1 HSI Data Pre-Processing	33
4.3 Band Ratios	34
4.4 Minimum Wavelength Mapping for Hyperspectral Data	34
4.5 Endmember Extraction & Library Creation	35
4.6 Spectral Unmixing	37
4.7 Spectral Angle Mapping (SAM) Algorithm	38
4.8 Selection of Samples for LiF Measurements	38
4.9 LiF Data Acquisition	38
4.9.1 LiF Data Pre-Processing	40
4.10 Minimum Wavelength Mapping for LiF Spectroscopy Data	40
4.11 Validation	41
4.12 Proposed Workflow Overview	41
Chapter 5 – Results & Interpretations	44
5.1 Sample Block MLA Mineralogical Results	44

5.2	PCA and Elbow Plot Results	46
5.3	Selected Endmembers for Each Dataset	48
5.4	Fe-Oxide Band Ratio Map	53
5.5	Hyperspectral MWL Maps	54
5.5.1	Nd MWL Map	55
5.5.2	Al-OH Feature MWL Map	55
5.5.3	Quartz – Plagioclase – Aegirine – Mica MWL Map	56
5.5.4	Carbonate MWL Map	57
5.6	Abundance Maps from Spectral Unmixing	57
5.7	SAM mapping	59
5.8	Validation	59
5.9	Spectral Characterization of Storkwitz Breccia	62
5.10	Laser Induced Spectroscopy of Storkwitz Samples	65
5.10.1	Peak Detection	65
5.10.2	Minimum Wavelength Mapping for LiF data	70
	Chapter 6 – Discussion	73
6.1	Discussion About the Storkwitz Carbonatite.	73
6.2	Features and Limitations of Proposed Workflow	79
	Chapter 7 – Future Outlook	82
7.1	Recommendations	83
	Chapter 8 – Conclusions	84
	Appendix	85
	References	86

List of Figures

Figure 2.1: Position of most characteristic REE absorption features in the VNIR range according to the chemical analysis and literature review (from Lorenz et al., 2018).....	18
Figure 2.2: Spectral library plot of common REE -bearing minerals (from Koerting et al., 2021).	18
Figure 2.3: LIF reference spectra obtained with 325 nm, 442 nm, and 532 nm laser excitation with the respective diagnostic emission lines for the REE phosphates (modified from Fuchs et al. 2021).	22
Figure 3.1: (a) Regional overview map of Germany showing the location of the Delitzsch ultramafic complex. (b) Geological map of the Delitzsch area with Cenozoic cover removed (c) Schematic cross-section of the Storkwitz diatreme, RHZ - Rheno-Hercynian zone; SX-TH - Saxo-Thuringian zone; UML - ultramafic lamprophyre (taken from Loidolt et al. 2022; modified from Krüger et al., 2013 and Mockel, 2015)	25
Figure 3.2: Downhole lithological logs for 419–491 m interval with Nb% and REE% based on m-scale geochemical assaying (modified from Ceritech, 2012).	28
Figure 4.1: Sample blocks from the Storkwitz drill cores with available SEM-MLA mineralogical data used for qualitative hyperspectral interpretation.....	30
Figure 4.2: SisuROCK drill core scanner (left) with mounted sensors (right) in the visible to near-infrared and shortwave infrared (VNIR-SWIR), mid-wave infrared (MWIR), and long-wave infrared (LWIR) range.....	32
Figure 4.3: Schematic diagram illustrating the LiF line scanning experimental setup used for data acquisition.....	32
Figure 4.4: First stage of the developed workflow showing the processing steps of the hyperspectral dataset and the resulting outcomes.....	42
Figure 4.5: Second stage of the developed workflow to acquire and process LiF data.	43
Figure 5.1: MLA maps showing the distribution of the 20 mineral classes for the ten thick sections.	45
Figure 5.2: Modal abundances of each mineral class within the ten thick sections.....	46
Figure 5.3: Visualization of the PCA maps for the block sections and the elbow method and silhouette score plots of the block data for each wavelength dataset.	47
Figure 5.4: Pixel locations of the VNIR-SWIR endmembers as well as their respective hull-corrected spectra. (Reflectance spectra for each endmember offset for clarity).....	49
Figure 5.5: Pixel locations of the MWIR endmembers as well as their respective hull-corrected spectra. (Reflectance spectra for each endmember offset for clarity)	51
Figure 5.6: Pixel locations of the LWIR endmembers as well as their respective hull-corrected spectra. (Reflectance spectra for each endmember offset for clarity)	52
Figure 5.7: Band ratio map generated for three iron oxide band ratios utilized in the data.	54
Figure 5.8: Comparison between the REE rich zones in the MWL map generated to the RGB image of the same core piece illustrating the accumulation of REEs in clasts.	55
Figure 5.9: 434 – 437m section of core indicating the fault zone with high mica and clay content.....	56
Figure 5.10: 467-470 m section of core indicating the different clasts associated with quartz, plagioclase, aegirine and mica.	56
Figure 5.11: RGB image of the core piece at 486.4 nm and the corresponding maps short-wave, mid-wave, and long-wave maps to compare the lithologies identified to the ones mapped.	60

Figure 5.12: RGB image of the two core pieces at 454.1 m and 452.9 m and their corresponding long-wave SAM map to verify the quartz, plagioclase, aegirine and biotite mineralogy.	61
Figure 5.13: OWL-SAM maps illustrating the two types of granitoid clasts that are observed.	62
Figure 5.14: 482-485 m section of core indicating the different carbonatitic clasts present in the drill core.	63
Figure 5.15: LiF data based minimum wavelength map across the broad 580 – 900 nm range for the block sections and the core pieces.	66
Figure 5.16: Individual emission spectra for all points identified in the block sections with certain peaks outlined.	67
Figure 5.17: Result of peak detection technique used on the P6 identifying all the possible emission points existing in the spectra.....	68
Figure 5.18: MWL comparison between maps generated for the blocks with LiF data (left) and hyperspectral data (right) for spectral range of 580-900nm along with the MLA mineralogical data of the respective blocks.	69
Figure 5.19: False color images indicating the co-distribution of the three emission peaks as well as the three identified zones. (Yellow – R+G; White – R+G+B)	70
Figure 5.20: LiF minimum wavelength map identifying the peak between 590 – 610 nm range in the blocks and core pieces.....	71
Figure 5.21: LiF minimum wavelength map identifying the peak between 855 – 885 nm range in the blocks and core pieces.....	72
Figure 6.1: LiF 870 nm MWL map for blocks along with spectra from two different peak regions along with the MLA data to illustrate the REE-fluorcarbonate and apatite rich areas.	75
Figure 6.2: LiF 870 nm MWL map of core pieces with the correlating Carbonate MWL map illustrating the dolomitic composition of the two carbonatitic clasts.....	76

List of Tables

Table 4.1: Block samples extracted from the drill core with their depth and associated lithology (from Loidolt et al. 2022).....	31
Table 4.2: Sisurock drill core scanner acquisition parameters for the visible to near-infrared and shortwave infrared, mid-wave infrared, and long-wave infrared range.....	32
Table 4.3: Spectral indices for relevant features for band ratios.....	34
Table 4.4: Spectral ranges used to extract the position and depth of specific absorption features using minimum wavelength mapping.....	35
Table 4.5: Spectral ranges of the specific emission peaks using minimum wavelength mapping techniques.....	42
Table 5.1: All identified endmembers in the VNIR-SWIR, MWIR, and LWIR datasets (Cb: Carbonates, Amp: Amphibole, Bt: Biotite, Qz: Quartz, Aeg: Aegirine, Or: Orthoclase, Ab: Albite, REE-FI: REE-fluorcarbonate, Wm: White Mica). (Abbreviations based on Whitney & Evans, 2010).....	48

Abstract

The growing importance of rare earth elements (REEs) in sustainable technologies necessitates an efficient assessment of potential resource targets within the European Union. Traditional analytical techniques for REE determination have drawbacks like destructive and time-consuming sample preparation, but hyperspectral imaging (HSI) and laser-induced fluorescence (LiF) offer promising alternatives. This project aims to use a combined HSI and LiF method to qualitatively characterize REE mineralization and alteration in drill core samples from the Storkwitz deposit, Germany. The goal is to develop a transferrable mapping approach for REEs, while enhancing our understanding of the Storkwitz deposit. It aims to check the robustness of HSI conducted across the extended wavelength range as a tool in effectively characterizing the lithologies associated with REE mineralization in the Storkwitz breccia. It also tests if the combined HSI-LiF can provide new insights into the presence of REEs and its associated minerals in the Storkwitz breccia.

The proposed workflow involves acquiring hyperspectral data of the Storkwitz drill core and block sections in three wavelength ranges (VNIR-SWIR, MWIR, and LWIR). Automatic and manual endmember extraction is performed on the smaller subsection of data to create spectral libraries, which are then used for spectral unmixing and mapping of the entire hyperspectral dataset to identify lithologies. LiF is used to identify and map rare earth elements (REEs) in selected REE-rich zones identified from the hyperspectral data.

The results indicated that the Storkwitz Breccia is primarily composed of ankerite in the matrix, along with minor amounts of white mica, clay, iron oxides, and REE-fluorcarbonates. The breccia contains different clasts, including granitoid clasts rich in orthoclase and quartz-albite-biotite, as well as carbonatitic clasts dominated by ankerite, dolomite, and ankerite-calcite. The breccia also underwent four alteration phases, including fenitization, biotite alteration, white mica-clay alteration, and ferric alteration. Laser-induced spectroscopy confirmed the presence of REEs, with apatite and REE-fluorcarbonates, particularly bastnäsite, being the main REE-bearing minerals. The specific REEs identified include Nd^{3+} , Sm^{3+} , Pr^{3+} , and possibly Eu^{3+} . The comprehensive workflow combining hyperspectral imaging and laser-induced fluorescence spectroscopy proved to be a successful approach for characterizing lithologies and mapping rare earth element mineralization in the Storkwitz breccia. The study opens up new possibilities for efficient REE exploration in similar geological settings, providing valuable information for geological logging and interpretation.

Chapter 1 – Introduction

Rare earth elements (REE) are necessary components for the production of wide variety of items like glass, ceramics, lasers, superconductors, batteries, and high-strength alloys with vital applications in the aerospace, defense, telecommunications, and medical sectors. Additionally, REEs are also essential for the manufacturing of permanent magnets. These magnets, typically composed of neodymium, iron, and boron (NdFeB), are critical components in electric vehicle motors, wind turbines, computer hard drives, and many other electronic devices. The strong magnetic properties of rare earth elements contribute to the miniaturization and improved performance of these technologies. With their recently growing demand linked to their utilization in current and future green technologies, REEs are important for the progress of society. Following the mounting risks associated with susceptibility to disruption of their supply chains, REEs have been identified as critical materials in the European Union (Critical Raw Materials Resilience Report, 2020). Given the rising importance of REEs for modern civilization focused on sustainability, there is an increased need for efficient assessment of potential resource targets for these materials also within the EU territory.

Geologically speaking, REEs are formed as constituents in a wide range of mineral groups, including phosphates (e.g., monazite and xenotime), carbonates (bastnäsite and synchysite), silicates (e.g. allanite and steenstrupine) and halides (e.g. fluocerite). Carbonatites (typically containing monazite and bastnäsite minerals) and their associated alkaline igneous rocks are considered the most important source of REEs and make for popular targets for mineral exploration companies (Simandl et al., 2018). In this context, some key REE occurrences have been identified and explored across Europe that could be exploited in the future. An example of such an occurrence is the Storkwitz Carbonatite. The Storkwitz carbonatite is characterized by breccias with a fine-grained matrix. It forms part of the Late Cretaceous ultramafic lamprophyre-carbonatite Delitzsch complex, located in Saxony, Germany.

Typically, ICP-MS (Inductively coupled plasma mass spectrometry), ICP-OES (Inductively coupled plasma optical emission spectrometry), NAA (neutron activation analysis), and XRF (X-ray fluorescence) are some of the most commonly used analytical techniques for REE determination in resource programs (Bhatt et al., 2017). While these techniques provide valuable insights into mineralogy and geochemistry, they also pose certain drawbacks. For ICP-MS and ICP-OES methods, the sample must be prepared either using corrosive acids or fusion with fluxes which can be destructive and time-consuming. Alternatively, these techniques must be combined with laser ablation sampling to yield direct analysis of solid samples (Bhatt et al., 2018; Fedorowich et al., 1993). NAA is a highly precise technique for REE analysis, but it requires access to a nuclear reactor and long irradiation time. While XRF can present a convenient direct analysis of solid samples, it is unsuitable for lighter elements (Bhatt et al., 2018). Therefore, the use of a non-destructive and fast analytical method for the detection and mapping of REEs like

hyperspectral imaging (HSI) and Laser-Induced Fluorescence spectroscopy (LiF) can be viable alternatives to these techniques.

Drilling is an integral part for mineral resource assessment. Drill cores provide important information on the structure, size, quality, and value of the deposit as well as samples for chemical, processing, metallurgical, and geotechnical analyses. Drill cores are traditionally characterized through the method of core logging performed by experienced geologists. However, this process can be subjective and time-consuming and for bulk geochemistry data, destructive analytical techniques like ICP-OES, ICP-MS or Fusion-XRF must be performed. Moreover, obtaining drill cores is expensive. Given the high costs, it is important maximize the information gained from available drill cores. Within this context, hyperspectral imaging can be used to rapidly obtain continuous, high-resolution mineralogical data over the entire length of drill cores, adding value to exploration campaigns.

Hyperspectral data is based on the evaluation of radiance data measured in a large number of spectrally continuous bands in the visible and infrared part of the electromagnetic spectrum. Using different hyperspectral sensors, reflected radiance is registered in the visible-near infrared (VNIR), short-wave infrared (SWIR), mid-wave infrared (MWIR) and long-wave infrared (LWIR) ranges. Based on diagnostic spectral signatures within these different spectral ranges, minerals or mineral mixtures can be identified and their spatial distribution and relative abundances can be mapped (Acosta et al., 2021). REE-bearing minerals typically have complex yet diagnostic absorption patterns in the visible to shortwave infrared (Turner et al., 2015). Significant research has been conducted where hyperspectral imaging is used as a tool for characterizing alteration assemblages associated with hydrothermal ore deposits in different magmatic, and sedimentary environments (e.g., Gering et al., 2022; Kruse, 2015, Arne et al., 2016; Wang et al., 2017; Jakob et al., 2016). Hyperspectral data has also been used to characterize REE-bearing rocks (Booyesen et al., 2020; Boesche et al., 2015; Neave et al., 2015). For the Storkwitz carbonatite, only petrographic and geochemical studies have been undertaken (Loidolt et al., 2022; Müller et al., 2021, Niegisch et al., 2022), but there has not been a hyperspectral study, particularly using the extended VNIR-SWIR-MWIR-LWIR wavelength ranges, to map the REE mineralization in drill cores.

An additional sensitive technique to detect and map REEs is laser-induced fluorescence (LiF) spectroscopy. This method involves the excitation of atoms or molecules using laser light and the subsequent emission of fluorescent light which can be detected and analyzed. It is highly suited for REE detection due to the combination of targeted excitation and narrow emission lines, along with the element-specific characteristic features observed in LiF spectra (Fuchs et al., 2021). Kauppinen et al. (2013) showcased the utilization of LiF for mapping drill core samples from the Kevitsa Ni-Cu-PGE deposit containing nickel, copper, cobalt, platinum, palladium, and gold. Seidel et al. (2019) utilized laser-induced fluorescence spectroscopy to map REEs in natural rock samples, but not at drill core scale, and not in combination with reflectance spectroscopy. A combination of HSI and LiF would provide superior sensitivity for the detection of REEs, and a

means of cross-validating data, thus becoming an important tool for drill-core logging in REE exploration.

Due to the reasons outlined above, this project plans to investigate the application of HSI for the qualitative characterization of the REE mineralization and alteration using drill core samples from the Storkwitz deposit. It also plans to implement a combined HSI-LIF mapping approach for REE detection to create qualitative maps of the REE-rich zones. Preexisting geological studies will provide ground truthing of the data acquired using the HSI-LIF approach. Not only does this project test the capabilities of these analytical techniques but also further increase our understanding of mineralization associated with the Storkwitz deposit. In addition, the combined HSI-LIF approach for the mapping of REEs will be transferrable to other carbonatite-hosted REE deposits and may be a useful tool in exploration programs worldwide.

1.1 Project Specifications

Goal: The goal of the project is to develop a workflow utilizing hyperspectral imaging and laser-induced fluorescence spectroscopy to spectrally characterize the lithologies associated with REE mineralization in the Storkwitz breccia using the entire VNIR-SWIR-MWIR-LWIR range and gain insights into the presence of REEs and their association with specific minerals in the Storkwitz Carbonatite.

Objectives: The specific objectives for this project could include:

1. Acquiring and analyzing hyperspectral imaging data across the entire extended wavelength range of the Storkwitz breccia to characterize the lithologies associated with REE mineralization.
2. Acquiring laser-induced fluorescence spectroscopy data using an integrated line scan setup on the selected REE-rich samples to determine the presence of REEs and their mineral associations.
3. Correlating the results from hyperspectral imaging and laser-induced fluorescence spectroscopy to understand the relationship between lithologies, REE distribution, and associated minerals in the Storkwitz breccia.

Research Questions: The study plans to address the following research questions:

1. Can hyperspectral imaging be utilized to spectrally characterize the lithologies associated with REE mineralization in the Storkwitz breccia?
2. Can laser-induced fluorescence spectroscopy be used to determine the presence of REEs in the selected REE-rich samples?
3. What insights can be gained from correlating the results of hyperspectral imaging and laser-induced fluorescence spectroscopy regarding lithologies, REE distribution, and associated minerals in the Storkwitz breccia?
4. What are the implications of the proposed workflow for its application in other similar deposits and the exploration industry overall?

Hypothesis: The hyperspectral imaging conducted across the extended wavelength range has the potential to provide spectral signatures that can be used to map mineral occurrences in the Storkwitz breccia, while the laser-induced fluorescence spectroscopy offers an enhanced sensitivity to REEs, enabling the identification of REE-bearing minerals associated with this carbonatite.

Chapter 2 – Instrumentation & Technique Background

The goal of this chapter is to provide some introduction to the technique of hyperspectral imaging and laser-induced fluorescence spectroscopy. Additionally, it aims to give a brief overview of the characteristic features of minerals observed while discussing previous relevant research related to these techniques in the context of this thesis project. Since the project is focused on REEs, their associated spectral features are clearly stated. As a background, REEs are a group of seventeen chemically similar elements that are found in the Earth's crust. Despite their name, they are not actually rare in terms of their overall abundance, but they are typically found in low concentrations and are often challenging to extract economically. The seventeen rare earth elements include fifteen lanthanides—lanthanum (La), cerium (Ce), praseodymium (Pr), neodymium (Nd), promethium (Pm), samarium (Sm), europium (Eu), gadolinium (Gd), terbium (Tb), dysprosium (Dy), holmium (Ho), erbium (Er), thulium (Tm), ytterbium (Yb), and lutetium (Lu). Additionally, two non-lanthanide elements, scandium (Sc) and yttrium (Y), are also classified as rare earth elements due to their similar chemical properties. These elements are often divided into two groups based on their atomic number and properties: light rare earth elements (LREEs) and heavy rare earth elements (HREEs). LREEs include lanthanum to europium, while HREEs include gadolinium to lutetium, as well as yttrium. This division is primarily based on their atomic weight and differentiating chemical and physical characteristics.

2.1 Hyperspectral Imaging (HSI) Spectroscopy

Spectroscopy is commonly utilized to detect, analyze, and quantify solids, liquids or gaseous materials across different disciplines ranging from chemistry to astronomy. Spectroscopic measurements can identify absorption features related to specific chemical bonds and thus, the abundance and physical state of the absorbing molecular species. With the development of advanced sensors, spectroscopic measurements were combined with imaging methods to create a new field of hyperspectral imaging, also known as imaging spectroscopy or reflectance spectroscopy (Clark et al., 2003; Rencz, 1999)

Hyperspectral imaging is a remote sensing discipline wherein an image spectrometer can map absorption features by acquiring data with the sufficient spectral range, resolution, and sampling at every pixel contained in a raster image (Clark et al., 2003; Goetz et al., 1985). The high spatial resolution combined with the little to no sample preparation makes this non-destructive technique attractive for mineral exploration at sample, near-field, and space-borne scale.

A hyperspectral sensor exploits the photoelectric effect by collecting pairs of free electron holes in the detector element, and hence, the number of collected electrons is a function of the incident photons. The radiometric calibration process for each detector element determines the function of

illumination which is a mathematical function relating the incident light intensity and wavelength to the corresponding signal produced by the detector (number of collected electrons) (Boesche et al., 2015). Hyperspectral sensors particularly like a push broom line scanner include at least one detector array and detectors that are simultaneously illuminated by incident electromagnetic radiation which is spatially and spectrally dispersed. A push broom sensor is a type of imaging device that scans the sample surface by continuously moving along a pre-defined fixed trajectory while collecting data across multiple spectral bands. During this process, energy is emitted or reflected by the material atom or ion that is not equal to the discrete energy of absorption of the incident light. This results in energy emissions at a different wavelength and creating distinct absorption bands or absorption features (Koerting et al., 2021; Clark, 1999; Hunt, 1989). Each detector element, which is essentially an individual sensor, captures and quantifies the photons within a specific wavelength range from a particular solid angle which refers to the three-dimensional angle that the element captures within its field of view. The system is structured in a manner to allow continuous acquisition of spatial and spectral information. The process enables the collection of a hyperspectral data cube where the number of detectors is represented though the x-axis (spatial information) and the number of frames with the y-axis (spectral information). The z-axis denotes the spectrum wavelengths. Thus, each pixel denotes a single spectrum that can be individually evaluated (Boesche et al., 2015).

Hyperspectral data can be acquired across a wide range of the electromagnetic spectrum with the use of different sensors. The four wavelength ranges that are considered in this thesis study include: visible to near infrared (VNIR: 350–1000 nm), shortwave infrared (SWIR: 1000–2500 nm), mid-wave infrared (MWIR: 2700–5300 nm), and long-wave infrared range (LWIR: 8000–12000 nm). These ranges coincide with ranges from commercially available spectrometers and extensive research on the spectral properties of minerals and rocks has already been undertaken in these wavelength regions (Laukamp et al., 2021; GMEX. 2008; Thompson et al., 1999).

2.1.1 Spectral Properties of Minerals

The internal structures and chemical composition determine how metals, minerals and organic materials absorb electromagnetic radiation. This, in turn, determines the position, shape, depth, and width of absorption and emission features observed in the respective spectra (Koerting et al., 2021; Clark et al., 2003). It is important to note that different minerals exhibit distinct diagnostic features in specific wavelength ranges. For example, minerals like micas, clays, chlorites, and amphiboles reveal suitable diagnostic responses in the short-wave infrared region but only moderate responses in the long-wave infrared (Laukamp et al., 2021; GMEX. 2008; Thompson et al., 1999).

In the visible-near infrared (VNIR) region, minerals show characteristic features due to electron transition processes in the form of crystal field arrangement, charge transfer absorptions, or conduction band transition (Savitri et al., 2021; Clark, 1999; Sherman & Waite, 1985; Hunt &

Ashley, 1979; Hunt, 1977). Minerals having spectral features in VNIR include iron-bearing minerals, nickel, copper, manganese, chromium, and REE-bearing minerals (Savitri et al., 2021; Turner et al., 2016, 2014; Hunt & Ashley, 1979; Hunt, 1977). In the SWIR range, spectral responses are a result of vibrational processes mainly of OH and functional groups such as H₂O, Al-OH, Fe-OH, Mg-OH and/or CO₃ (Savitri et al., 2021; Pontual et al., 2008; Clark et al., 1990; Hunt et al., 1973; Hunt 1971, 1970). The MWIR range comprises the fundamental stretching vibrations of O-H bonds like that seen in sheet silicates, amphiboles, and borosilicates, but studies indicate that sulphates, carbonates, phosphates also have distinct features in this range (Laukamp et al., 2021; Yitagesu et al., 2011; Murad & Bishop et al., 2005). Anhydrous silicates such as quartz, feldspars, pyroxenes, olivines and garnets exhibit their diagnostic features in the LWIR range due to the fundamental vibrations of the SiO₄ tetrahedra (Schodlok et al., 2016). The LWIR is dominated by surface scattering processes instead of volume scattering like that seen in SWIR and MWIR (Laukamp et al., 2021) and mineral features in this range are induced by a combination of Restrahlen, Christiansen and transparency features (Laakso et al., 2019; Salisbury et al., 1987).

Previous research focused on the behavior of REE-bearing minerals in the VNIR and SWIR wavelength regions state that REEs display a series of well-defined sharp absorption features in this range (Laakso et al., 2019; Rowan et al., 1986; Hunt et al., 1972; Dieke, 1968). Rowan et al. (1986) and White (1967) stated that the absorption bands of REEs in visible, and near-infrared regions can be explained through electronic field transitions. This is explained by the 4f orbitals of almost all lanthanides being partially occupied (Boesche et al., 2015, Dieke & Crosswhite, 1963). There are 14 different electron configurations with a maximum of two electrons occupying the 7f orbitals. Except for lanthanum and lutetium, whose f orbitals are either completely filled or empty, respectively, incident electromagnetic radiation is absorbed in the appropriate energy, resulting in electron excitations (Boesche et al., 2015; Rowan et al., 1986; White, 1967). The position of the absorption features related to the lanthanides depends on the coordination of cations and the asymmetry of the crystal host structure (Turner et al., 2014a, b). The reflectance spectra are formed by many closely overlapping absorption bands, which primarily arise from 4f-4f intra-configurational electron transitions of Nd³⁺, Pr³⁺, Sm³⁺, and Eu³⁺ ions. The peak positions of certain REEs in the VNIR region is seen in Fig 2.1. As an example, it is observed that the peak positions of the key spectral characteristic absorption bands for neodymium (Nd) are present ~580 nm, ~750 nm, ~800 nm, and ~880 nm (Booyesen et al. 2020, Lorenz et al., 2018, Turner et al., 2014, Hernandez & Filho, 2013; Rowan & Mars, 2003; Rowan et al. 1986, White, 1976). Due to its significantly distinct absorption features among the REEs, Nd can be employed as a key pathfinder element for REEs as a whole (Neave et al., 2016; Booyesen at al., 2020). While absorption bands associated with REEs indicate the presence of rare earth ions, it is important to note that they do not always provide specific information about their associated mineralogy (Clark, 1999).

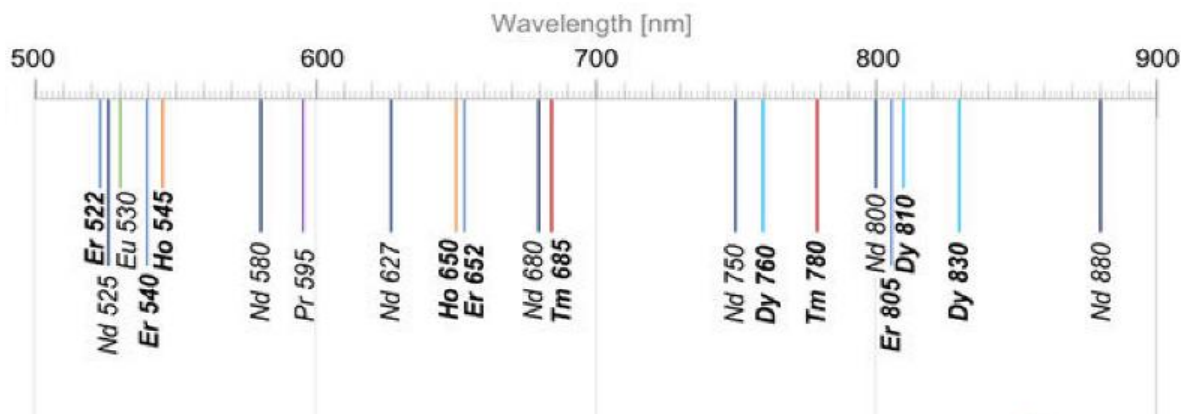


Figure 2.1: Position of most characteristic REE absorption features in the VNIR range according to the chemical analysis and literature review (from Lorenz et al., 2018)

More recent studies (Turner et al., 2014, 2016, 2018) evaluated the features of REEs and REE-bearing minerals in the SWIR region. They observed that less abundant and less pronounced absorptions occur, and these can be generally explained by REE-OH vibrations overtones in the crystal lattice or chemical bond lengths (Laakso et al., 2019; Boesche et al., 2015). Research conducted by Laakso et al. (2019) investigating REE-bearing samples suggested that REEs do not induce any specific resolvable diagnostic features in the LWIR region. An example VNIR-SWIR spectra of common REE-bearing minerals are shown in Fig 2.2.

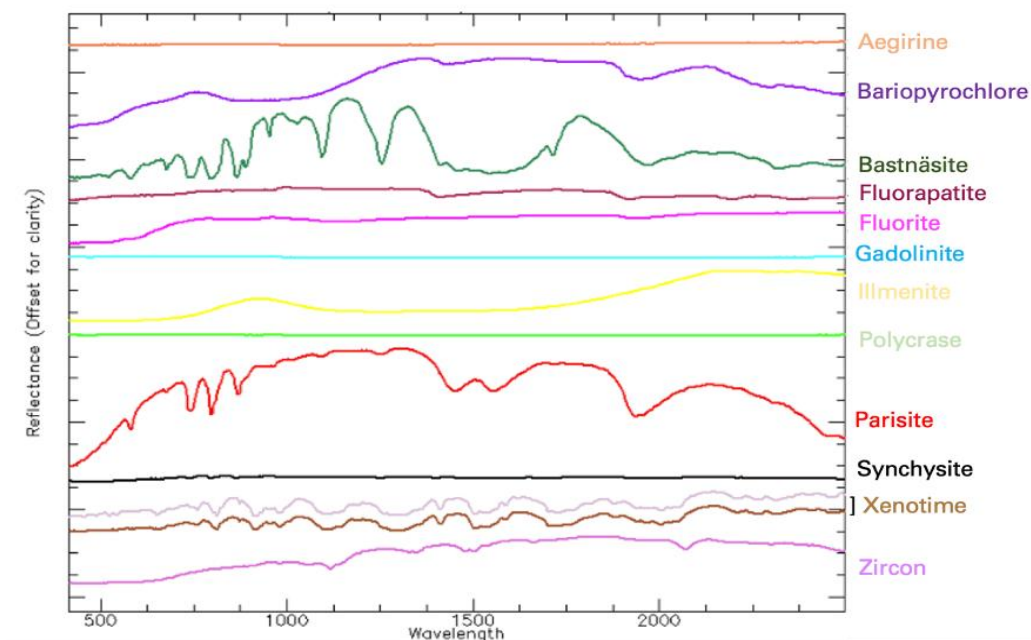


Figure 2.2: Spectral library plot of common REE-bearing minerals (from Koerting et al., 2021).

2.1.2 Previous Research and Toolboxes

The use of hyperspectral imaging in the context of mineral exploration and mapping has steadily increased during the last decade. This is partly attributed to sensor development and better processing routines (Booyesen et al., 2022). Extensive research has been undertaken using ground based HSI like when Snyder et al. (2016) merged such ground-based data with 3D information to map sedimentary structures. The application of this ground-based data in combination with drone-borne techniques allowed for the mapping of geological and lithological units (Kirsch et al., 2018; Boesche et al., 2015). There has also been significant research in the application of HSI in combination with LIDAR and photogrammetric data to successfully 3D model geological structures (Thiele et al., 2021a; Krupnik et al., 2016; Kurz et al., 2013; Buckley et al., 2013)

Extensive research have the highlighted the support for HSI in its application for characterization of lithologies and alteration assemblages associated with mineralization in different ore deposit environments, like magmatic (e.g., Thiele et al., 2021b; De la Rosa et al., 2021; Herrmann et al., 2001; Jones et al., 2005; Zamuido, 2009; Riley et al., 2009; Ngcofe et al., 2013; Swayze et al., 2014; Kruse, 2015; Thiele et al., 2021a), orogenic (e.g., Bierwirth et al., 2002; Mateer, 2010; Laukamp et al., 2011; Arne et al., 2016; Wang et al., 2017) and in sedimentary environments (e.g., Géring et al., 2022, Taylor et al., 2005; Jakob et al., 2016). Booyesen et al. (2022) undertook a multi-scale hyperspectral imaging approach evaluating drill core and outcrop scale data to map lithium-bearing minerals and their spatial distribution in pegmatites across these scales. Similarly, for REEs, several studies particularly demonstrated the application of HSI in close-range scanning of drill cores and outcrops or with drone-borne data of large-scale areas (Booyesen et al., 2019; Zimmermann et al., 2016; Neave et al., 2016; Boesche et al., 2015; Turner, 2015).

As an increasing amount of hyperspectral data has become available due to the growing interests in its application in the raw materials industry, the development of new toolboxes and workflows is required to effectively analyze these data. Previously, MEPHySTO (Jakob et al., 2017) was a toolbox created to perform sensor- and platform-specific geometric distortion and topographical corrections for drone-borne hyperspectral data. While this toolbox for frame-based HSI systems has been adapted for the complex corrections required for drone imaging, it has been used to perform preliminary data corrections for smaller core-scale data studies as well (Booyesen et al., 2022; Loidolt et al., 2022). Similar to MEPHySTO, a new open-source python toolbox called 'hylite' was developed by Thiele et al. (2021). The hylite toolbox can effectively fuse geometric information of the pixels with data from several hyperspectral imaging sensors. It has the capacity to apply geometric and atmospheric corrections for drone and space-borne data and illumination corrections to compensate for variations in lighting conditions during image acquisition. It also has a variety of built-in analysis techniques that can be used to generate a hyper cloud which is a combination of point and hyperspectral data, giving both geometric and spectral information in one. It can pre-process and analyze drill core data as well.

In drill core spectral data processing and analysis, typical approaches have relied on the visual interpretation of the spectra and performing a comparison with the reference spectral libraries like the USGS Spectral library (Kokaly et al., 2017), and CSIRO library (Pejcic et al., 2022). Other analytical techniques used to evaluate and visualise drill core data include dimensionality reduction, minimum wavelength mapping, band ratios, spectral angle mapping, endmember extraction, and unmixing (Van de Meer et al. 2018; Calvin & Pace, 2016; Van Ruitenbeek et al. 2014; Kruse et al. 2012; Littlefield et al. 2012; Van de Meer, 2004). For quantitative estimations of geochemistry and mineralogy along drill cores, a number of supervised approaches have been developed (e.g., Tusa et al., 2020; Acosta et al., 2019,2020; Khodadadzadeh & Gloaguen, 2019).

2.2 Laser Induced Fluorescence (LiF) Spectroscopy

Laser-induced fluorescence (LiF) is a useful well-studied emission spectroscopic measurement technique that has vast applications in biochemical, medical, and chemical research fields (Kwásny & Bombalska, 2022; Wulf et al., 2008; Muraoka & Maeda, 1993). It involves the excitation of a molecular target when aimed at with a beam of laser radiation (Aliabadi & Soboyejo, 2023). The excited chemical species will eventually de-excite and emit light at a wavelength longer than the excitation wavelength. The frequency of excitation-emission is correlated to the specific transition of a molecule or ion from its ground state to a higher excited state and thus the fluorescence is linearly proportional to the input laser irradiance. The emitted fluorescent light is typically recorded with a photomultiplier tube (PMT) or filtered photodiodes.

Studies have supported that LIF has better detection sensitivity to other spectroscopic methods because a signal is observed against a dark background (Aliabadi & Soboyejo, 2023) while being easy to implement. The typical methods for LIF analysis are based on evaluating the measured fluorescence spectrum of minerals (Kauppinen et al., 2014). Colorful emissions of the fluorescent minerals suggest the idea of mineral detection using those colors. Typically, luminescent minerals are composed of a lattice and luminescent centers that are known as activators. The different color radiations of the luminescent minerals that are observed are the result of different activators (Kauppinen et al., 2014, Gaft et al., 2005). Generally, these activators inside minerals are interpreted to be impurities. These impurities are primarily transition metals or rare earth element ions (Kauppinen et al., 2014 Waychunas, 1988).

2.2.1 Behavior of REEs in LIF

Laser-induced fluorescence spectroscopy is a well-suited technique for REE identification due to the increased sensitivity of this method and the unique spectral characteristics of these elements. Given the electronic configuration of the elements (i.e., the trivalent REE with a partially filled 4f-shell) as well as their elemental configuration in relation to other elements within the crystal lattice, REEs exhibit distinct and narrow emission lines that correspond to specific electron excitation and radiative relaxation processes associated with each element.

Fuchs et al. (2021) studied the behavior of various rare earth element species by recording their representative spectra in the UV-visible to near-infrared spectral range (340 - 1080 nm) after utilizing three standard laser wavelengths (325, 442, 532 nm). The study indicated that excitation at all three wavelengths generated characteristic spectra with distinguishable emission lines for EuPO₄, TbPO₄, DyPO₄ and YbPO₄. However, in some samples where high-energy excitation at 325 nm resulted in broad and non-specific defect emissions, it was observed that such non-REE-related emissions could be effectively suppressed by using a lower-energy laser excitation. For PrPO₄, SmPO₄, and ErPO₄, diagnostic emission lines were observed at 442 nm excitation. 532 nm wavelength produced the most efficient excitation for NdPO₄ and HoPO₄. The emission lines characteristic of GdPO₄ were outside the detection range, and none of the three laser wavelengths were suitable for TmPO₄ excitation. A summary of the different emission features observed in the various REE phosphates with the three laser wavelengths, as observed by Fuchs et al. (2021), is seen in Fig 2.3. These diagnostic LIF signatures deliver the spectral fingerprints that can be used to characterize the behavior of REEs in a sample.

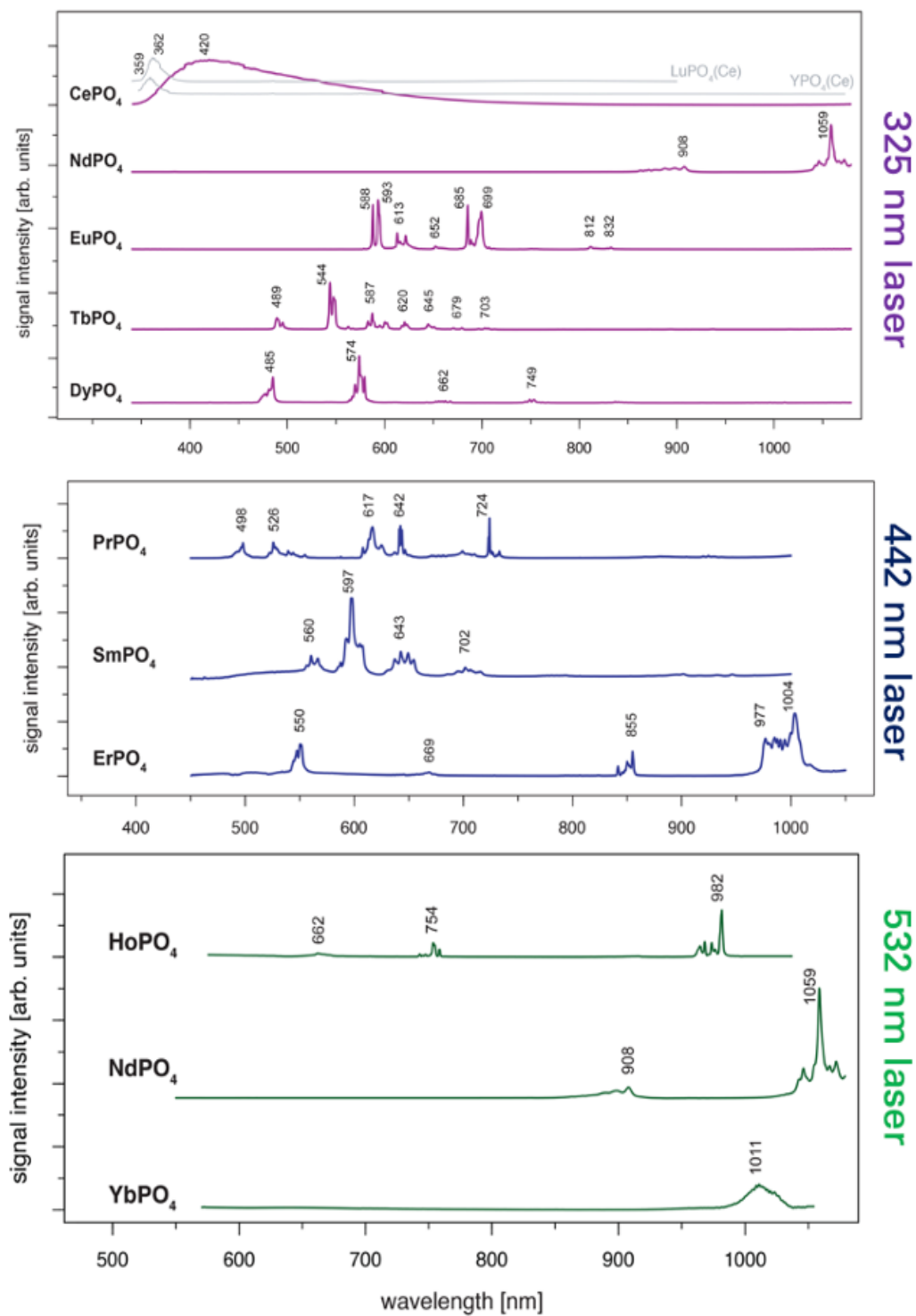


Figure 2.3: LIF reference spectra obtained with 325 nm, 442 nm, and 532 nm laser excitation with the respective diagnostic emission lines for the REE phosphates (modified from Fuchs et al., 2021).

2.2.2 Previous LiF Research and Combined Approach

Past research has been undertaken on the fluorescence spectrum of minerals in laboratory conditions (Gaft et al., 2008; Waychunas, 1988; Reifeld et al., 1996). Other studies investigated the application of LiF for horizon control of mining machines (Nienhaus & Bayer, 2003) or quality control of mineral processing and sorting (e.g., Broicher, 2000, 2005). Also, Bozlee et al. (2005) presented an approach for remote LIF spectral analysis of natural minerals and rocks that yields information complementary to Raman spectroscopy.

Kauppinen et al. (2014) demonstrated the effective application of laser-induced fluorescence (LiF) for rapid mineral mapping of drill core samples extracted from the Kevitsa mine. The study focused on identifying and quantifying nickel, copper, cobalt, platinum, palladium, and gold concentrations within the samples. This research highlights the potential of LiF as a valuable tool for efficient mineral analysis in mining exploration and resource characterization. Though, it is important to note that in such mapping application cases, the broad emission intensities or their ratios were primarily studied instead of distinct features within the LIF spectra. In terms of LiF research specific to REEs, Fuchs et al. (2021) developed the spectral reference library for REEs by capturing diagnostic spectra in the UV-visible to near-infrared range under different laser excitation conditions, as mentioned. This helps to facilitate applications of LIF for REE detection in mineral exploration through the identification and characterization of such elements in potential samples. Additionally, research on REE detection in natural rock samples using laser-induced fluorescence spectroscopy mapping (Reifeld et al., 1996; Gaft et al., 2005; Lorenz et al., 2019; Seidel et al., 2019) has shown to have high promise.

Chapter 3 – Geological Setting

3.1 Regional Geology

The late Cretaceous ultramafic lamprophyre-carbonatite (UML-CR) Delitzsch Complex is located in northwestern Saxony, Germany, approximately 20 km north of Leipzig. It extends over an area of 450 km² and consists of lamprophyre and carbonatite intrusions and the associated Storkwitz and Serbitz breccia pipes. This complex is positioned at the southern boundary of the Mid-German Crystalline Zone (as seen in Figure 3.1) and corresponds to the former suture between Laurussia and Gondwana that was active during the closure of the Rheic Ocean (Kruger et al., 2013). The complex intruded the subsurface at a depth of approximately 100–120 meters below the pre-Cenozoic land surface (Loidolt et al., 2022). Subsequently, the complex became covered by ~100 meters of Cenozoic glacio-fluvial sediments (Loidolt et al. 2022; Niegisch et al., 2020; Krüger et al., 2013). The basement in the region consists of Carboniferous to Lower Permian sediments. To the south, Neoproterozoic to Cambrian sedimentary and volcano-sedimentary units of the Saxo-Thuringian zone underlie the basement layer, while to the north, metamorphic rocks of the Mid-German Crystalline Zone underlie it (Loidolt et al., 2022; Röllig et al., 1990).

The basement layer includes Paleozoic sedimentary rocks that were significantly reworked during the Variscan orogeny (Krüger et al., 2013). This region experienced repeated reactivations of the Variscan structural elements during the periods where the regional stress field was reorganized, like during the development of the Oslo Rift, the opening of the Tethys and Atlantic oceans, and the Alpine Orogeny. These led to the formation of horst and graben structures with substantial uplift (Wagner et al., 1997). The Delitzsch Complex is located at the intersection of an east-west trending structural low and a long-lived, north-south trending zone that is seismically active today. (Kruger et al., 2013; Bankwitz et al., 2003). According to Röllig et al. (1990), the later forming northwest-southeast trending structures played a significant role in controlling the emplacement of melts and determining the location and shape of the breccia pipes, including the Storkwitz Carbonatite.

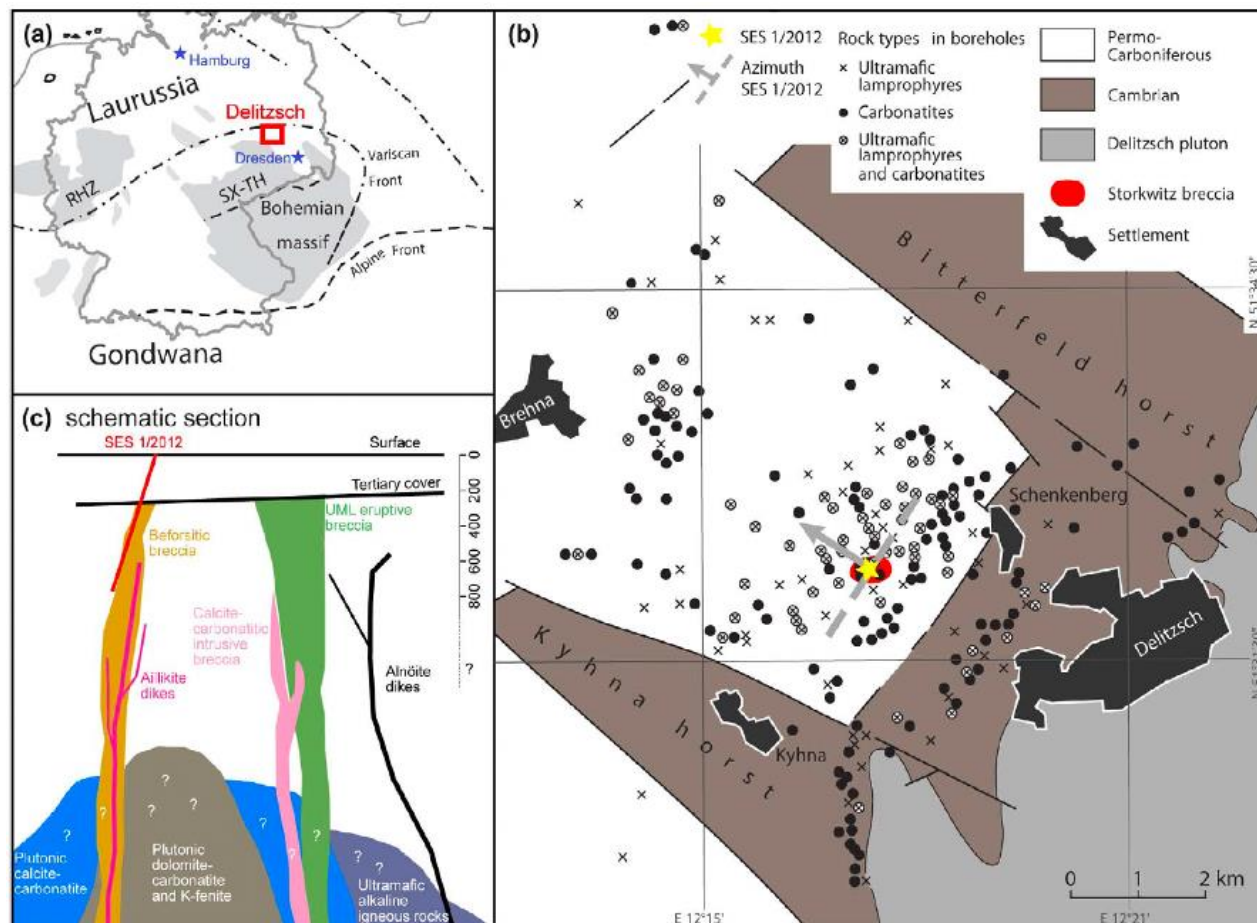


Figure 3.1: (a) Regional overview map of Germany showing the location of the Delitzsch ultramafic complex. (b) Geological map of the Delitzsch area with Cenozoic cover removed (c) Schematic cross-section of the Storkwitz diatreme, RHZ - Rheno-Hercynian zone; SX-TH - Saxo-Thuringian zone; UML - ultramafic lamprophyre (taken from Loidolt et al. 2022; modified from Krüger et al., 2013 and Mockel, 2015)

3.2 Geology and Magmatic Evolution of the Delitzsch complex

Previous research on the Delitzsch complex (Krüger et al., 2012; Rollig et al., 1990) primarily investigated the petrographic characteristics of carbonatites and lamprophyres in order to gain insights into the timing and magmatic evolutionary process of the complex. To outline the evolution of this complex, a multi-stage intrusive sequence was initially proposed by Röllig et al., (1990) which was further developed by Seifert et al., (2000) and Krüger et al., (2013). This sequence suggested the progression of the complex in six stages: (i) intrusion of dolomite carbonatite magmatic body (ii) intrusion of ultramafic and alkaline lamprophyre (iii) beforsitic (different term also used to refer to dolomite carbonatite) diatremes, including xenoliths of dolomite carbonatite and ultramafic lamprophyre forming (iv) ultramafic and alkali lamprophyres intruding diatremes of previous stage, followed by the final development of (v) beforsite and (vi)

alvikite dykes. Kruger et al. (2013) demonstrated that the main phase of the emplacement (ii to iv) occurred during 75-71 Ma and that the carbonatite and lamprophyre magmatism appear to have occurred around the same time. This and the cross-cutting relationships observed by Röllig et al., (1990) suggest a close genetic relationship between the lamprophyres and carbonatites.

Within the Delitzsch complex, the associated ultramafic lamprophyres and carbonatites developed as unique bodies that form dikes, sills, and pipe-shaped small intrusions (Kruger et al., 2012; Rollig et al., 1990). Lamprophyres are defined as a diverse group of igneous hypabyssal rocks, normally occurring as dykes, that contain euhedral to subhedral phenocrysts of biotite and/or amphibole occasionally with clinopyroxene, where feldspars and/or feldspathoids if present are matrix restricted (Le Maitre et al., 2005). The ultramafic lamprophyres found within this complex most commonly occur as centimeter to meter thick, fine-grained, steeply dipping, homogenous dikes. They are observed predominantly as alönite with small occurrences of aillikites and alkali-lamprophyres (Loidolt et al., 2022; Kruger et al., 2013; Seifert et al., 2000; Gruner 1990). In comparison, the carbonatites in this complex form steeply dipping dikes, veins, and pipe-shaped bodies up to tens of meters in diameter and mainly occur as intrusive breccias with abundant xenoliths (Röllig et al., 1990). The two subgroups observed here are the dominating dolomite-ankerite-carbonatites and the minor calcite-carbonatites. The breccia pipes at Storkwitz and Serbitz exhibit a wide range of lithologically diverse clasts, including angular to subangular rhyolites and metasedimentary rocks from the surrounding wall rocks. Additionally, they contain rounded to sub-rounded fragments of carbonatite and ultramafic lamprophyre, which indicates that these occur at depths greater than that reached by the drilling campaign (Loidolt et al. 2022, Kruger et al. 2013, Röllig et al., 1990).

3.3 Exploration History

Historically, the Delitzsch complex was examined during two exploration drilling campaigns consisting of over 500 holes that reached depths of 1100 meters (Seifert et al., 2000). The initial efforts, carried out in collaboration between SDAG Wismut and the Central Geological Institute (ZGI) in Berlin, focused on uranium prospecting and exploration around the known Permian intrusions in the Delitzsch–Halle area during the late 1960s to 1989. This led to the accidental discovery and confirmation of rare earth resources hosted within the Storkwitz breccia (Mockel 2015). Kormeier & Miroschnitschenko (1979) stated that the drilling activities captured carbonatite and carbonatite breccia hosted REE mineralization in 143 drill holes. These holes are distributed over an area of 20 km². The rock intervals in these holes contained elevated concentrations of niobium (Nb), tantalum (Ta), phosphorus (P), and thorium (Th).

The renewed interest in the rare earth element resources prompted further drilling between 2011 and 2015 by Seltenerden Storkwitz AG currently called Ceritech. The objective of this drilling campaign was to delineate the extent of the resource and resulted in the resource estimation of 4.4

million metric tons (Mt) according to the JORC standards. The average grade of the rare earth oxides was appraised to be 0.45 wt.% (Deutsche Rohstoff AG 2013). While potential resources do presently exist, the deposit was considered not to be economically viable due to several factors outlined by Kormeier & Miroschnitschenko (1979) and Deutsche Rohstoff AG (2013). These include (1) the absence of a known uniform carbonatite massif, (2) large spatial distances between the ore bodies and (3) the presence of a thick Cenozoic cover over the complex that contains crucial groundwater aquifers.

3.4 Previous Research on SES 1/2012 Drill core

The interval investigated in this project is part of the SES 1/2012 drill core and was recovered by Ceritech, in 2012. The aim of this drilling was to intercept the entire Storkwitz breccia. The coordinates of the drill hole collar are 51.534998 N, 12.283838 E, with an azimuth of 327° and a dip of 12.1°. The hole reached a total length of 700 meters (Figure 3.1).

The drill hole logging was carried out by Ceritech in 2012 and has been extensively discussed in Loidolt et al. (2022). This borehole consists of 138 m of Cenozoic glacial fluvial overburden, which is then traversed by ~138 to 246 m of porphyry granitoid wall rock. The porphyry granite is intruded by a lamprophyre dike at 182 to 188 m and by calcite-carbonatite dike at 242 to 244 m. The Storkwitz breccia (252 to 640 m) underlies altered lamprophyres (246-252 m). Additionally, fine-grained calcite-carbonate dikes intrude the breccia at ~381-385 m and ~615 m, and a lamprophyre dike at 626-628 m. The breccia itself is categorized into two distinctive zones: an upper zone (252–269 m) and a lower zone (372– 640 m). A series of faulted brecciated porphyry granite and an extensive fracture zone at 361–372 m delineate the two zones. The drill core also intersects several fault zones including the intensely chloritized fault zone at 435.8–437 m and additional faults that cut the breccia at ~417 and ~556 m. Beyond 640 m, metasedimentary rocks are observed in the drill core, which include veins of intrusive carbonate material and silty mudstone

This thesis evaluates the 419 - 491 m core interval. This interval examined comprises well-cemented breccia containing country rock and granitoid clasts. The clasts are present abundantly as coarse-grained granitoids or in specific intervals as porphyritic granitoids and sedimentary rock clasts. The core log from Ceritech (2012) for this interval is seen in figure 3.2.

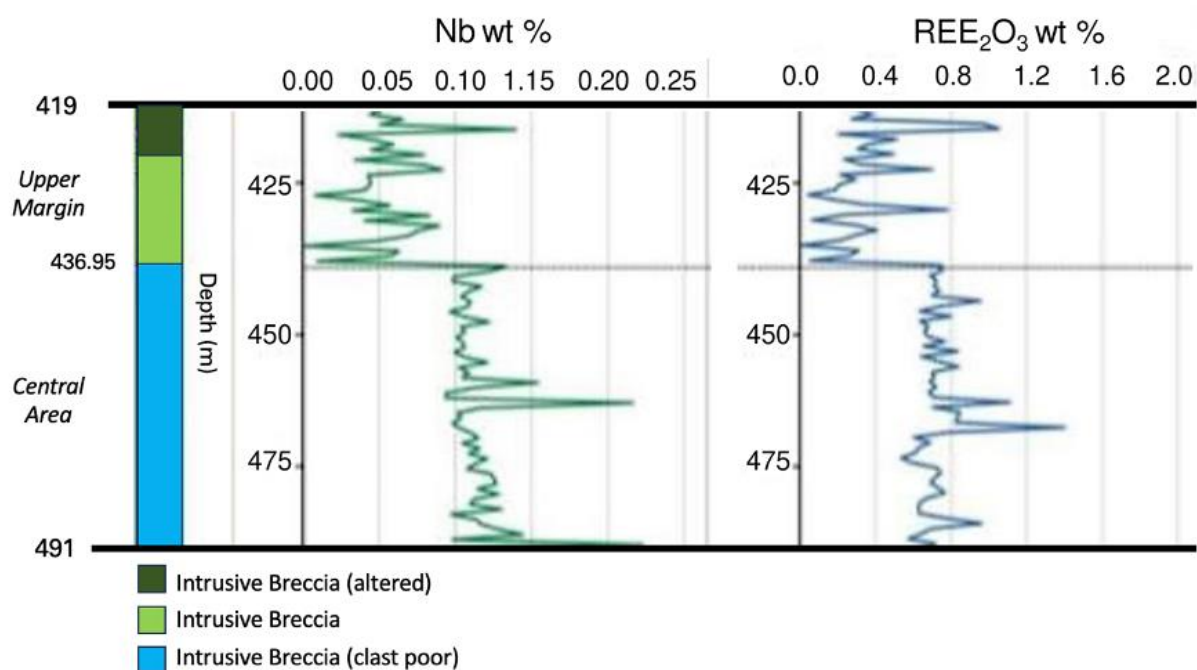


Figure 3.2: Downhole lithological logs for 419–491 m interval with Nb% and REE% based on m-scale geochemical assaying (modified from Ceritech, 2012).

Recently, detailed multi-method geochemical and mineralogical investigations using the SES 1/2012 drill core have been conducted to better evaluate the Storkwitz carbonatite. These include a study by Niegisch et al. (2020) that examined the upper zone of carbonatite breccia (240 - 273 m) in this drill core, REE mineralization that was predominantly LREE enriched was observed to be hosted in the fine-grained alvikite veins and the heterogeneous carbonatitic igneous breccia body. The principal REE-bearing mineral phases are monazite as well as bastnaesite-synchisite group minerals and are suggested to be formed mainly by secondary processes (Niegisch et al., 2020). Strong evidence for supergene alteration includes the mineral paragenesis, textural features, the formation of supergene iron oxyhydroxides and, recrystallization of the breccia matrix. However, Niegisch et al. concluded that this did not lead to significant enrichment of the REEs but only a redistribution of REE to new mineral phases in the portion of the Storkwitz carbonatite near the surface (Niegisch et al., 2020).

Loidolt et al. (2022) examined an upper part of the lower zone of the breccia (425 - 542 m) where the effect of supergene processes as observed by Niegisch et al. (2020) was stated to be lower. High REE concentrations in this interval were indicated in past studies using hyperspectral imaging spectroscopy (Loidolt, 2018; Müller et al., 2021). Loidolt et al. (2022) found that the breccia hosts an assortment of clasts that are cemented chiefly by an ankeritic matrix. The clasts are representative of different lithologies like country rock, mixed medium-grained ankerite-dolomite-calcite-carbonatites, fine-grained dolomite-carbonatites, and fine grained ankerite-

carbonatites with associated REE mineralization (Loidolt et al. 2022). Through geochemical analyses like X-ray diffraction (XRD) and mineral liberation analyses, Loidolt et al. (2022) suggested a multistage intrusive and mineralization sequence which consists of the intrusion of an early carbonatite magma at depth which was followed by the fine-grained ankerite-carbonatites intruding at shallow depth and then the REE mineralization in the fine-grained ankerite carbonatites resulting from the late-stage REE enrichment of a residual 'brine-melt'. Subsequently, the explosive brecciation of the complex resulted in minor REE mineralization by a hot, evolving hydrothermal fluid and finally ended with a supergene alteration of Fe-(Mg-Mn)-rich carbonate minerals in the breccia matrix (Loidolt et al., 2022). The fenitization and biotitization at Storkwitz is also suggested to have occurred in multiple stages. Ultimately, the REE mineralization in Storkwitz carbonatite was not caused by externally introduced sources but rather by the accumulation of REE and other incompatible elements due to the primary magmatic fractionation prior to depressurization (Loidolt et al., 2022).

Chapter 4 – Methods

A summary of the steps employed are described below, along with the measurement parameters for the different data acquisition techniques. In the end, a two-stage workflow for the acquisition and processing of hyperspectral and LiF data of the Storkwitz drill core is proposed (Fig 4.4, Fig. 4.5). This workflow is developed to address the research question about the capability of these techniques for mapping and characterization of the Storkwitz lithologies and the associated REE mineralization.

To provide some background on the available data: As part of the previous study by Loidolt et al. (2022), a total of 26 block samples were extracted from the drill core interval of 425–542 m. These samples are considered to be representative of the mineralogy in that interval. In preparing these samples for mineral liberation analysis (MLA), the samples were cut into two portions: ~200 μm thick sections on which the MLA analysis was conducted and 40 x 25 x 10 mm offcut counterpart blocks. While the thick sections themselves were not available for this study, I had access to the mineralogical data acquired from them. Of the 26 samples from the 425–542 m interval in Loidolt et al. (2022), 10 block sections in the 419–491 m interval evaluated here were accessible for this project (Figure 4.1).

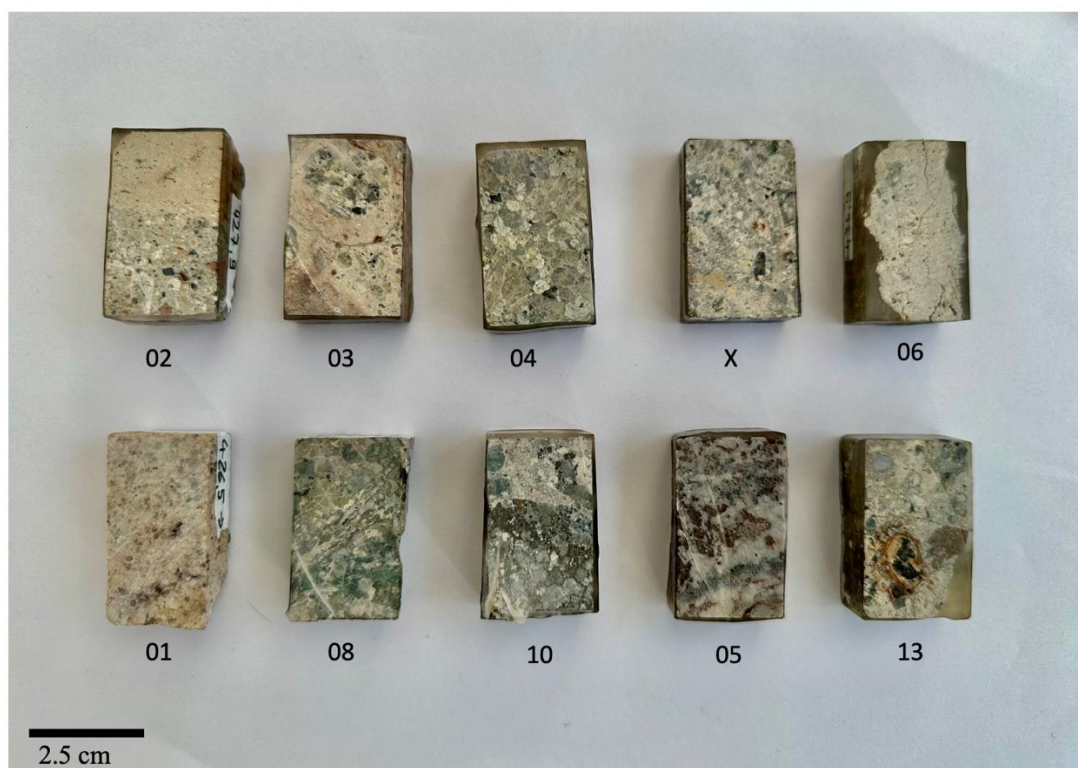


Figure 4.1: Sample blocks from the Storkwitz drill cores with available SEM-MLA mineralogical data used for qualitative hyperspectral interpretation.

4.1 SEM-MLA Data Acquisition

Mineralogical data of the ten thick section used in this study were acquired as part of the mineral liberation analysis (MLA) done on Scanning electron microscopy (SEM) and energy dispersive X-ray spectroscopy (EDS) data by Loidolt et al (2022). For these samples, the mineral liberation analysis (MLA, automated EDS mineral identification system) was performed using a FEI Quanta 650 MLA-FEG. Details about the equipment parameters used for the acquisition of the data can be found in Loidolt et al. (2022). Lithological and depth information about the ten thick sections of the corresponding blocks chunks which are used in this thesis is provided in Table 4.1.

Table 4.1: Block samples extracted from the drill core with their depth and associated lithology (from Loidolt et al. 2022).

Sample Name	Depth (m)	Lithology
BLK_01	425.5	Granitoid
BLK_02	427.9	Intrusive breccia with granitoid clast
BLK_03	428.7	Intrusive breccia with fenitized granitoid clast
BLK_04	429.2	Granitoid with fenite vein
BLK_X	429.3	Intrusive breccia, REE-fluorcarbonate blebs in ankerite-carbonatite clast
BLK_05	429.4	Ankerite-carbonatite with REE-fluorcarbonates, biotite
BLK_06	436.9	Intrusive breccia, faulted
BLK_08	445.4	Granitoid, fenitization overprints REE-fluorcarbonate-ankerite-carbonatite vein
BLK_10	453.8	Granitoid, fenitized
BLK_13	489.5	Intrusive breccia, large pyrite, and biotite fragments

4.2 Hyperspectral Data Acquisition

The hyperspectral reflectance data for the 419–491 m drill core interval as well as the ten offcut blocks of the Storkwitz drill core were acquired utilizing the SisuROCK drill core scanner with a mounted sensor setup (Fig. 4.2). It is important to note that interval 485–486 m was missing in the interval and therefore not included in the scans. As an advantage of hyperspectral scanning, no intensive sample preparation was required. The samples were only brushed clean and arranged to ensure that all samples are in the same focus plane. Some small sections of the drill core were covered with epoxy from previous sampling efforts. These were avoided where possible by turning them over.



Figure 4.2: SisuROCK drill core scanner (left) with mounted sensors (right) in the visible to near-infrared and shortwave infrared (VNIR-SWIR), mid-wave infrared (MWIR), and long-wave infrared (LWIR) range.

The drill core scanner used for data acquisition is equipped with three hyperspectral push-broom sensors, a SPECIM AisaFENIX, an FX50 and an AisaOWL (Spectral Imaging Ltd., Oulu, Finland; Table 4.2) as well as a high-resolution RGB camera with a spatial resolution of 250 μm . The scanner is equipped with internal lighting and the samples are placed on a moving tray that travels under the scan line of each sensor and a conventional white panel like a Spectralon R90 was used as reference when measuring the samples.

Table 4.2: SisuROCK drill core scanner acquisition parameters for the visible to near-infrared and shortwave infrared, mid-wave infrared, and long-wave infrared range.

	VNIR	SWIR	MWIR	LWIR
Wavelength Range	380 - 970 nm	970 - 2500 nm	2700 - 5300 nm	7700 - 12300 nm
Specim Sensor	AisaFenix	AisaFenix	AisaFX50	AisaOwl
Spatial Resolution	1.50 mm/px	1.50 mm/px	1.06 mm/px	1.60 mm/px
Calibration	Grey Panel		Thermic Calibration	

4.2.1 HSI Data Pre-Processing

The acquired hyperspectral data was processed using hylite (Thiele et al., 2021) built into an in-house real-time preprocessing system (as seen in Fig. 4.4). This system is a framework encompassing numerous modular functions that can be tailored to accommodate specific experimental requirements. After sensor-specific calibrations are done based on an available calibration file, dark current corrections are performed to remove hot pixels and other fixed-pattern noise. Other preprocessing steps include bad pixel replacement, lens distortion and geometric correction, and radiance to reflectance value conversion. This produces individual image files from each hyperspectral sensor that are geometrically and radiometrically corrected. The images are then coregistered, meaning they are aligned spatially to match the calibration image or reference coordinate system. This step ensures that all images have consistent positioning and orientation.

The calibrated, corrected, and co-registered data must be masked so that only relevant sample pixels are available for analyses. For this step, an automatic image segmentation tool was used. This masking system integrates the Napari image viewing python tool with Segment Anything Model algorithm from Meta AI (Kirillov et al., 2023) to automatically identify and delineate regions of interest within the images. The resulting masks were inspected for quality and manually corrected before being applied to the data. Next, the first 20 bands of the Fenix sensor data (VNIR-SWIR) were removed, because that part of the data is very noisy. Only the data that was HSI block data which was used for endmember extraction was smoothed using a Savitzky-Golay filter. This function works by fitting a least-squares polynomial regression to a small window of neighboring data points and then estimating the smoothed value for the central point of that window. The window length i.e number of coefficients of 7 and a 2nd order polynomial was used to fit the data. Through this process, it effectively removes high-frequency noise components while preserving the underlying trend or shape of the data resulting in better noise reduction without significantly distorting the signal.

As an additional processing step, principal component analysis (PCA) was performed. The purpose of implementing this technique was to visualize and understand the spectral variability present in the dataset before subsequent analyses like endmember extraction and spectral unmixing and mapping are undertaken. It transforms the original variables into a new set of uncorrelated variables called principal components. These components are ordered in terms of their contribution to the overall variance of the dataset meaning the first component illustrates the most variance in the data. Using the hylite toolbox (Thiele et al., 2021), PCA was performed on the block section data for each wavelength region dataset. The hyperspectral data was visualized using the first three components.

4.3 Band Ratios

Band ratios are a common technique for spectral feature mapping. This method involves dividing one or more spectral bands to obtain relative intensity maps that reflect variations within a specific spectral range. Essentially band ratios are calculated using the reflectance value at the shoulder of an absorption feature and dividing it by the value of the minimum. An increase in this ratio is proportional to the absorption depth of the feature. By employing this technique, specific spectral characteristics related to mineral compositions can be enhanced (Mars & Rowan, 2011). The band ratio method is particularly effective when applied to high spectral resolution data, where the precise location of narrow absorption features provides sensitivity to distinct mineral compositions. The performance of different band ratios was initially evaluated on the block section data for which the mineralogical information is available. Following this step, the most effective band ratios were applied to the spectral data of the drill cores. The band ratios we applied to characterize the Storkwitz cores are listed in Table 4.3. In the end, the three band ratio results were compiled into a single map referred to as Fe-oxide band ratio map of the drill core.

Table 4.3: Spectral indices for relevant features for band ratios.

Feature	Ratio (nm)	Reference
Fe ⁺³ Index	600 / 570	GMEX (2008)
Fe ⁺² Index	(920+1650) / (1230+1035)	Cudahy et al. (2008)
FeOH	2280 / 2245	Cudahy et al. (2008)

4.4 Minimum Wavelength Mapping for Hyperspectral Data

Minimum wavelength (MWL) mapping is an unsupervised technique to visualize the position and depth of characteristic absorption features within specific spectral ranges at the same time (Hecker et al., 2019). This process of feature fitting is repeatable but computing power intensive. It gives a per-pixel overview map of the dominantly abundant mineral present. It is performed by selecting specific wavelength ranges and fitting mathematical functions, such as asymmetric Gaussian functions (Thiele et al., 2021), to hull corrected spectra. In resulting maps, the hue represents the feature position, while the brightness value represents the absorption depth and therefore, the feature position and depth estimates create maps within the HSI color space (Hecker et al., 2019). This method is effective when implemented on high spectral resolution data and when the position of absorption features is sensitive to specific mineral compositions. Similar to the approach for band ratios, the suitability of different spectral ranges for distinguishing minerals, taking into

account potential overlapping features, was initially tested using the combination of block section reflectance and the corresponding MLA mineral data. Minimum wavelength maps were generated for the hyperspectral data using the hylite toolbox (Thiele et al., 2021). The MWL technique was also utilized to map the emission features in the LiF spectroscopy data and is discussed within that context further below.

The main spectral ranges that were mapped using the MWL technique, and the interpretation of these maps, are listed in Table 4.4. However, it is important to note that Nd is used as a pathfinder for the overall presence of REEs due to its very prominent features observed in the VNIR region (Turner et al., 2014), similar to the approach by Neave et al. (2016). Therefore, the Nd minimum wavelength map plays a critical role in the selection of assumed REE-rich zones for further LiF spectroscopy measurements.

Table 4.4: Spectral ranges used to extract the position and depth of specific absorption features using minimum wavelength mapping.

Spectral Range	Expected Feature Name	Associated Mineralogy	Reference
790 - 810 nm (1 minimum)	~800 nm	Deep spectral feature associated with neodymium	Turner et al. (2014)
2190 - 2220 nm (1 minimum)	~2200 nm	AIOH absorption associated with clay or mica minerals.	Kokaly et al. (2017), Laukamp et al. (2021)
8180 - 8900 nm (4 maxima)	~8200 nm	Quartz primary reststrahlen band peak feature	Kokaly et al. (2017), Laukamp et al. (2021)
	~8400 nm	Plagioclase (Albite) peak feature	Kokaly et al. (2017), Green and Schodlok (2016)
	~8600 nm	First Aegirine peak feature	Herrmann (2015)
	~8800 nm	Mica peak feature	Laukamp et al. (2021)
11200 - 11600 nm (1 maximum)	~11250 nm	Carbonate peak feature	Laukamp et al. (2021), Green and Schodlok (2016)

4.5 Endmember Extraction & Library Creation

For the spectral unmixing and spectral angle mapping that were employed to map the distribution of the different geological lithologies (see below), a spectral library of endmembers was required. Hyperspectral endmembers are “basis spectra” assumed to be pure, or unmixed, pixels in the image. These were extracted using an endmember extraction algorithm called NFINDR (Winter, 1999). It exploits the geometric properties of convex sets to identify endmembers. To prepare the dataset and help determine the data sample volume in an easier manner, orthogonal subspace

projection (OSP) and maximum noise fraction (MNF) transformations were applied to the dataset to minimize the data dimensionality inherently as part of the algorithm. The algorithm then searches for a simplex, a geometric shape with maximum volume, using these endmembers. The algorithm assumes that in an L-spectral dimensional space, the volume enclosed by a simplex formed by the purest data sample is greater than any other combination of data samples (V. Kale et al., 2020). A larger volume implies that the simplex spans a broader range of the spectral space, indicating a better representation of the underlying endmembers. For each data sample and endmember, the endmember is replaced with the spectra of the data sample, and the volume is recalculated. If the volume increases, the new data sample replaces the endmember. This process continues until no further replacements occur. While typically the algorithm starts with a randomly selected set of pixels and progressively expands the simplex within the dataset, this has shown to have drawbacks where the algorithm converges at a local optimum and thus, affects the final outcome (V. Kale et al., 2020).

It is important to note that different diagnostic features exist for minerals across different wavelength regions. Therefore, the three wavelength regions (VNIR-SWIR, MWIR, and LWIR) are regarded as separate datasets that are collected using different sensors in the context of endmember identification rather than combining them because an endmember pixel identified from the VNIR-SWIR data will not necessarily represent an endmember in the MWIR or LWIR range.

To solve the limitation caused by the randomized initialization, an automatic target generation process (ATGP) algorithm is applied when performing the N-FINDR algorithm. This unsupervised target detection technique searches for potential pure members with the maximal orthogonal projections using an orthogonal subspace projector (Zhang et al., 2009). This implies that these potential targets have the strongest presence or distinctiveness in the data. Thus, using the ATGP algorithm, the initial spectra and abundances of target endmembers are first generated which then improves the performance of the endmember extraction algorithm overall.

The N-FINDR algorithm extracts a predefined number of endmembers set by the user. The optimum number of endmembers in each dataset was determined iteratively using a combination of domain knowledge and data analytical techniques. Therefore, the results obtained from the principal component analysis are visualized to understand the heterogeneity in the block data and recognize potential domains that share similar characteristics. Additionally, the elbow method (Syakur et al., 2018) and silhouette score technique (Shahapure & Nicholas, 2020), used in unsupervised K-means clustering algorithm to find the optimal number of clusters, were also used in this context to estimate the ideal number of endmembers. In the elbow method, the distortion score is the sum of square distances from each point to its assigned center. With an increase in the number of clusters (k), the average distance decreases and thus, to find the optimal number of clusters in a plot, the value of k is found which corresponds to a sharp and steep fall in the distortion

score i.e., where an elbow occurs. For the silhouette score plot, the optimal number of clusters is calculated using the silhouette coefficients of each point. This coefficient is determined by dividing separation measure by cohesion measure and subtracting that value by 1 if separation measure is bigger than cohesion measure or by 1 subtracted by the value of cohesion measure divided by separation measure if the cohesion is bigger the separation (Saputra et al., 2019). The highest silhouette coefficient value corresponds to the best overall cluster number.

After the number of endmembers to be extracted is determined, the spectra of these endmembers were then evaluated with the available mineralogical information. This mineralogical data also allowed for the manual addition of certain endmembers that were not well represented in the automatically extracted endmembers but are important minerals in the deposit. In the end, following the interpretation of the spectra of the extracted endmembers, a spectral library for each wavelength range was created.

4.6 Spectral Unmixing

The unmixing algorithm used on this data is the fully constrained least-squares method (FCLS) (Heinz & Chein-I-Chang, 2001). This method is a combination of two approaches, nonnegativity constrained least-squares algorithm (NNLS) and sum-to-one constrained least-squares algorithm (SCLS). Generally, spectral unmixing is based on the assumption that the reflectance spectra of any given pixel is comprised of a combination of different endmember signals. In this case, the spectral library created from the block sections data represents these endmembers and a vector a is of the mixing coefficients (ratios) of these endmember signals. Therefore, this function aims to perform this operation by minimizing the reconstruction error associated with the inversion and estimation of this mixing coefficient. However, two key requirements must be fulfilled to perform this method: (1) The coefficients need to be non-negative and (2) all coefficients of one pixel need to sum up to one (Michelsburg & Léon, 2018). The individual NNLS and the SCLS algorithm respectively ensure that these constraints are met. An only NNLS algorithm was not used because when testing the result of the algorithm in contrast to the results of the FCLS, the NNLS algorithm led to errors in the accurate classification of the classes. This was visibly evidenced by the inaccurate classification of biotite and muscovite zones within the VNIR-SWIR data. Therefore, FCLS was chosen to be implemented instead.

Using the spectral libraries created for each dataset, spectral unmixing is performed (as seen in Fig 4.4). This generates abundance maps for each endmember in the respective wavelength range. These individual abundance maps for each tray set were then compiled and to allow for interpretations about the endmember distribution across the entire drill core length. Additionally, a maximum classification map for each of the three datasets was created. Each pixel in this map is classified to represent the most abundant class across that pixel in all the individual endmember abundance maps.

4.7 Spectral Angle Mapping (SAM) Algorithm

The SAM algorithm is a supervised image classification method that enables efficient comparison between image spectra and reference spectra, allowing for rapid mapping of their similarity (Kruse et al., 1993). The reference spectra can be derived from laboratory or field spectra or extracted from the image itself. SAM operates by measuring the angle between the reference spectrum and each pixel vector in a multi-dimensional space. Smaller angles indicate a closer match between the pixel spectrum and the reference spectrum. The hylite toolbox is used to implement the spectral angle mapping algorithm on the hyperspectral data of the drill cores, using the endmember library. A spectral angle threshold of 10° is applied to prevent overestimation of the low intensity-matrix endmember or any pixels spectra that are very dissimilar to any of the endmembers. Thus, an additional unclassified class is also generated that includes the pixels which represent the pixels that are greater than the specified spectral angle threshold and therefore could not be classified into any of the respective endmember groups. Ultimately, this algorithm creates one map each in the VNIR-SWIR, MWIR and LWIR region that represents the distribution of the respective reference endmembers across the entire length of drill core scanned.

4.8 Selection of Samples for LiF Measurements

The LiF stage of the workflow begins with identification of REE-rich zones in the blocks and drill cores which is primarily done by examining the Nd MWL map and using Nd as a REE pathfinder (seen in Fig 4.5). From the REE MWL map of the block sections that was created, Block 05, Block X and Block 10 are identified as Nd rich samples and were selected for further scanning using the LiF setup. For the drill core, selection of REE rich core pieces was more complex. While the REE MWL map did reveal several zones with high concentrations of Nd, as mentioned before, large portions of these REE-rich zones in the core pieces were covered in epoxy. The LiF sensor is sensitive to the epoxy mixture and would produce poor results for REEs if scanned. Therefore, two less intensely concentrated pieces of drill core were selected. These core pieces are located between 486.3 to 486.5 m interval.

4.9 LiF Data Acquisition

The selected blocks and core pieces were scanned using an experimental integrated line-scan sensor system (Abend et al. 2019) using a sCMOS 50-v10E camera from Specim (Fig. 4.5) (Spectral Imaging Ltd., Oulu, Finland). The ions are excited at the corresponding sample surface line using two continuous wave laser diodes of 447 nm (blue) and 525 nm (green). By collimating and focusing the laser diode emission cones with specifically designed modular cylindrical lenses built for beam shaping, the line excitation required is achieved (Abend et al., 2019). In order to

have good resolution at considerable detection speed, the camera utilized has a spectral range of range between 400–1000 nm with a spectral and spatial resolution of 2.9 nm and 2184 pixels respectively. The camera also has a frame rate of up to 100 images per second.

In the current setup used for the data acquisition on the Storkwitz samples, the two lasers, which can be operated independently, are used simultaneously to provide greater excitation energy and an integration time of 300 ms is used. The samples are placed on a belt that moves at 0.003 m/s travelling under the laser and camera structure. It is also important to note that a 550 nm long-pass filter is fitted in front of the lens of the sCMOS camera to block out light from the laser LEDs. No particular sample preparation is required. Additionally, a small REE-rich sample from Sillinjärvi, Finland is scanned alongside all the samples and used as a reference sample with known peak features to calibrate the instrument

LiF Experimental Line Scan Setup

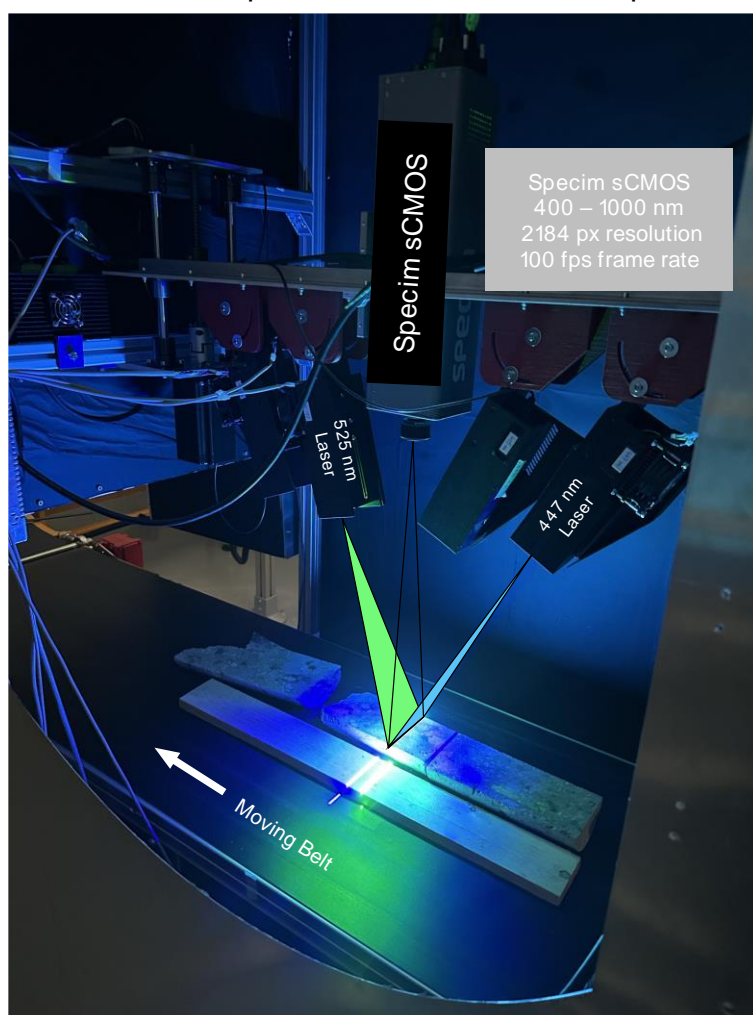


Figure 4.3: Schematic diagram illustrating the LiF line scanning experimental setup used for data acquisition.

4.9.1 LiF Data Pre-Processing

The obtained fluorescence data was corrected in three steps. Firstly, the dark current was subtracted using reference calibration data. Secondly, the data was converted into radiance values. Lastly, the dataset was spectrally cropped at 540 nm outside of the laser bands so that only real emission peaks can be evaluated, and the feature of lasers can be omitted. Following these preprocessing steps, the LiF data for the block sections and core pieces was manually masked. After checking the quality of the corrected and masked data, it was stored as a 3D data cube.

4.10 Minimum Wavelength Mapping for LiF Spectroscopy Data

Initially, various points which showed a visual differences in intensity or luminosity were chosen and a spectral library was created that included most variance in the spectra observed. Following this, the main emission peaks were identified. Similar to hyperspectral data processing and using the hylite toolbox, the minimum wavelength mapping method was used on the LIF data from the block section and core pieces, fitting asymmetrical gaussian functions to the peaks within the specified spectral ranges. The two main spectral ranges that were mapped using the MWL technique, and their correlating interpretation, are listed in Table 4.5.

To understand the correlation amongst the several identified peaks, false color images of the samples were created where the R-G-B bands were assigned to specific peak wavelengths. This created a visual representation of the distribution of peaks within the samples. In the end the results of the minimum wavelength mapping along with the false color images of the block sections are correlated to the SEM-MLA mineralogical data to allow for geological interpretations about the distributions of the potential REEs. These interpretations are then extrapolated onto the drill core pieces which provides information about their distribution in relation to the entire drill core.

Table 4.5: Spectral ranges of the specific emission peaks using minimum wavelength mapping techniques.

Spectral Range	Expected Feature Name	Associated Mineralogy	Reference
585 - 610 nm	~600 nm	Emission feature associated with Sm ³⁺ , Pr ³⁺	Gaft et al. (2005), Fuchs et al. (2021)
860 - 900 nm	~870 nm	Emission feature associated with Nd ³⁺	Gaft et al. (2005), Fuchs et al. (2021)

4.11 Validation

To provide validation for the qualitative data produced through this workflow (as seen in Fig 4.4), visual inspection of the drill cores was conducted. This visual inspection consisted of using common field-based identification approaches like hand lens inspection, scratch test and acid test. Several points were deliberately chosen in the different resulting maps to match the distribution of the mapped mineral to the actual drill core present. Given the fine-grained nature of the samples, a portable XRF was not chosen as a validation tool. The spot diameter of the equipment would be too large to accurately classify the different fine-grained clasts within the matrix. Moreover, the detection limit of the machine would not be sufficient to recognize and distinguish the distribution and concentration of the REEs.

4.12 Proposed Workflow Overview

As mentioned before, a proposed workflow is developed that provides the organized sequence of method and steps needed to spectrally characterize the lithology using HSI and to identify REEs using LiF set up. The first phase of the proposed workflow involves the acquisition and analysis of the hyperspectral data which will eventually allow for the selection of key samples for further evaluation with LiF spectroscopy.

The workflow begins by acquiring and correcting hyperspectral data of the drill core and the block sections. Hyperspectral data collected in the VNIR-SWIR, MWIR and LWIR are considered as three different datasets since data is collected using different sensors. A combination of automatic endmember extraction and manual selection is then conducted on each dataset to create a corresponding spectral library. Only the block hyperspectral data is used since the blocks are assumed to be representative of all the existing mineralogies and would be less processing power intensive to use than the entire drill core interval. The mineralogical data from the corresponding thick sections was used as a basis for the spectral analyses of these endmembers. After the three equivalent spectral libraries are generated, they are used for spectral unmixing that is performed on the entire hyperspectral drill core dataset. This yields abundance maps for each of the endmembers in each of the three wavelength ranges. These libraries are also used to perform spectral angle mapping (SAM) on the drill cores to create mineral maps. Additionally, other techniques like band ratios and minimum wavelength mapping are implemented on the drill core data to qualitatively map relevant mineral groups and REE rich zones. While there have been workflows developed that utilize machine learning methods to create quantified mineral abundance estimations (Khodadadzadeh & Gloaguen, 2019; Acosta et al., 2019, 2021; Tusa et al., 2019, 2020), these methods require the MLA and HSI datasets to be co-registered. Due to the

thickness of the saw blade used during sample preparation, material between the thick section and the corresponding offcut block was removed, which prohibits easy co-registration. Hence, the mineralogical mapping of the drill cores is qualitative rather than quantitative, guided by the MLA mineral maps, and validated based on a visual inspection of the drill core.

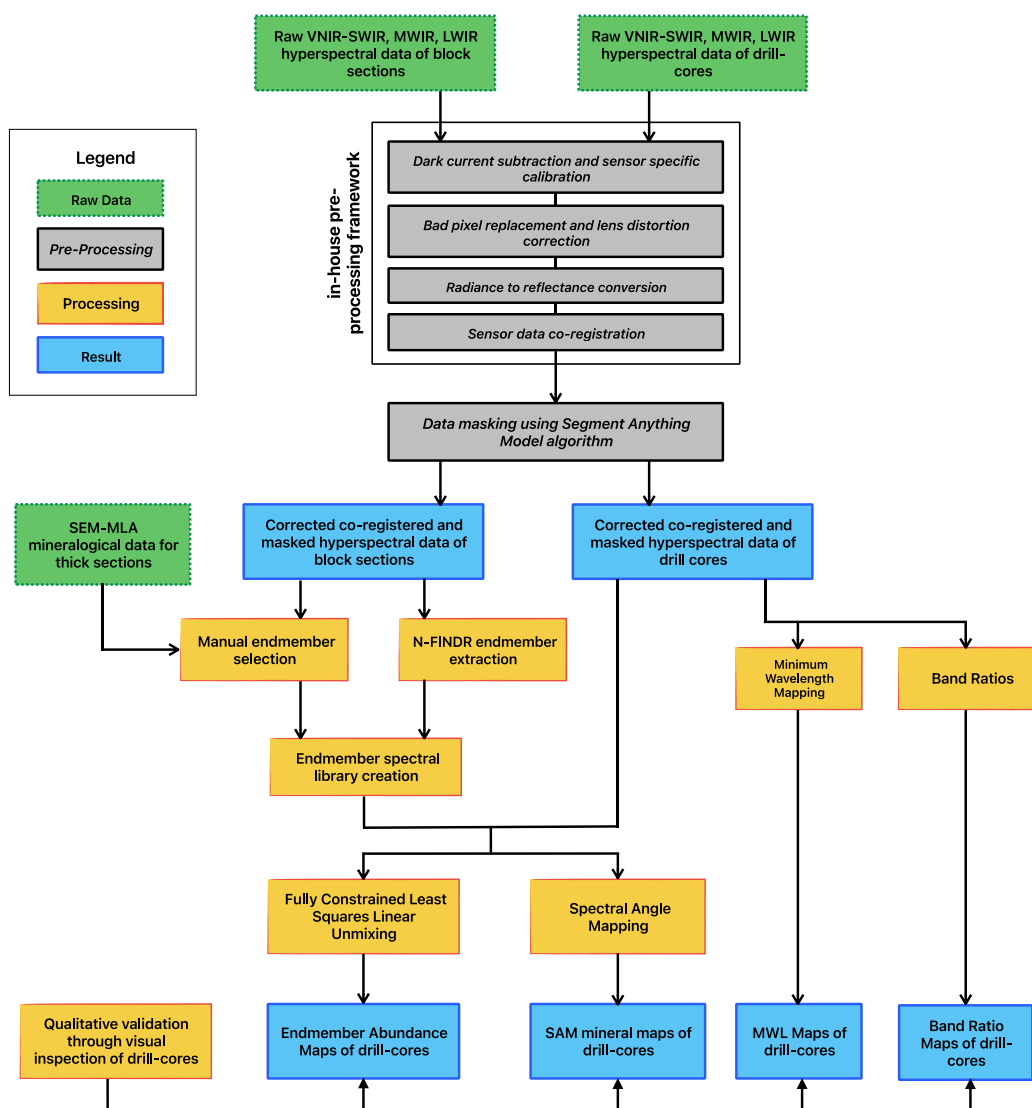


Figure 4.4: First stage of the developed workflow showing the processing steps of the hyperspectral dataset and the resulting outcomes.

The second phase of the workflow involves the identification and mapping the distribution of rare earth elements using laser-induced fluorescence spectroscopy. Nd-rich blocks and core pieces were identified primarily using the Nd feature minimum wavelength map generated from the hyperspectral data acquired in the previous stage. These selected samples were then scanned using the LiF setup and the data was corrected and masked. Using similar minimum wavelength mapping

techniques, peaks for different REEs were identified. In the end, the minimum wavelength maps created using the LiF data acquired on the block sections were compared to the available MLA maps to identify associations between minerals and REEs. This information was then extrapolated onto the core pieces and interpretations about the distribution of the REE across the drill core were made.

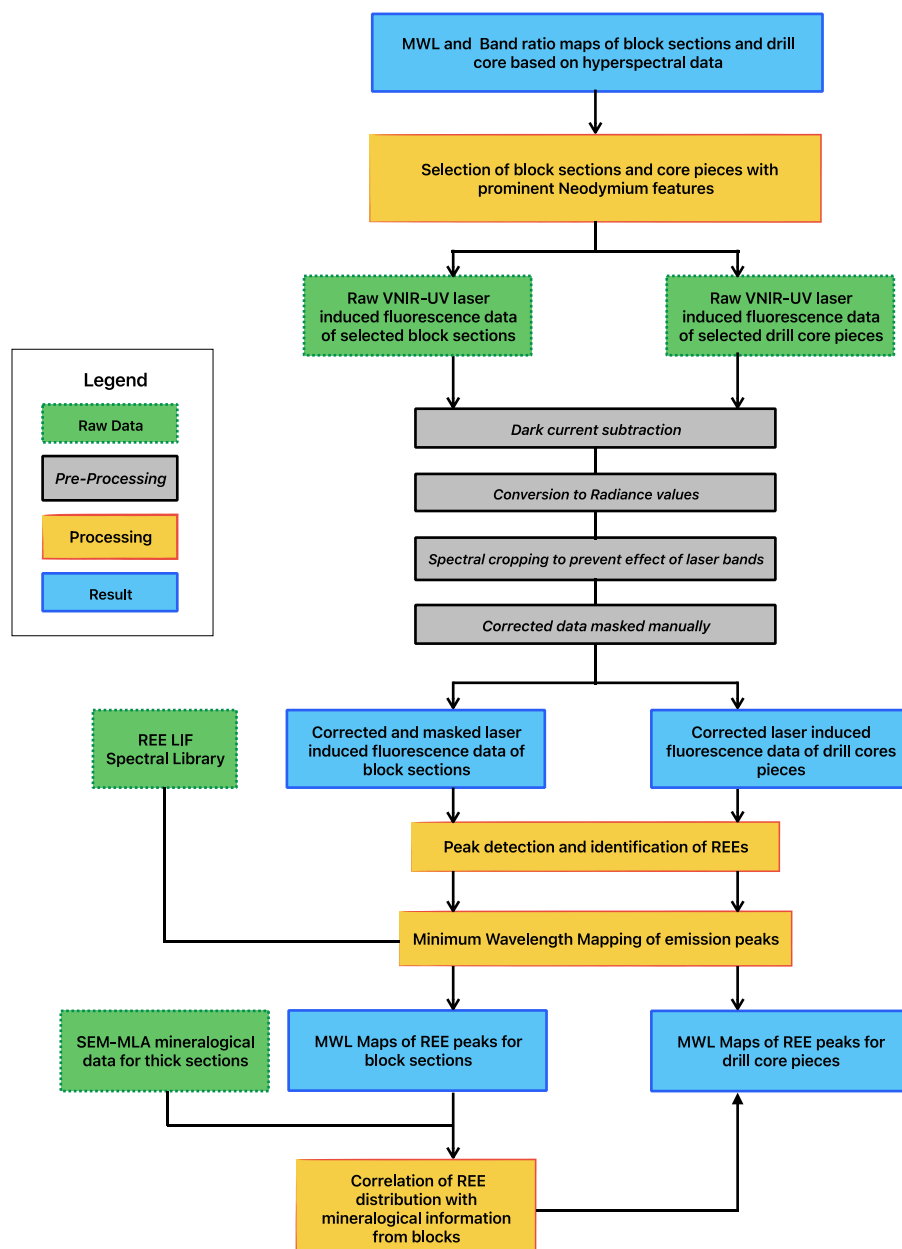


Figure 4.5: Second stage of the developed workflow to acquire and process LiF data.

Chapter 5 – Results & Interpretations

5.1 Sample Block MLA Mineralogical Results

The SEM-MLA data acquired from the thick sections formed the basis of all the mineralogical data used in this project by providing information needed during the manual verification of the endmembers and to correlate the regions of interest LiF to mineralogical zones in the blocks. The MLA Suite 3.1 software produced GXMAP maps for the ten thick sections that showed all the mineral classes present. However, for this project, this specific level of differentiation in classes was not required. Therefore, from the 52 mineral classes identified through the MLA analysis, the maps were regrouped and reclassified into 20 mineral classes which are based on similar chemical compositions or spectral responses. Most mineral classes are monomineralic but there are some exceptions. The plagioclase group is chiefly composed of albite with certain smaller quantities of other sodium-calcium feldspars. The amphibole class consists primarily of richterite with some lower amounts of unspecified Na-Ca amphibole and can be broadly considered as alkali-amphibole group here. The clay group represents the modal occurrence of both kaolinite and illite. The apatite class comprises mainly of the more abundant apatite, but very minor amounts of monazite observed in the samples is also considered within this group. The REE-fluorcarbonate class here only represents the bastnäsite mineral that was detected in these samples. The accessory mineral class is a broad class group that represents minerals that do not exhibit clear diagnostic features in reflectance spectroscopy like pyrite, zircon, sphalerite, rutile, ilmenorutile, and baddeleyite. The background material includes all the unknown, low count, epoxy, and glass zones.

The new mineral maps for each thick section are listed in Appendix 1.1. A granitoid lithology dominated by quartz, plagioclase and orthoclase with muscovite, chlorite, and clay is inferred for Block 01. Block 04 is inferred to show a similar granitoid mineralogy of quartz and feldspar but has also been biotized and has an alkali-amphibole and aegirine vein across the sample. In Block 03, the granitoid clast has also been fenitized which is observed by the presence of alkali amphibole and aegirine. Block 02 and Block 03 contain an intrusive breccia matrix mixture with granitoid clasts. It is observed that the matrix of the intrusive breccia is primarily composed of an ankeritic matrix but also contains varying concentrations of very fine-grained clasts or groups of orthoclase, quartz, sulfides, accessory minerals, chlorite, biotite, REE-fluorcarbonate, pyrochlore, and amphibole. This mixture is the primary lithology observed in Block 06. Block 13 also represents this intrusive breccia mineralogy but contains a large sulfide crystal and fragments of biotite. Block 10 contains a granitoid lithology, as seen in other samples crosscut by an REE-fluorcarbonate-ankeritic carbonatitic vein containing high amounts of calcite. It is interpreted that the lithologies observed here have been significantly altered based on the high abundances of biotite, amphibole, and aegirine. A similar lithology is observed in Block 08 which cuts granitoid mineralogy which is overprinted by fenitization. Block 05 depicts also ankeritic-carbonatitic lithology that shows

significant zones of REE-fluorcarbonate concentrations as well as biotite bands. Block X comprises an ankeritic-carbonatitic clast containing a large bleb of REE-fluorcarbonate in an intrusive breccia matrix. Block 05 only includes ankeritic-carbonatite with large zones of REE-fluorcarbonates between biotite mineral-rich bands.

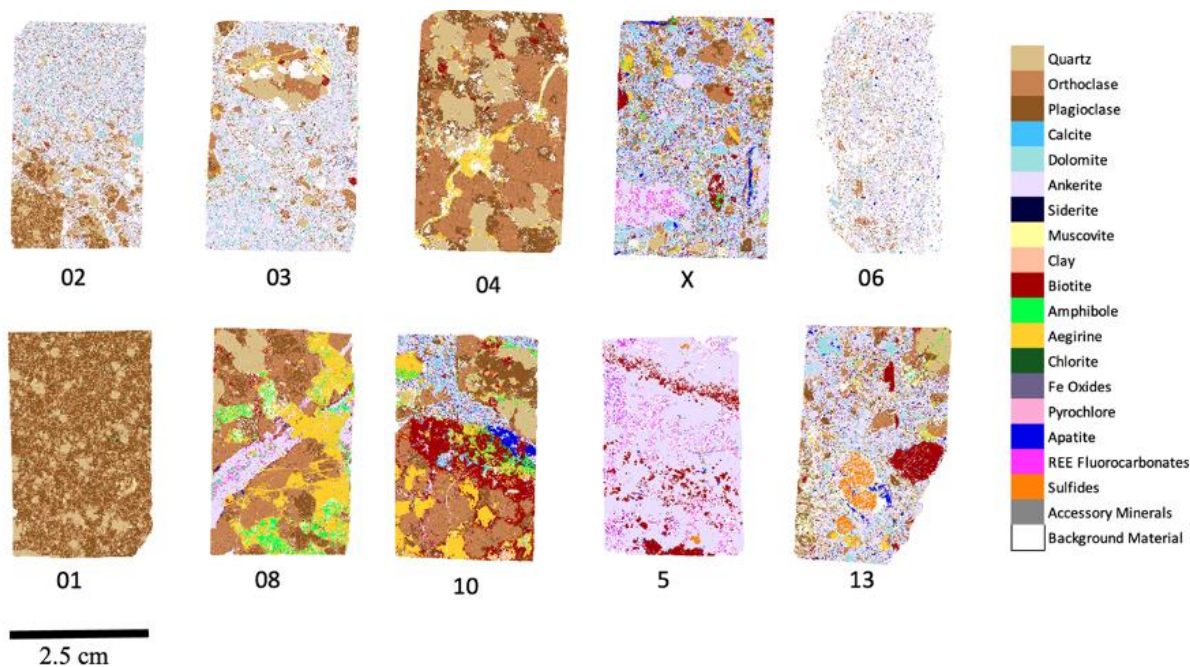


Figure 5.1: MLA maps showing the distribution of the 20 mineral classes for the ten thick sections.

For the easier visualization of the modal composition of each of the thick sections, the abundances of the mineral groups are illustrated in the bar graph in Figure 5.2. Across these samples, quartz, plagioclase, and orthoclase which is interpreted to represent the granitoid lithology of the host rock, occur in varying concentrations. These minerals are present in almost all the samples except Block 05. Block 06 is also the only sample containing plagioclase and orthoclase without quartz. Ankerite is the most abundant carbonate mineral found in all samples except in Block 01 and Block 04. It is observed to be the primary mineral of the intrusive breccia matrix and is also associated with the ankeritic-carbonatite. The concentration of ankerite varies depending on the extent of the breccia matrix or carbonatite that is present; however, the highest concentration is in Block 05, which contains 77.2% ankerite, followed by Block 06 with 64.50%. Dolomite and calcite are the other two carbonate minerals present in these samples. Dolomite is present in most samples where the ankerite is present except for Block 05 and 08 and calcite is only present with in these samples in Block 10 and X. The modal abundance of apatite mineral is minor in all samples except those containing the intrusive breccia lithology which contain 3.80% apatite on average. Small amount of apatite is also observed in the ankeritic-carbonatite between the large REE-fluorcarbonate zones

in Block 05. In most samples, the average REE-fluorcarbonate value is $\sim 0.5\%$ except for Block 05, Block X and Block 8 that contain 7.9%, 2.6% and 1.5% respectively.

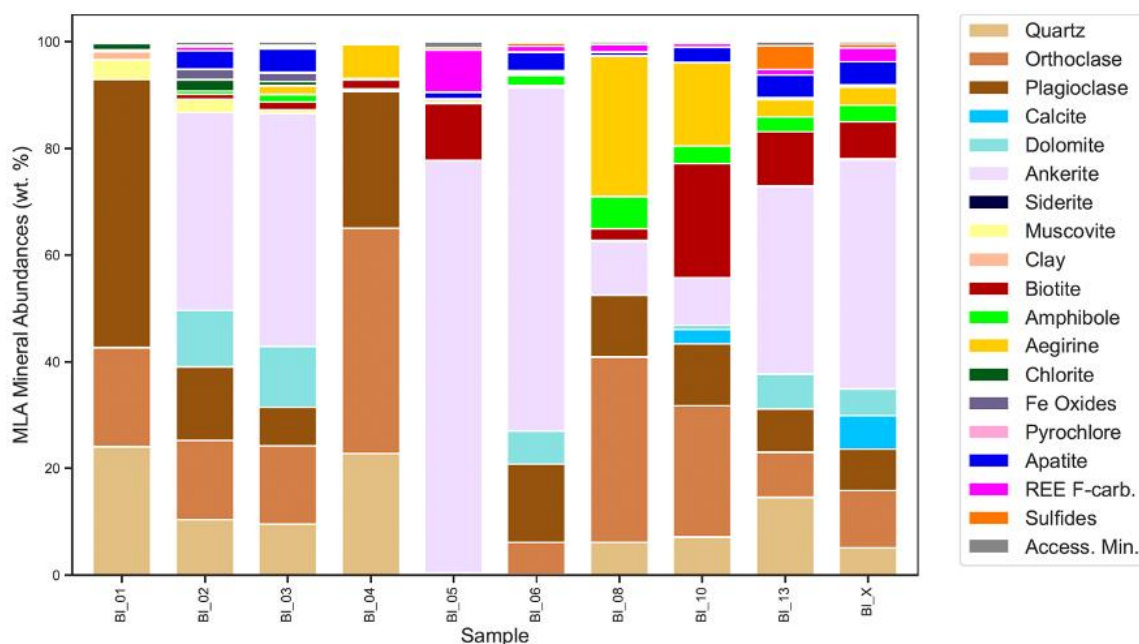


Figure 5.2: Modal abundances of each mineral class within the ten thick sections.

5.2 PCA and Elbow Plot Results

The results from visual assessment of the principal component analysis maps, elbow method, and silhouette score along with manual identification led to the final selection of the endmembers that are used further.

The results of the principal component analysis on the VNIR-SWIR, MWIR and LWIR data of the block samples are shown in Figure 5.3, only displaying the first three components with the highest variance. The visual assessment of the PCA map is a crude method to approximate the idea number of classes that can exist in the data. This approximation is fundamentally subjective since the number of different colored zones that can be differentiated in the image is determined by the viewer. Different zones are identified that represent spectrally distinct areas. This provides an understanding of the spectral variation in the data. In general, the number of unique regions of interest roughly represent the number of endmembers that could exist. From the VNIR-SWIR data, it can be observed that between 8 and 10 different colored zones exist; for the MWIR and LWIR data, it can be argued that ~ 7 and ~ 9 separate regions can be distinguished respectively.

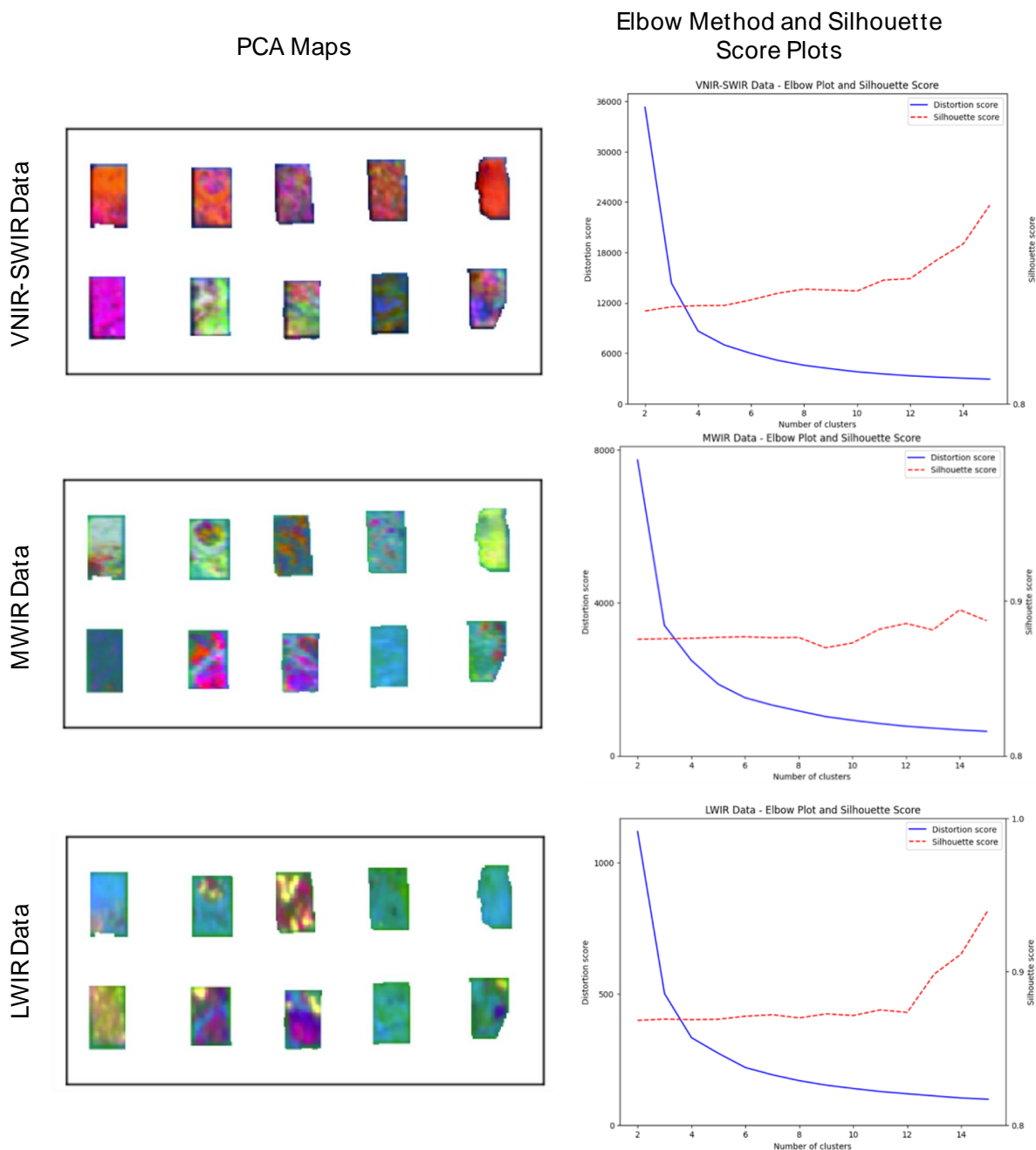


Figure 5.3: Visualization of the PCA maps for the block sections and the elbow method and silhouette score plots of the block data for each wavelength dataset.

On evaluation of the elbow plots generated on the three datasets (Fig 5.3), the elbow point and thus the optimal number of endmembers according to the elbow method for all the datasets was found to be four. However, from the mineralogical information combined with the PCA results, this number of endmembers would be too small to accurately represent the data. The resulting

endmembers would primarily be defined by the spectrally dominant minerals in that wavelength range which would not be wholly representative of the mineralogies present.

In comparison, the silhouette score plot (Fig 5.3) provided dissimilar results. For the VNIR-SWIR, MWIR and LWIR dataset, the number of optimal endmembers in these datasets would be 14. These would not be the optimal number of endmember classes for any of the datasets due to the over separation of co-existing spectral features that would occur. The process would ultimately create convoluted maps that would be significantly differentiated and would contain redundant information which would be detrimental to the subsequent geological evaluation.

Assessing the visual evaluation and other analytical metrics provided contrasting and varying results in the optimal number of classes. However, it was ultimately decided that nine endmembers would be extracted using the automatic extraction algorithm from each dataset.

5.3 Selected Endmembers for Each Dataset

After the nine endmembers were extracted and identified by evaluating the spectra, a manual verification of the endmembers was done using the mineralogical information and public spectral libraries (e.g., iSpec). Following this, the endmember library for each dataset was compiled where the first endmember always was a low reflectance value, highly mixed spectral signal, which is interpreted to represent the matrix and epoxy. An overview of each identified endmember for the three datasets can be seen in Table 5.1.

Table 5.1: All identified endmembers in the VNIR-SWIR, MWIR, and LWIR datasets (Cb: Carbonate, Amp: Amphibole, Bt: Biotite, Qz: Quartz, Aeg: Aegirine, Or: Orthoclase, Ab: Albite, REE-FI: REE-fluorcarbonate, Wm: White Mica). (Abbreviations based on Whitney & Evans, 2010)

	EM 1	EM 2	EM 3	EM 4	EM 5	EM 6	EM 7	EM 8	EM 9
VNIR-SWIR (S)	Matrix	REE-FI + Amp (minor Bt)	Cb + Amp	Cb	Cb + Bt	Wm + Clay	Cb + Clay	REE-FI + Bt + Clay	
MWIR (M)	Matrix	Cb + Amp	Bt	Cb	Cb + Bt				
LWIR (L)	Matrix	Qz (minor Bt)	Cb	Aeg + Ab	Or + Cb	Ab + Or + Bt	Bt (minor Cb)	Qz + Ab + Bt	Or + Aeg + Bt

In terms of the VNIR-SWIR data (Fig 5.4), one extracted endmember was removed because of the complex mixed spectral signal. A spectral library was created for eight endmembers in the VNIR-SWIR dataset. The second endmember shows REE features in the VNIR along with ~1250 nm and features for REE-fluorcarbonates. It also shows diagnostic features between 2300–2400 nm that are typical for amphibole (Kokaly et al., 2017). These features are also seen in FEM 3 which contains an additional carbonate feature between 2300-2360 nm (Kokaly et al., 2017). FEM 5 shows carbonate features along with characteristic features for biotite including an absorption at ~2350 nm (Kokaly et al., 2017). FEM 6 is a white mica-clay class because of the Al-OH feature

at ~2200 nm and the OH feature at 1400 nm are observed (GMEX, 2008). The seventh endmember is a carbonate-clay-REE-fluorcarbonate class. The term clay used in these endmembers is used as a broad label for the smectite group that is likely to be present based on the small 1400 nm OH feature, deep-water feature at ~1900 nm and the Al-OH feature at ~2210 nm. Although features specific to montmorillonite are observed, considering the variation between the spectral features, an inclusive label of clay is used. Based on the spectral features of the biotite endmembers observed, the magnesium-rich phlogopite endmember of the biotite solid solution series is likely to be present, however it is generalized as a biotite mineral.

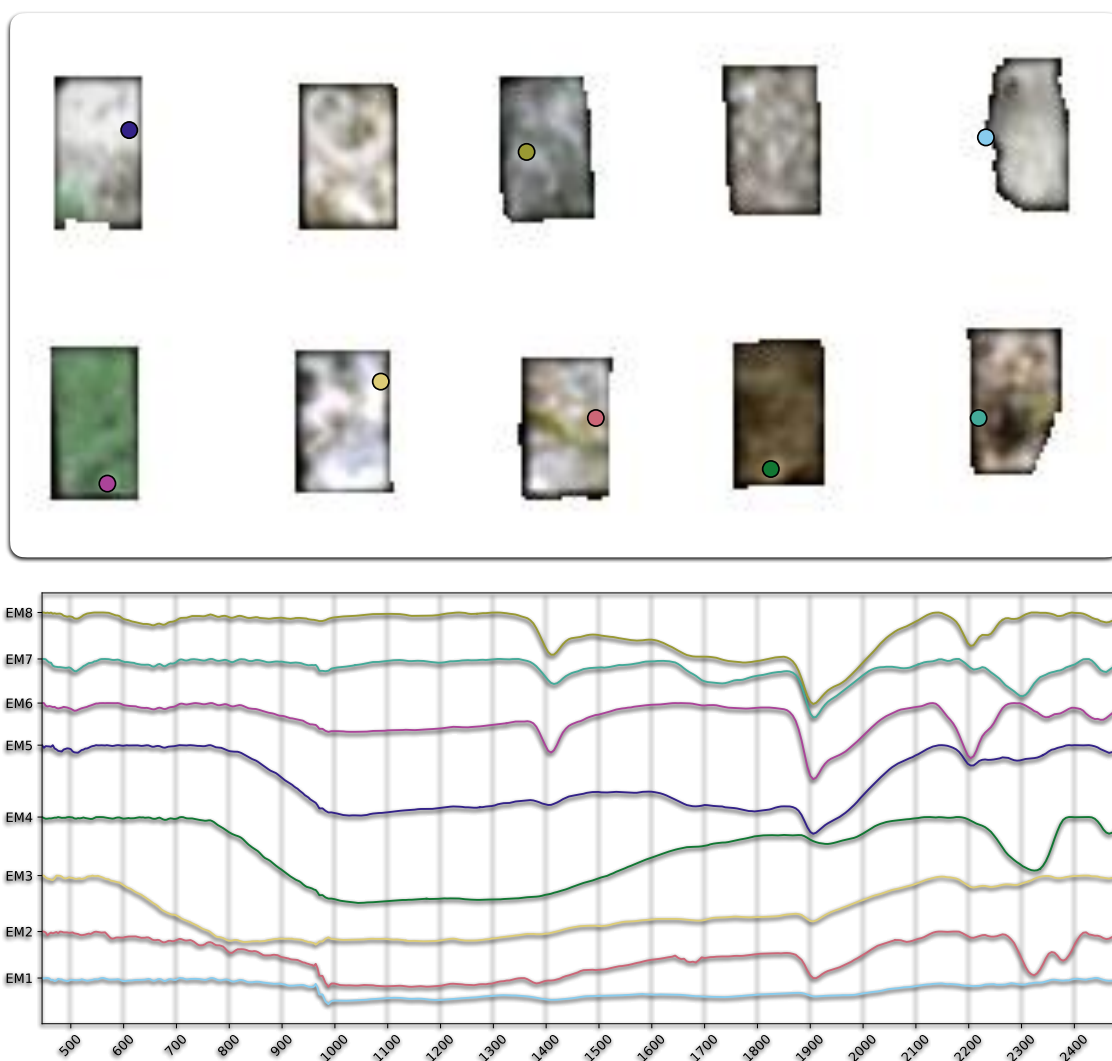


Figure 5.4: Pixel locations of the VNIR-SWIR endmembers as well as their respective hull-corrected spectra. (Reflectance spectra for each endmember offset for clarity)

In terms of the MWIR data (Fig 5.5), the overall characteristics observed between endmembers were similar in nature and only differentiated slightly in intensity and feature combination. This can be attributed to the fact that while characteristic spectra for different minerals do exist in the MWIR range, only some minerals have diagnostic features that can be easily distinguished (Laukamp et al., 2021). Consequently, only five endmembers were chosen to represent the data in the MWIR wavelength range. The second endmember identified showed features along with specific biotite associated features. The third endmember had a specific spectrum in this wavelength region that is diagnostic for a broad mica mineralogy (Laukamp et al., 2021). Within the observed spectra it was not possible to accurately distinguish features for specific mica minerals and therefore the endmember was largely identified as mica endmember. The fourth endmember had the characteristic features for carbonate around characteristic peak ~3900 nm and minimum ~3700 nm which can be attributed to carbonate (Gering et al., 2022). The final class contained features that allowed for it to be identified as carbonate-amphibole class.

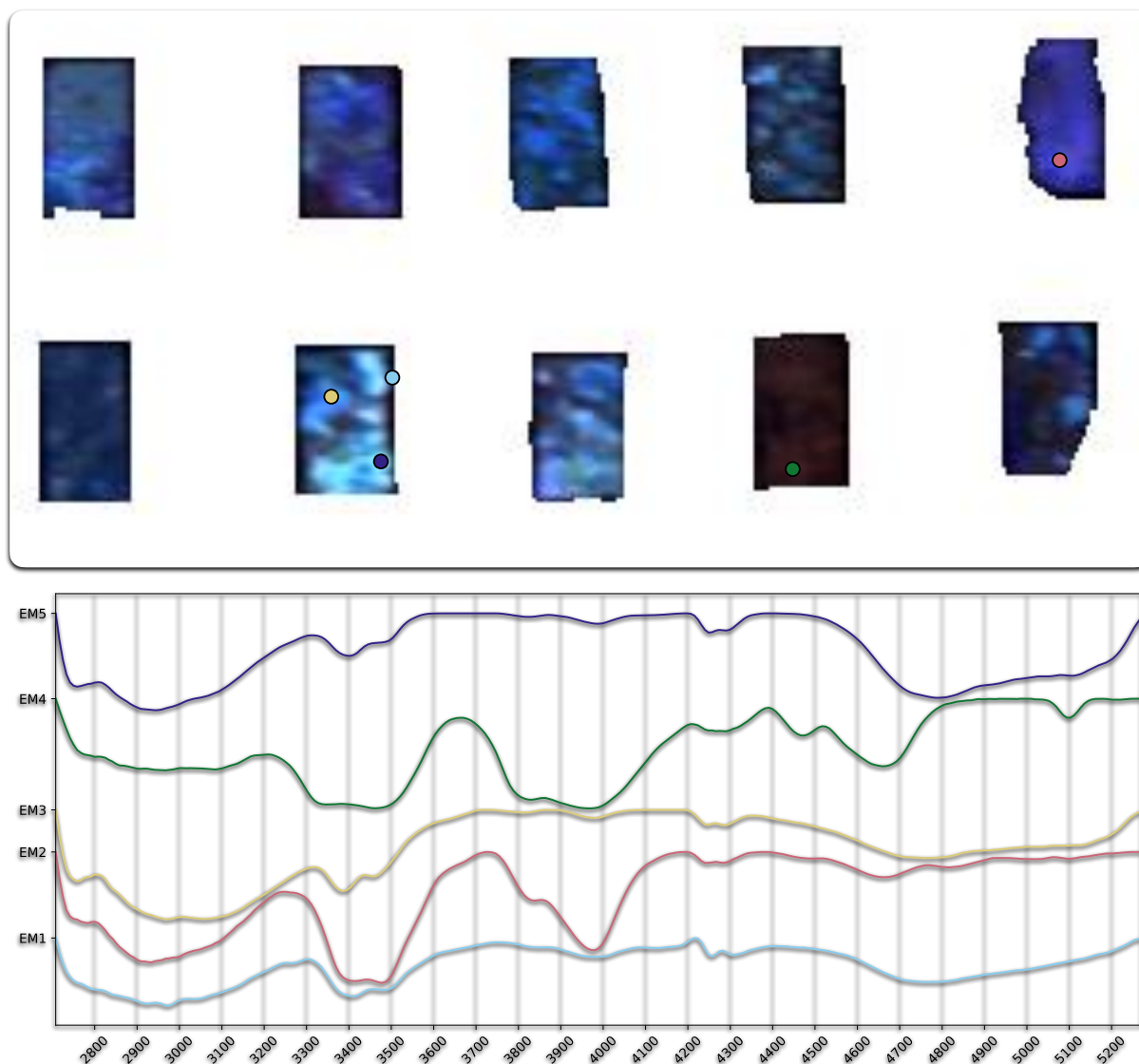


Figure 5.5: Pixel locations of the MWIR endmembers as well as their respective hull-corrected spectra. (Reflectance spectra for each endmember offset for clarity)

In terms of the LWIR data (Fig 5.6), the typical approach of the manual identification and evaluation of the endmembers within the available mineralogical context was done. Unlike the other dataset, the endmembers extracted from the block for this wavelength range were concluded to be sufficiently representative of the data. Therefore, no endmembers were removed or added, and a spectral library was created with nine endmembers. After the first matrix-epoxy class endmember, the next endmember class is quartz as distinguished by the typical restrahlen bands (~ 8250 nm & ~ 9200 nm peaks) as seen in its spectrum (Laukamp et al., 2021). The third endmember identified is a carbonate endmember detected by the characteristic ~ 11250 nm peak observed for carbonates (Laukamp et al., 2021). The next endmember groups represent mixtures that are prevalent within this sample. LEM 4 corresponds to a mixture of albite and aegirine

endmember which is indicated by the 8700 nm, 9200 and 9700 nm peaks (Kokaly et al., 2017) and 8700 nm, 9500 nm, and 9850 nm peaks (Hermann, 2019) respectively. LEM 5 indicates an orthoclase and carbonate endmember which is identified by the carbonate feature and the 8400 nm peak and 9020 absorption feature of orthoclase (Laukamp et al., 2021). The sixth endmember is aegirine-orthoclase-carbonate endmember that shows the characteristic peaks for aegirine. LEM 7 displayed a 9700 nm and a 10350 nm maxima attributed to biotite along with the carbonate peak (Kokaly et al., 2017). The next endmember had characteristic peaks and represented aegirine and biotite class. The last endmember was identified and categorized as an orthoclase-aegirine-biotite endmember.

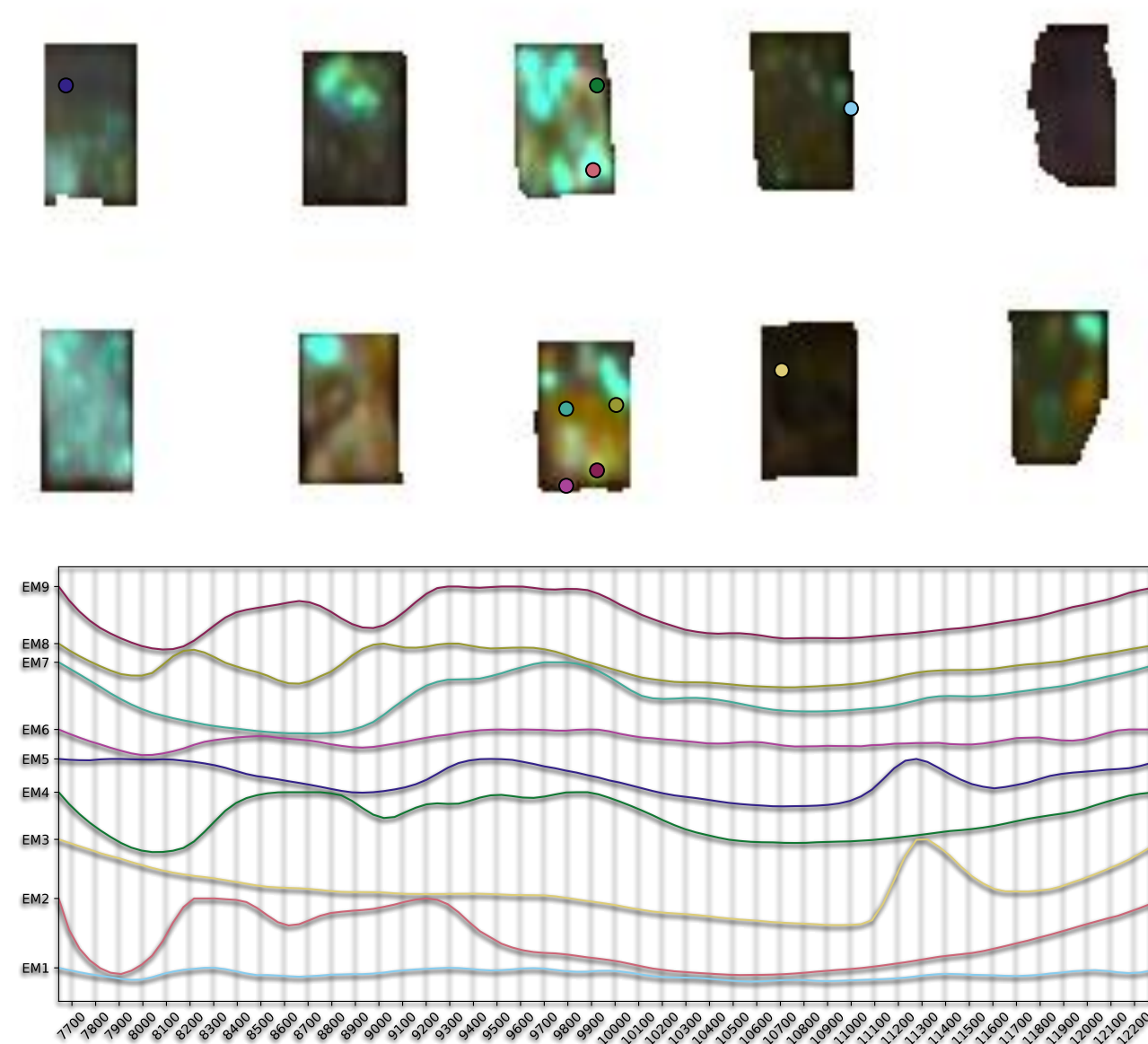


Figure 5.6: Pixel locations of the LWIR endmembers as well as their respective hull-corrected spectra. (Reflectance spectra for each endmember offset for clarity)

It is important to note that although this detailed approach for selection of the endmember was followed, given the limited spatial resolution of the hyperspectral data and the fine-grained nature of the Storkwitz Breccia, some endmember classes are still identified as mineral mixtures here. These mixed endmember classes are assumed to be sufficiently representative of the real mineralogy observed.

5.4 Fe-Oxide Band Ratio Map

By exploiting the band ratio technique, the abundance of different iron oxides was mapped as a false-color RGB composite of Fe^{2+} , Fe^{3+} and Fe-OH (Fig. 5.7). The different oxidation states observed here are associated with different mineralogical regions. Ferrous iron is the most abundant iron oxide. This iron feature is pervasive and present in almost every meter of the drill core interval. The ferrous iron ion is seen in the matrix of the central region of the Storkwitz breccia as well as associated with some clasts throughout the breccia. Some minerals that contain ferrous iron oxidation state that are associated with Storkwitz include ankerite, biotite, chlorite, and pyrite.

The iron-hydroxide phases are the second most abundant iron phase which is typically associated with amphibole or clay. In the upper margin section of the core, this iron hydroxide class can be seen in several rock fragments especially along the fault zone between 434 - 437 m. Several core fragments in this section are completely composed of this Fe-OH phase which is in contrast to the rest of the drill core. Within the central area of the intrusive breccia, iron hydroxide is observed to be associated with certain clasts and fragments and generally occurs randomly dispersed across this section.

Lastly, the ferric iron phase is the least abundant iron oxide detected. The Fe^{3+} ion is present abundantly within the upper margin section of the Storkwitz drill core and with certain core pieces that are closely associated with the iron hydroxide class. Within the central area of the Storkwitz core, the modal abundance of this oxide class is lower but still prevalent. The ferric oxides are found associated with the matrix of the intrusive breccia in random sections of the core as well as with certain clasts groups.

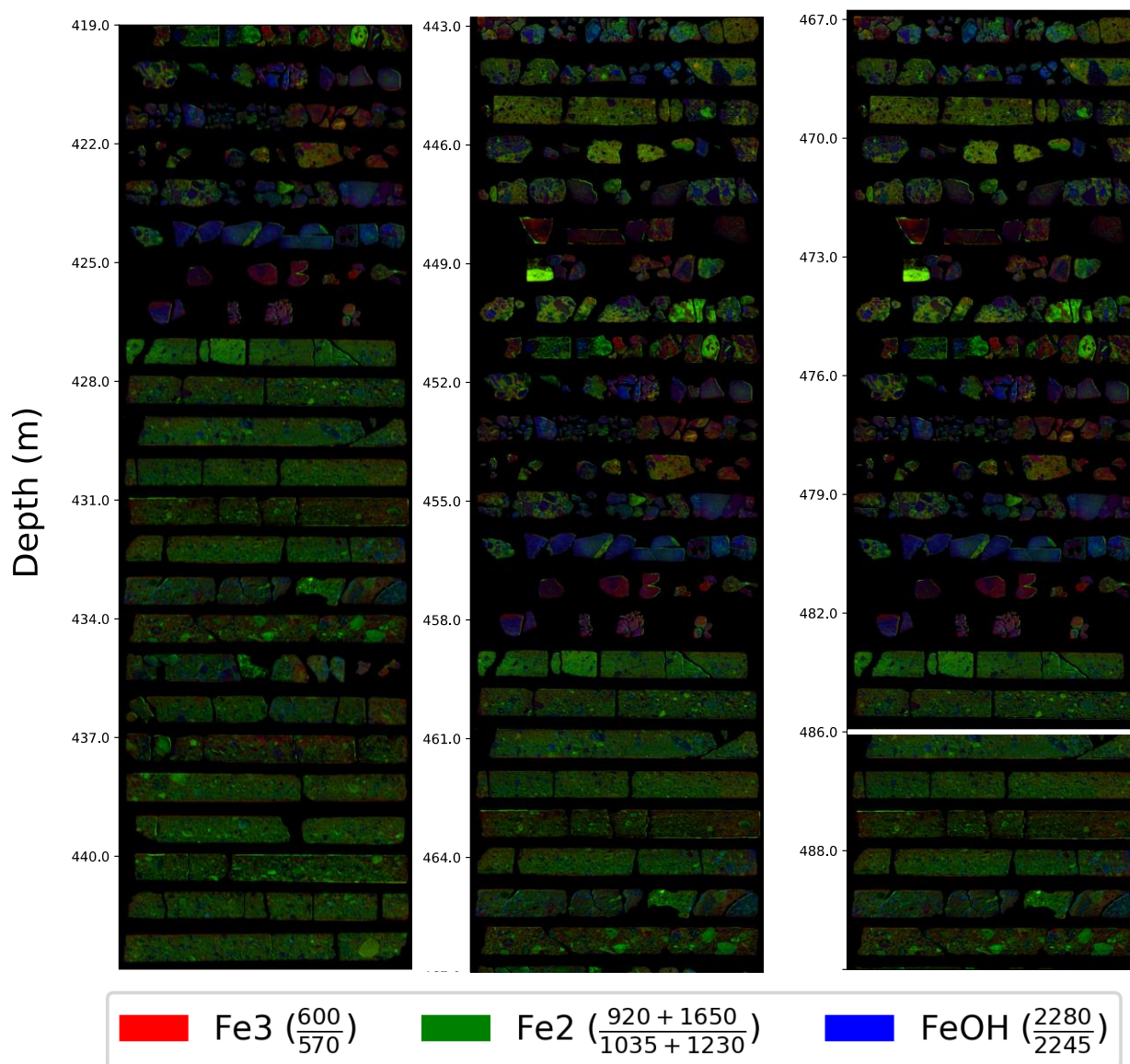


Figure 5.7: Band ratio map generated for three iron oxide band ratios utilized in the data.

5.5 Hyperspectral MWL Maps

Using minimum wavelength technique is useful for separating closely associated features within a spectral range due to the difference in position (hue) and intensity (brightness). It is used here to illustrate four spectral ranges and the associated minerals. It is important to note that the minimum wavelength maps chosen here were first verified by application on the blocks and then verified with the mineralogical data. The results of the minimum wavelength maps for the block section are in Appendix 1.3. and for the drill core interval is in Appendix 2.5.

5.5.1 Nd MWL Map

The resulting Nd MWL Map for the entire studied interval of the Storkwitz breccia can be found in Appendix 2.5. The brighter regions indicate a more concentrated accumulation of the neodymium and therefore potentially other REEs. The Nd MWL map shows the 419 - 437 m upper margin section of the core which includes this upper zone of the breccia, and only shows minor interspersed accumulations of REE rich zones. No REE rich areas are observed between specifically in the 434 - 437 section which is the fault zone region. The REE accumulations are higher in abundances in the rest of the drill core especially beginning from 439 m in the intrusive breccia lithology of the Storkwitz drill core. The REE rich zones (few cm in size) are seen associated with clasts in the drill core and are randomly distributed within the matrix. This result can be correlated to specific clasts within the Storkwitz breccia. An example of this observation is shown in Fig 5.8.

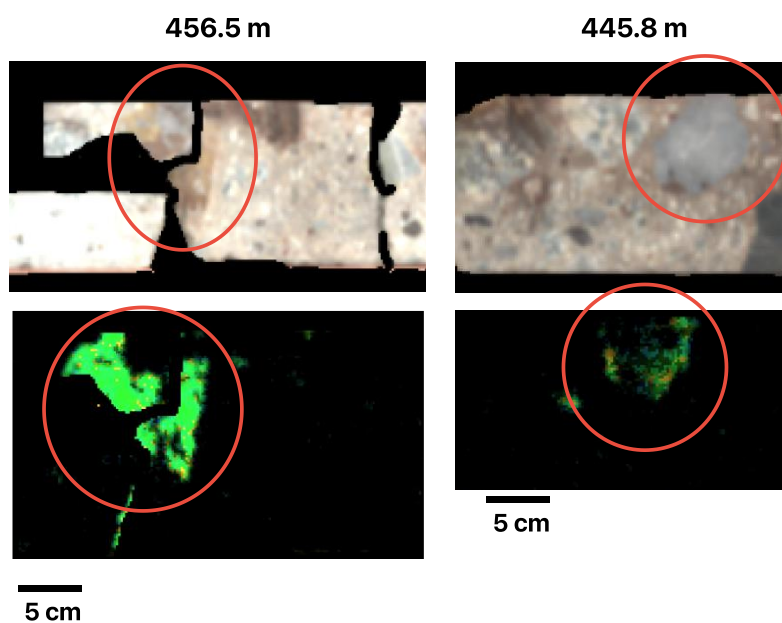


Figure 5.8: Comparison between the REE rich zones in the MWL map generated to the RGB image of the same core piece illustrating the accumulation of REEs in clasts.

5.5.2 Al-OH Feature MWL Map

The 2200 nm feature correlates to the AL-OH associated absorption feature for clays and micas (Laukamp et al., 2021; GMEX, 2008). As expected, a high modal abundance of white mica and clay exists in the upper zone of the Storkwitz especially visible in the fault zone (as seen in Fig 5.9). Within the intrusive breccia, the mica and clay content are minor and mostly present as a

pervasive material within the core pieces. The Al-OH feature and the inferred mineralogy is observed in certain clasts within the lower section of the intrusive breccia.

There are two Al-OH bearing minerals present here. After examining the spectral features of this class across the shortwave range, the group exhibiting spectral features at ~2210 nm is considered as white mica and a ~2200 nm feature is considered as clay. Based on this minimum wavelength map, it is inferred that this white mica is a muscovite with likely phengitic composition, and the clay can be further classified as smectite potentially montmorillonite. For the sake of simplicity, the mineralogies are only referred to as white mica and smectite.

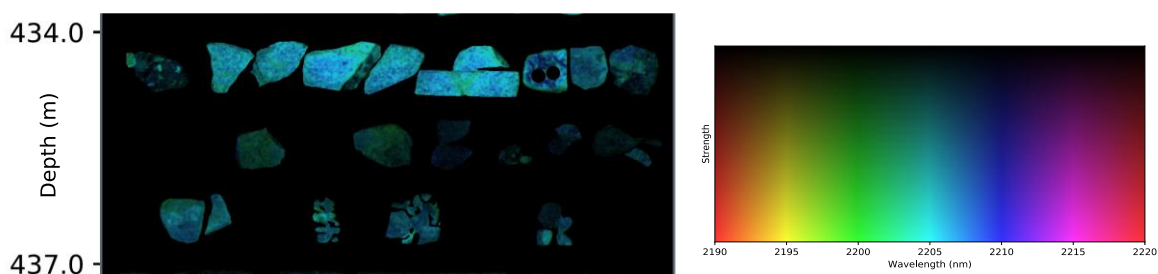


Figure 5.9: 434 – 437m section of core indicating the fault zone with high mica and clay content.

5.5.3 Quartz – Plagioclase – Aegirine – Mica MWL Map

The minimum wavelength map generated for the 8180 – 8900 nm range is important in differentiating quartz, plagioclase, aegirine and mica. Typically, the main feature for quartz is observed at 8260 nm, for plagioclase at ~8400 nm and for aegirine is at ~8600 nm. Within this spectral range a distinguishing feature at the higher wavelength (~8780 nm) is also observed which is correlated to the presence of mica.

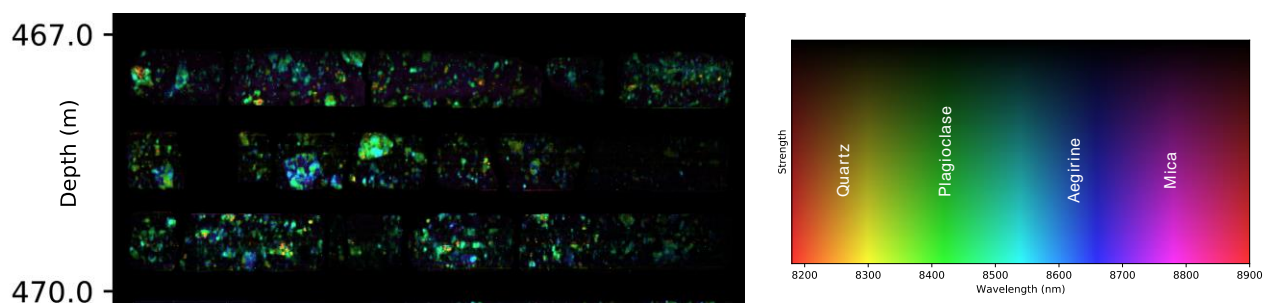


Figure 5.10: 467-470 m section of core indicating the different clasts associated with quartz, plagioclase, aegirine and mica.

On examination of the generated map, four combinations of quartz, aegirine, and plagioclase clasts exist. This can be observed in Fig 5.10 which shows 467–470 m section of the core. Firstly, distinct quartz regions (seen in orange) exist throughout the matrix as fine and large sized clasts. Secondly, there are distinct clasts where the quartz and plagioclase exist together which are characterized by the quartz peak being shifted to a higher wavelength representing a mineral mixture between quartz and plagioclase. These clasts are also associated with plagioclase rich zones (seen in green). Thirdly, plagioclase and aegirine rich clasts are observed. The plagioclase is seen to be shifted to a higher wavelength and in close association with the aegirine zones (seen in blue). Lastly, in lesser abundance, clasts containing quartz, plagioclase and aegirine are also observed within the sample. These are observed by the shifted wavelengths for quartz and plagioclase along with their close association to aegirine.

The majority of the mica rich regions are observed around the fault zone and in the upper margin of the drill core between 430 - 437 m. However, in the rest of Storkwitz interval, scattered mica dominated regions are observed in lower abundance and usually exist as a pervasive zone within the core pieces rather than distinct clasts. The mica rich zones are not found to be closely intermingled with the quartz, plagioclase or aegirine zone but rather in close proximity around these regions.

5.5.4 Carbonate MWL Map

For the Storkwitz samples, the distinct carbonate feature in LWIR was used to map the distinct carbonate mineralogy that exists within the Storkwitz lithologies. The map (in Appendix 2.5), which was generated for all the entire drill core interval, clusters the carbonate-bearing lithologies into three main groups that are identified: dolomitic (~11220 nm), ankeritic (~11300 nm), and calcitic (~11400 nm). This map particularly highlights the widespread distribution of the ankeritic carbonate class. This map also highlights the different mineralogies of the carbonatitic clasts that are dispersed within the drill core interval. Given the close mineral association and mixtures observed within these carbonatitic clasts, two subcategories are also identified which indicate the presence of a dolomite-ankerite mixture and an ankerite-calcite mixture.

5.6 Abundance Maps from Spectral Unmixing

The FCLS spectral unmixing that was performed on the drill core data produced individual abundance maps for each endmember in each wavelength range. These were organized together based on the wavelength ranges (Appendix 2.1). The resulting individual map illustrating the abundance of each endmembers were compiled to create three maximum classification maps for each dataset (Appendix 2.2).

According to the abundance maps from the first dataset (FENIX 1-8), the white mica-clay endmember is the most abundant mineral group in the VNIR-SWIR data. Additionally, it is observed that the carbonate-clay-REE-FL endmember is also an abundant class in the VNIR-SWIR data which is closely associated with white mica-clay class. It is typically found in higher quantities in zones where lower quantities of white mica-clay are present. The biotite-amphibole-REE-FL endmember is closely associated with the carbonate-clay group but only occurs in minor quantities associated with some clasts within the interval. The compiled maximum abundance map for the VNIR-SWIR data, also referred to as the FENIX classification map is found in Appendix 2.2.

There are five abundance maps (FX50 1-5) that were generated from the mid-wave data corresponding to the respective endmembers. It is important to note that the mid-wave data for the first drill core tray scanned (419-422 m) was corrupted and therefore the data is not included in any interpretation or discussion. Within the individual abundance maps, the highest modal abundance is seen for matrix endmember which covers significant portions of the drill cover interval. This endmember is associated with the low-intensity background data. Subsequently, the second most abundant class is the carbonate class. This either exists as dispersed with the sample or in the form of distinct clasts around 437-440 m, and in small sections between 455-467 m and 476-485 m. The carbonate-amphibole, biotite and carbonate-biotite endmembers are present in smaller quantities in the interval and typically closely associated with the carbonate class. The carbonate-biotite is generally observed as a pervasive class in the core piece, but the biotite/mica and carbonate-biotite endmembers are seen associated with clasts.

In the LWIR dataset with nine endmembers, the most abundant endmember similar to the mid wave data was found to be the matrix endmember. The second most abundant class was the orthoclase-carbonate class which covers significant portions of the core piece in the lower section of the Storkwitz breccia. Quartz and carbonate endmembers are seen as clasts distributed randomly within the orthoclase-carbonate class. The biotite-carbonate endmembers also form similarly distinct clasts across the core. The orthoclase-aegirine-biotite endmembers are also seen in higher quantities in the upper margin of the core but are present as minor quantities of clasts within the rest of the section as well. The aegirine-albite endmember is seen to exist in close relationship with the quartz endmember. The individual abundance maps of the nine endmembers for this range (OWL 1-9) are found in Appendix 2.1.

Comparing the generated individual abundance maps between the datasets provides information about the relationship between different mineralogies as well as provides validation of the similar mineralogies identified in the different wavelength ranges. The abundance maps for the carbonate-amphibole endmember in shortwave and mid-wave data show a similar distribution of classes. However, the data in the mid-wave is significantly less abundant and only categorizes the concentrated features seen in the shortwave abundance map. Across the three wavelength ranges,

the distribution of the carbonate and carbonate-biotite endmembers are relatively similar. However more regions are identified as carbonate biotite zones in mid wave abundance maps than the shortwave and long wave maps. The white-mica-clay and carbonate-clay clasts in the shortwave are seen to exist closely with the regions that contain abundant orthoclase-carbonate class. The abundance of the carbonate-amphibole class is also comparable to the orthoclase-carbonate class. The modal distribution of the carbonate-biotite endmember can also be attributed to that of the orthoclase-aegirine-biotite endmember.

5.7 SAM mapping

Spectral angle mapping technique utilized with the respective endmember data generated spectral angle maps for each wavelength range. The individual SAM maps can also be found in Appendix 2.3. Using the eight endmembers selected for the VNIR-SWIR data; the spectral angle mapping algorithm can map its occurrences throughout the drill core. This resulting spectral angle map created is referred to as the FENIX-SAM map. In the midwave dataset, the first tray is not included in the generated SAM map since the data acquired from this sensor for this tray set (419 - 422m) was corrupted. The FX50 SAM map that refers to the spectral angle mapping result conducted on mid wave dataset. As it can be observed, the most abundant class here is the matrix endmember. Minor abundances of the unclassified class are observed in the data. The OWL-SAM map refers to the result of the spectral angle mapping that was performed on the long-wave data using the relevant endmembers. Across cores interval small sections of the matrix endmember are present along with minor abundance of the unclassified class

5.8 Validation

Several points across the generated maps were chosen to be verified with existing lithologies using common field techniques. In terms of carbonate validation, the acid test was used to differentiate and confirm the occurrence of the different clasts observed in the carbonate MWL map as well as the spectral angle mapping and abundance maps. The difference between the calcitic abundant, dolomitic dominated and ankeritic clasts that is observed in the carbonate minimum wavelength map is confirmed based on the speed of the reaction of the acid test. The reaction seen from ankeritic matrix and ankeritic clasts was significantly slower and produced less noticeable effervescence than that for dolomite. Calcite rich clasts had the fastest reaction. These carbonate tests were used to check the core piece at 486.4 m (Fig. 5.11). The two clasts were confirmed as ankerite carbonatitic clasts in an ankeritic matrix. While the MWIR-SAM map, and OWL-SAM represented this result for the clast and the FENIX classification map depicted the carbonate matrix, the FENIX-SAM map incorrectly classified both the clast and the matrix. Field tests using acid across various points in the matrix portion of the cores confirmed that the majority of the matrix is carbonate hosted. This again differs from the map that was

FENIX-SAM map which illustrated that the matrix was primarily amphibole dominated with only some regions being carbonate dominated.

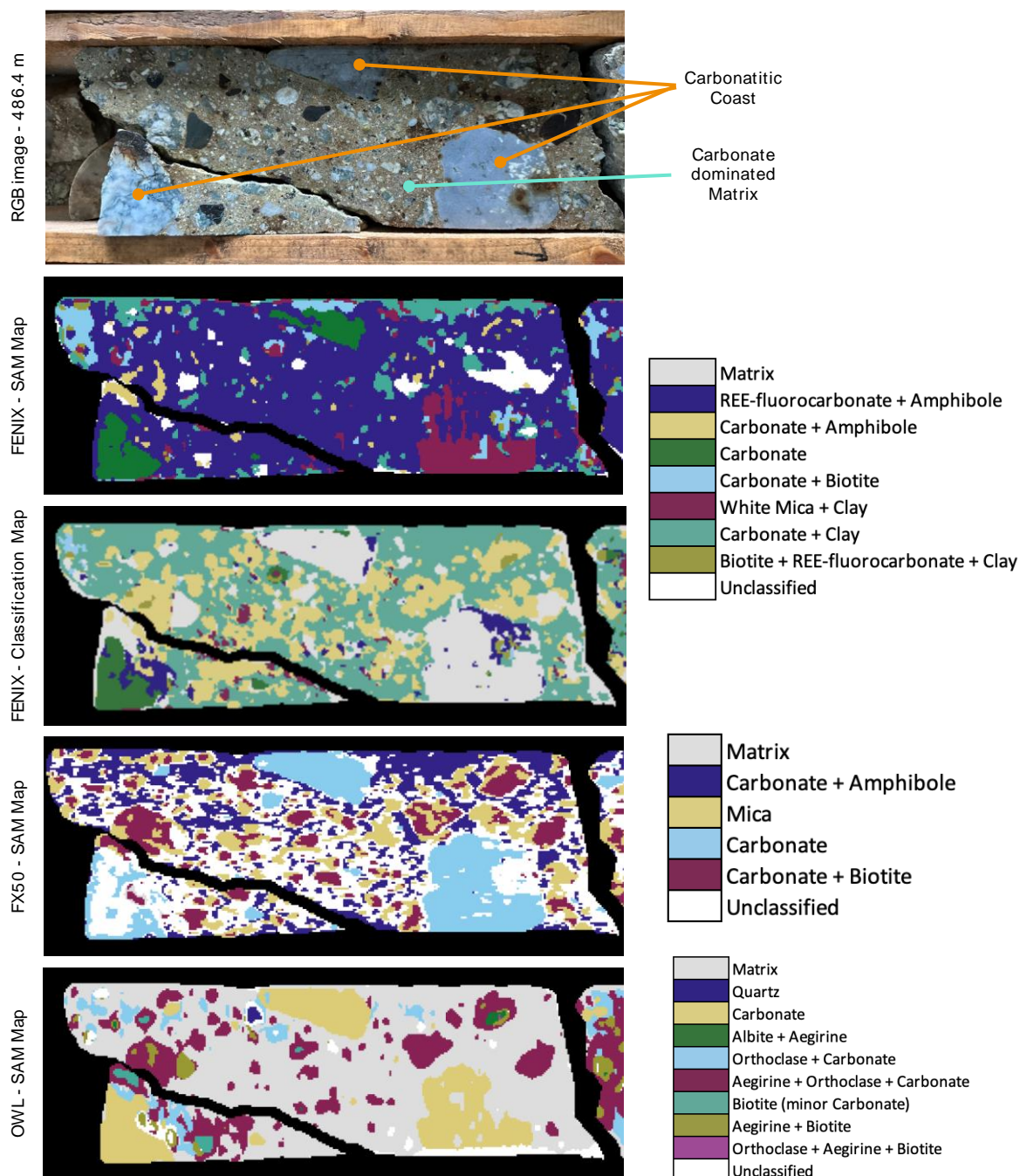


Figure 5.11: RGB image of the core piece at 486.4 nm and the corresponding maps short-wave, mid-wave, and long-wave maps to compare the lithologies identified to the ones mapped.

The difference between quartz and plagioclase was done based on the color as well as a scratch test. Color was used to differentiate between orthoclase and aegirine. Orthoclase rich were observed to have a dark pink hue whereas, aegirine could easily be identified and differentiated based on its green-dark green color. Biotite clasts were successfully identified in the field using a scratch test and comparing the color, luster, and cleavage. The results of comparing these lithologies which are seen in the OWL-SAM map are shown in Fig. 5.12. This test confirmed the mapping accuracy for the OWL-SAM map where the zones classified as aegirine, albite, quartz and orthoclase could be accurately correlated to the clast mixtures observed in the core.

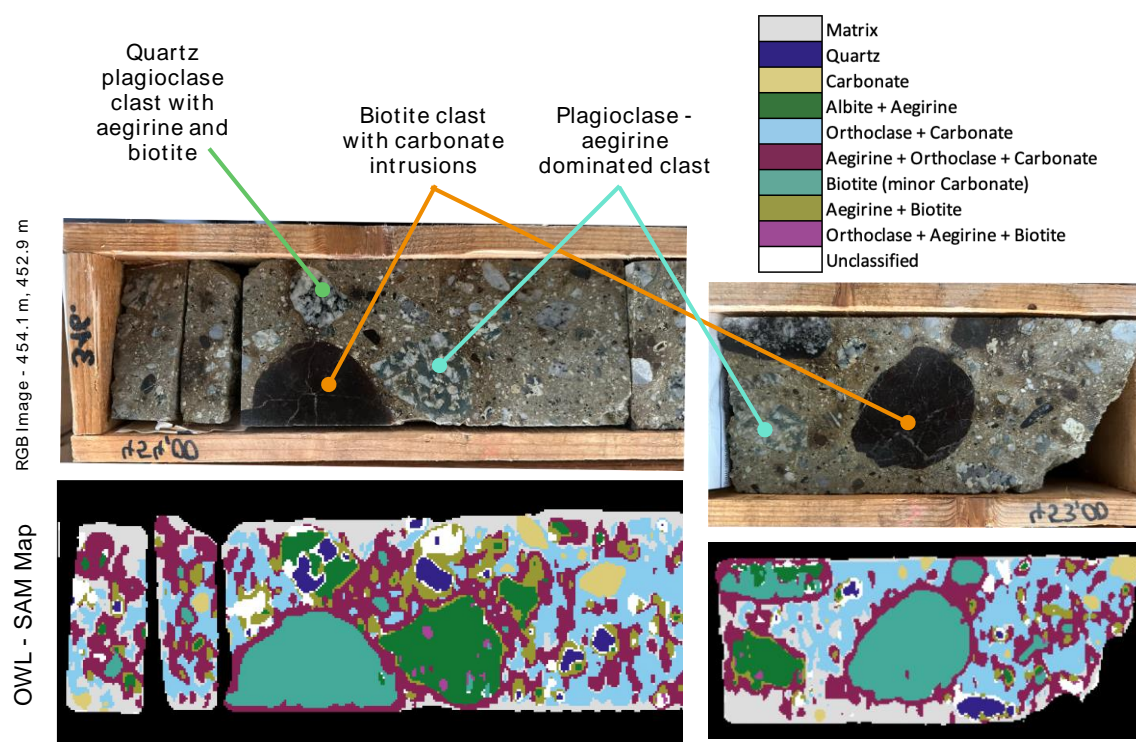


Figure 5.12: RGB image of the two core pieces at 454.1 m and 452.9 m and their corresponding long-wave SAM map to verify the quartz, plagioclase, aegirine and biotite mineralogy.

As mentioned before several regions of the drill core were covered in epoxy. One zone was identified and compared to the two maps generated for the VNIR-SWIR range. The epoxy zones are incorrectly classified as the REE-fluorcarbonate-amphibole class in the FENIX-SAM but accurately classified as a matrix background class in the FENIX classification map. Ultimately, this comprehensive approach provided the validation necessary to verify the quality of the maps generated from the identified endmembers. It was concluded that for the visible-shortwave data, the FENIX abundance map provides the most accurate representation of the existing lithologies. Alternatively, the FX50-SAM and OWL-SAM maps are the most appropriate at correctly illustrating the variation that is observed in the mid-wave and long-wave data respectively.

5.9 Spectral Characterization of Storkwitz Breccia

The following interpretations on the composition and texture of the Storkwitz Breccia are primarily based on FENIX-classification map, the FX50 and OWL SAM maps as well as the iron oxide band ratio and the HSI minimum wavelength maps. The main lithological units within the breccia in this study interval include the matrix and the diverse clasts that have undergone varying degrees of alteration. Based on the OWL-SAM map and particularly the Carbonate MWL map, it can be interpreted that the breccia matrix predominantly composed of ankerite. Additionally minor amounts of white-mica, clay iron oxides and REE-fluorcarbonates are also present. The breccia matrix is the groundmass that hosts the clasts discussed below.

Clasts

The first most abundant clast observed is predominantly in association with orthoclase. As observed in the OWL-SAM, extensive regions of the sample are covered in the orthoclase-carbonate class which is fundamentally indicative of fine sized orthoclase rich clasts in a carbonate rich matrix. A close relationship between the distribution of the orthoclase-carbonate class and other classes like albite-orthoclase-biotite, aegirine-orthoclase, and quartz-albite-biotite, is extensively observed across the core. The regions where this clast exists are also regions in the core sample characterized by the abundance of amphibole and aegirine. Therefore, it can be inferred that these clasts represent the one type of the granitoid lithology of the host rock which has been variably altered and is mainly composed of orthoclase with plagioclase and lower quantities of quartz, biotite, aegirine and amphibole (Fig. 5.13)

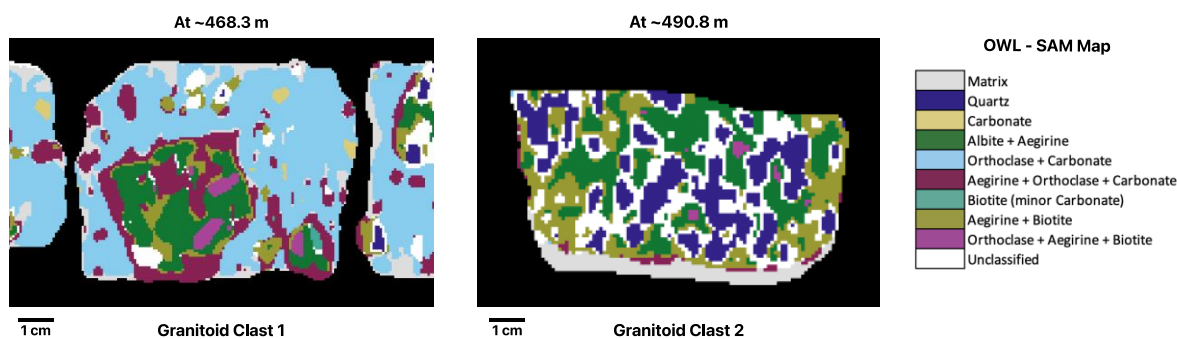


Figure 5.13: OWL-SAM maps illustrating the two types of granitoid clasts that are observed.

Another set of clasts are characterized by the mutual occurrence of quartz with minor biotite and the quartz-albite-biotite class. This clast group is separated out from the previous clast category due to the lower orthoclase abundance associated with these clasts. This clast group occur widespread across the matrix and are accompanied by the presence of biotite, aegirine and

amphibole. They also exhibit alteration towards clay and white mica. In the end, this clast group is interpreted as the second type of granitoid lithology that is composed of high quantities of quartz and albite with lower abundance of orthoclase and with the presence of biotite, aegirine, and amphibole. Similar to the first identified country rock clast group, this granitoid lithology also displays a low degree of alteration dominated by clay formation.

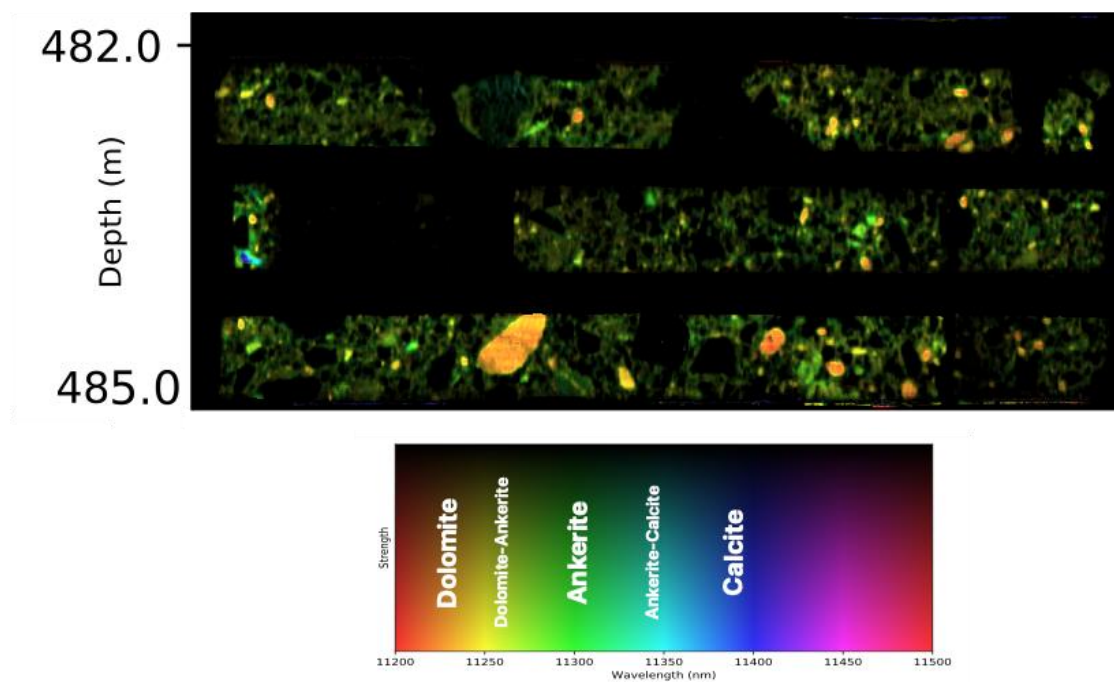


Figure 5.14: 482-485 m section of core indicating the different carbonatitic clasts present in the drill core.

Carbonate class clasts are significantly widespread in distribution throughout the drill core. The mineral maps particularly OWL-SAM maps identify a group of carbonate clasts within the matrix, these clasts refer to the carbonatites that are dispersed throughout the sample. By correlating the clasts identified carbonate MWL map generated, three types of carbonatitic clasts can be inferred (Fig. 5.14): (1) several small ankerite clasts that are identified by their jagged shapes (seen in green), (2) dolomite dominated clasts (seen with orange color) and (3) ankerite clast with some amount of calcite also present (seen in blue and purple). Firstly, the ankeritic carbonatites are the most abundant clast group present within the core interval. These clasts are observed to contain varying amounts of amphibole, and REE-fluorcarbonates. The associated bright ferrous features also observed in the Fe-Oxide map suggests the presence of iron sulfides and oxides within these clasts. Some minerals that contain ferrous iron oxidation state that are associated with Storkwitz include biotite, chlorite, and pyrite. Occasionally, some minor alteration of clay is also observed to be associated with this clast group. The second group of carbonatites is the dolomite dominated carbonatites with smaller quantities of ankerite. Given the close association of these classes with these clasts, these clasts likely contain minor quantities of REE-fluorcarbonates, amphibole, and biotite. Additionally, these typically form large clasts that exist within the matrix and correlate to

some REE-rich clasts seen in the REE MWL map. Lastly, the least abundant is the ankerite- calcite carbonatites which are observed as small, rare clasts within the core interval. These clasts likely contain the highest amount of calcic content within the breccia and the REE-fluorcarbonates associated with these clasts can be inferred to be synchysitic in composition.

Other than the different granitoid clasts and the carbonatitic country clasts, two other sedimentary clast types are observed. Across the core interval, quartz clasts of varying sizes are observed within the sample. Additionally, the biotite clasts are also observed. Although biotite is predominantly seen accompanying the granitoid and carbonatitic clasts, it also occurs as large crystals within the samples. Across several biotite clasts in the Storkwitz core, carbonate is also closely associated. Several biotite clasts are also categorized as biotite-carbonate class. This can be potentially explained by the presence of carbonate veins cross cutting the biotite crystals.

Alteration

Within Storkwitz breccia, four types of alterations are observed across the drill core interval. The first alteration phase identified is the fenitization that is observed in the drill core. The extent of fenitization is indicated by the widespread occurrence of alkali rich amphibole and aegirine. The individual abundance maps for the mineral classes with aegirine and amphibole indicate that these minerals typically always exist together. As evidenced by the FENIX-abundance map and the OWL-SAM map, a significant majority of the clasts have been affected by the fenitization. The second alteration sequence is associated with the occurrence of biotite which is typically observed to exist both independently and closely associated with aegirine, amphibole and clay. The regions of extensive biotite alteration are observed to be in close relationship with the fenitized zones. It is important to note that the distribution of these two alteration assemblages depict pervasive alteration sequences within the core. Both these alteration events are abundantly observed to be associated with the granitoid clasts and with carbonatitic clasts to a lower extent.

The third alteration phase refers to the distribution of white mica and clay that is observed across the drill core. White mica and clay associated together as one assemblage because of the intimate relationship between these minerals. As seen in the FENIX-classification map, white mica-clay endmember is the most abundant mineral group in the VNIR-SWIR data and is found to exist in almost every meter of core. While this class is generally found in low amounts intermixed throughout the core, it is found in the higher quantities in specific intervals between 437 - 440 m, 458 - 468 m and 488 - 491 m and is most concentrated in the upper margin section of the core (i.e., 419 - 437 m). The white mica alteration is primarily demonstrated by the occurrence of muscovite. On examination of the Fe-oxides map, regions with high Fe-OH contents are observed throughout the sample especially within the upper margin section of the drill core. These regions are observed to co-exist with the clay rich zones seen in the FENIX-classification map. Therefore, the potential existence of montmorillonite as the primary clay feature is also strengthened by the coexistence of

the Fe-OH regions. Montmorillonite can contain is Fe-OH bond and can be thus attributed with the supergene alteration of the core. This clay alteration within the lower portion of this drill core is also largely correlated with the alteration of granitoid clasts. This can be indicated that the country rock clasts underwent significant muscovite and smectite alteration in the later stages of the Storkwitz carbonatite evolution.

Lastly, a prevalent ferric alteration is seen with the groundmass of the breccia on examination of the Fe-oxide band ratio map. It is also observed that biotite clasts that contain minor amounts of carbonates also contain presence of these iron oxides. It is inferred that the Fe-rich minerals like ankerite and biotite are locally partially broken down, resulting in the exsolution of Fe-oxides. Some minerals that contain ferric iron oxidation state that could be associated with this iron phase include hematite, goethite, and limonite.

5.10 Laser Induced Spectroscopy of Storkwitz Samples

The results and interpretations of the LIF spectroscopy data are divided into two sections. The first section considers the library of spectra that was created from the block sections that is representative of the spectral mixture observed within the core pieces as well. It also displays the results of the peak detection that was done on the block section spectra along with false color images to map the spatial correlation of the peaks. The second section considers the minimum wavelength maps that were created for the block sections as well as the core piece.

5.10.1 Peak Detection

Initially, a minimum wavelength map which was created across the broad VNIR range (580 – 900 nm) for the block section and core piece is shown in Fig. 5.15. This visualization shows areas with similar emission peaks and confirms the likeness in spectral variation that exists in the blocks sections and core pieces. This ensures that the interpretations made in the blocks can be applied onto the core interval.

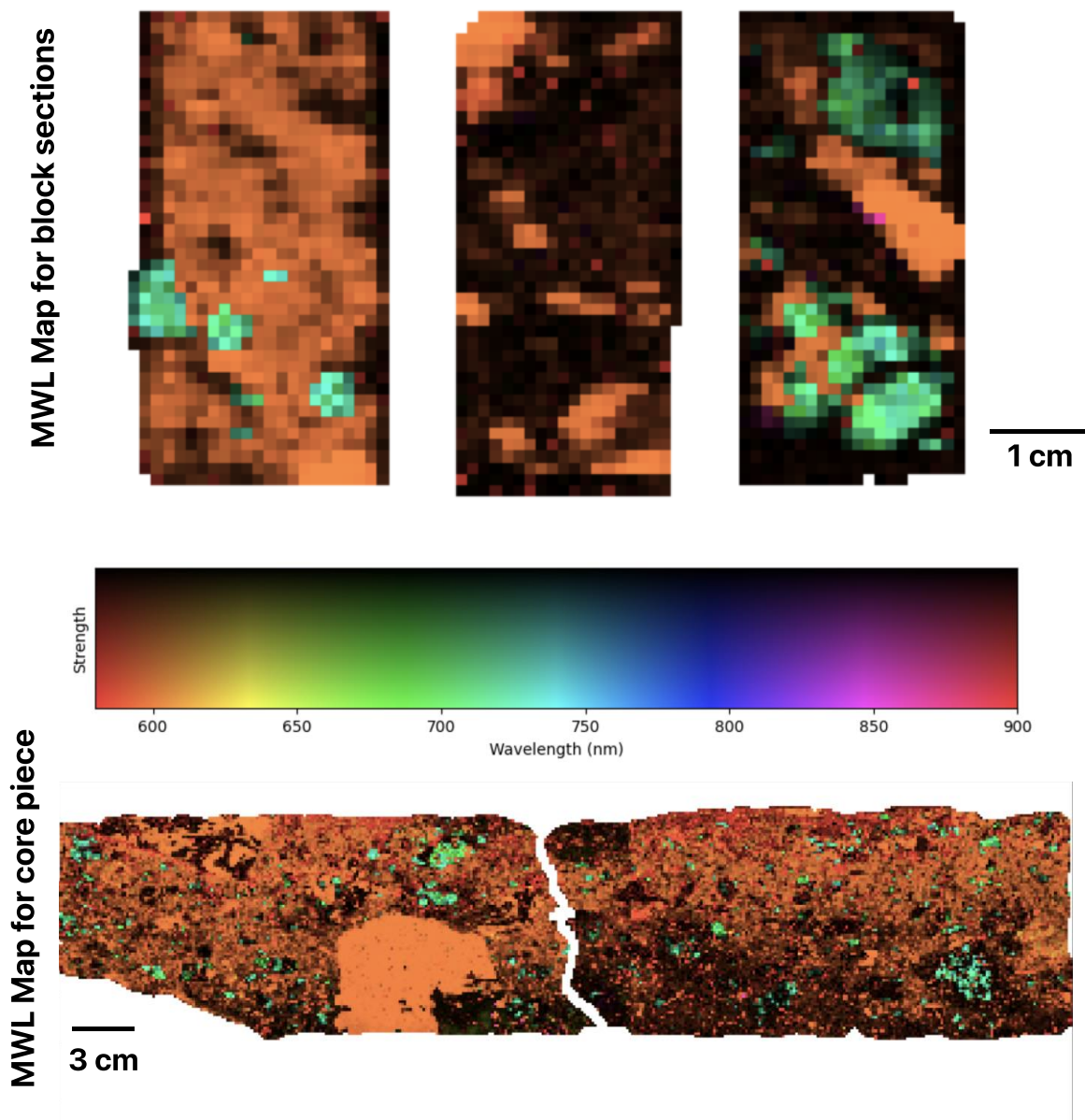


Figure 5.15: LiF data based minimum wavelength map across the broad 580 – 900 nm range for the block sections and the core pieces.

A total of nine points in three block sections were selected to represent a library of most of the spectral variations that exist within those samples as well as the core pieces. The pixel location along with the individual spectra of all these points is shown in Fig 5.16.

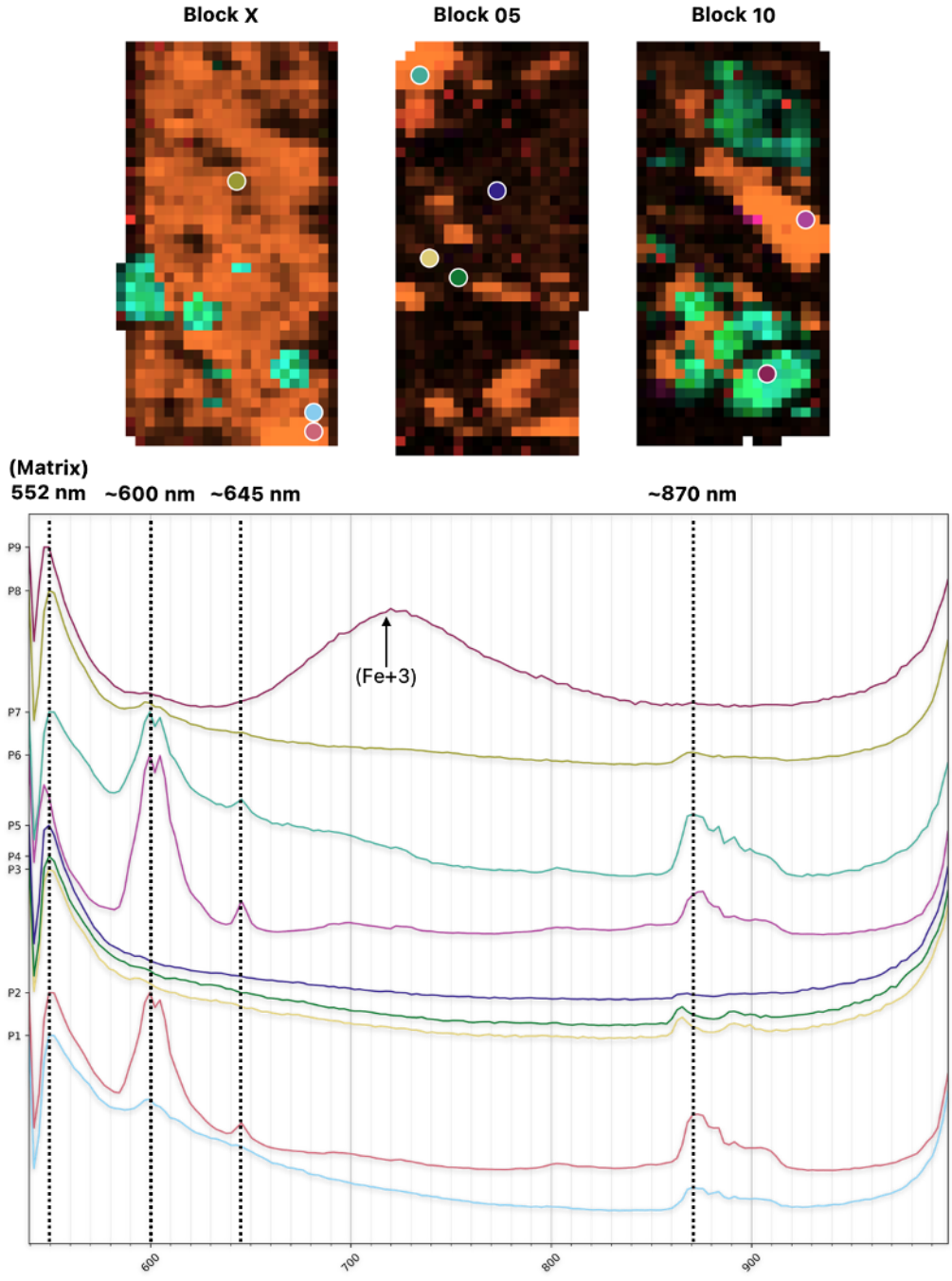


Figure 5.16: Individual emission spectra for all points identified in the block sections with certain peaks outlined.

Following this a point 'P6' which was found to contain all the main clearly visible features in one spectrum was chosen to be evaluated using a peak detection technique. The program highlighted the precise locations of all the features. The results of the peak detection for the point P6 are shown in Fig. 5.17 below.

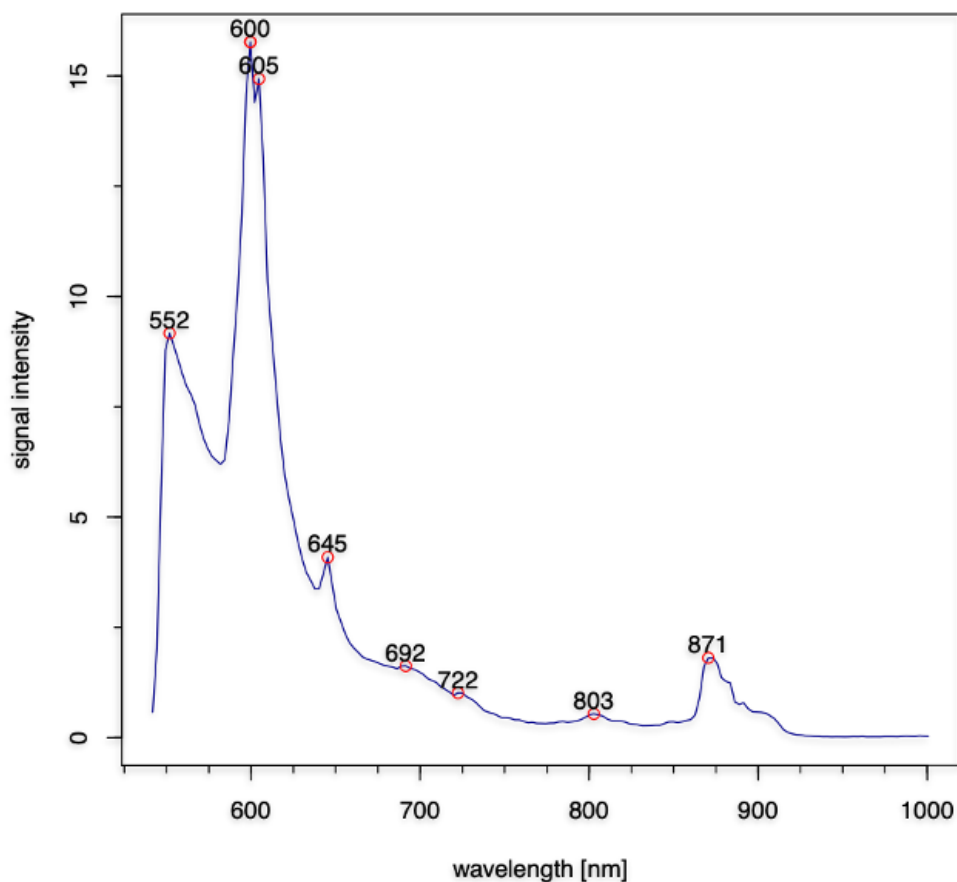


Figure 5.17: Result of peak detection technique used on the P6 identifying all the possible emission points existing in the spectra.

As illustrated in Fig 5.16, the 552 nm peak is observed in every sample point. This is interpreted as the emission peak related to the background class which does not indicate any real elemental signature. The 692 nm peak and 803 nm peak were considered to be too small to be correlated as major emission peaks of some specific rare earth element. These peaks are used as supplemental information in deciding which REEs can potentially exist.

The small 722 peak that is observed in spectra of P6 in Fig 5.16 is correlated to the broad emission feature that is seen in P9 in Fig 5.16. The regions with this peak are seen as cyan-colored discreet areas indicating a peak feature ~ 720 nm in LiF MWL map (in Fig 5.18). Based on past studies (Seidel et al., 2019; Cazenave et al., 2003), this peak can be assigned to the luminescence center of Fe^{3+} or other transition metal ions. Compared to HSI image, the same zones are also highlighted with a greenish-yellow color with features around ~ 650 nm. This feature in the HSI image can also be correlated to the presence of the Fe^{3+} ion (GMEX, 2008). Gaft et al. (2005), specifically highlighted that luminescence center for Fe^{3+} in feldspars particularly anorthoclase can be located at ~ 716 nm. This interpretation coincides well with the mineralogical information available for the

data where feldspar-plagioclase clusters are present in the same regions. Consequently, the 722 nm feature is not considered for further REE spectral conversation.

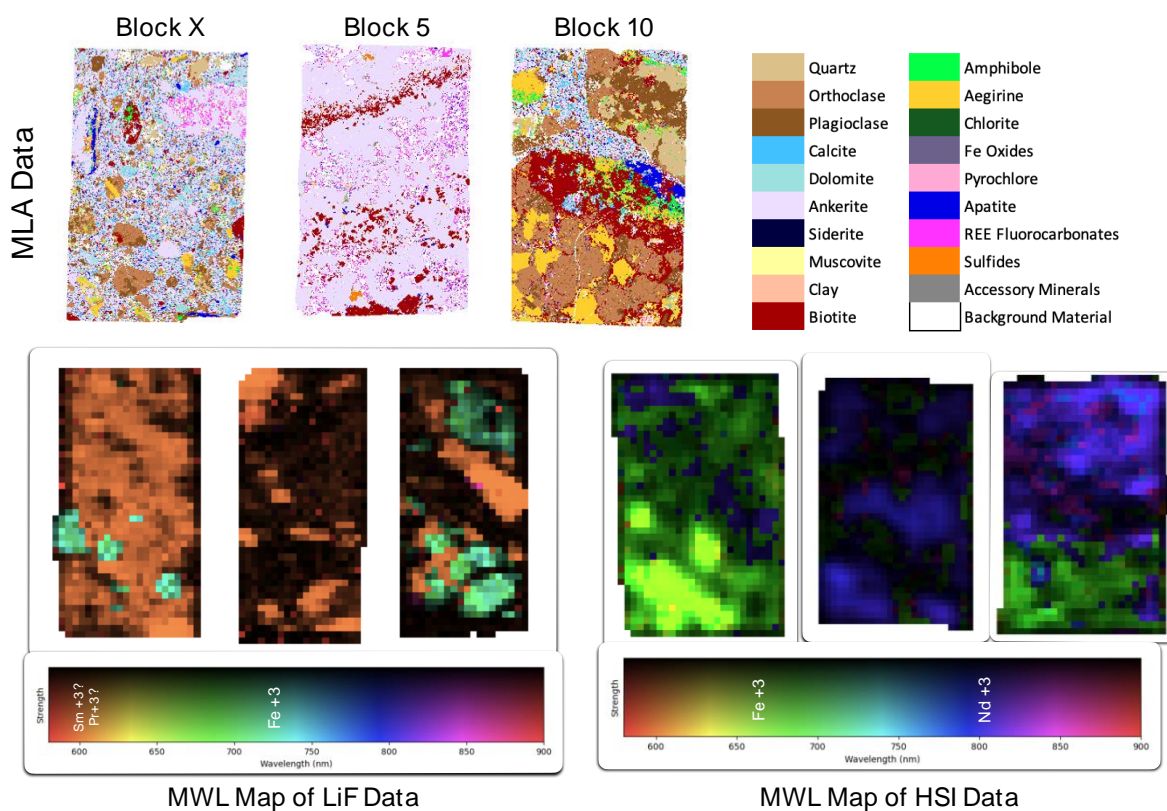


Figure 5.18: MWL comparison between maps generated for the blocks with LiF data (left) and hyperspectral data (right) for spectral range of 580-900nm along with the MLA mineralogical data of the respective blocks.

600 nm, 605 nm, 643 nm, and 871 nm were chosen as the main distinguishing spectral peaks. To understand the spatial distribution and correlation of the peaks, a set of false color images was created. In these images, the different R-G-B bands are assigned a specific channel. Essentially, these channels refer to specific deepest feature that is mapped using minimum wavelength mapping method within an encompassing specified spectral range. The 600 nm channel represents both the 600 and 605 nm peaks that coexist together and could not be spectrally separated out in the 590 – 615 nm range. The 645 nm channel represents the distribution of the 643 nm peak in 635 – 655 nm range, and the 870 nm channel illustrates the ~871 nm peak that exists within 860 – 900 nm range. Using this information, Fig 5.19 was created where the R+G band (yellow color) was assigned to one channel and B band (blue color) was assigned to another.

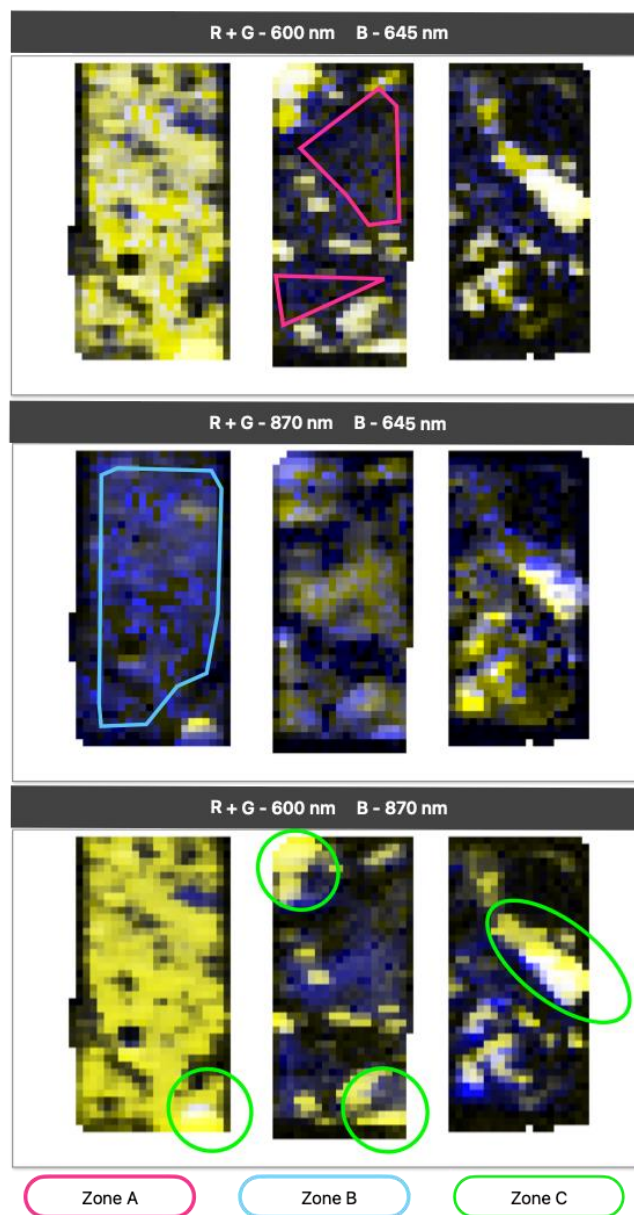


Figure 5.19: False color images indicating the co-distribution of the three emission peaks as well as the three identified zones. (Yellow – R+G; White – R+G+B)

5.10.2 Minimum Wavelength Mapping for LiF data

A minimum wavelength map created for the spectral range of 855 nm to 885 nm was used to map the 870 nm peak. The first minimum wavelength map is generated for the spectral range of 590 – 610 nm for both the core piece and block sections (Fig 5.20). It is observed that most of the features are primarily centered around ~597 nm (seen in green) across most of the region in the blocks and

core pieces. However, small specific regions with each map indicate a zone where peaks are generally observed ~ 600 nm (seen in cyan) and in some areas ~ 607 nm (seen in pink).

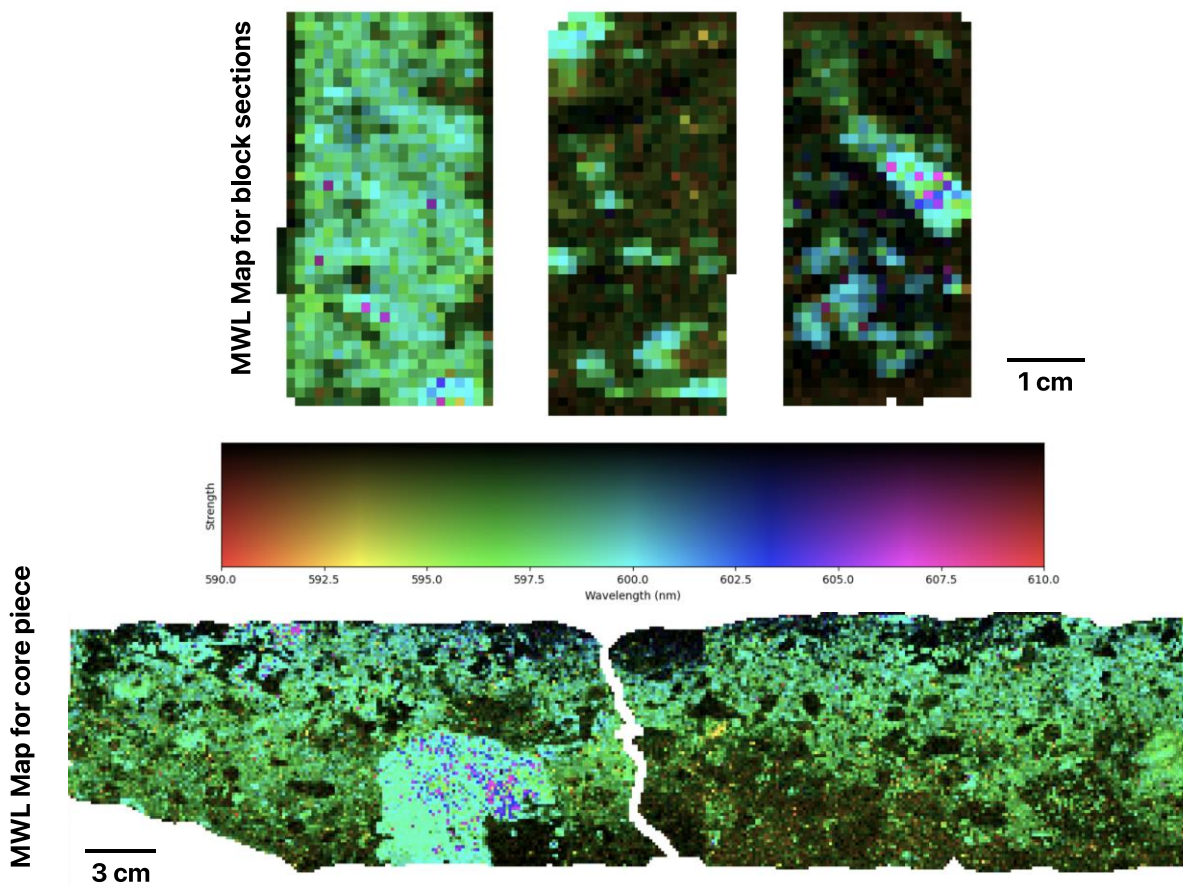


Figure 5.20: LiF minimum wavelength map identifying the peak between 590 – 610 nm range in the blocks and core pieces.

The other minimum wavelength map created for the spectral range of 855 nm to 885 nm was used to map the 870 nm peak. The resulting figure (Fig 5.21) across the blocks and the core piece shows two separate regions of interest. The first region (seen in green) exhibits a maximum peak within this spectral range at ~ 865 nm. The second region within these samples displays the peak emission spectra at ~ 872 nm.

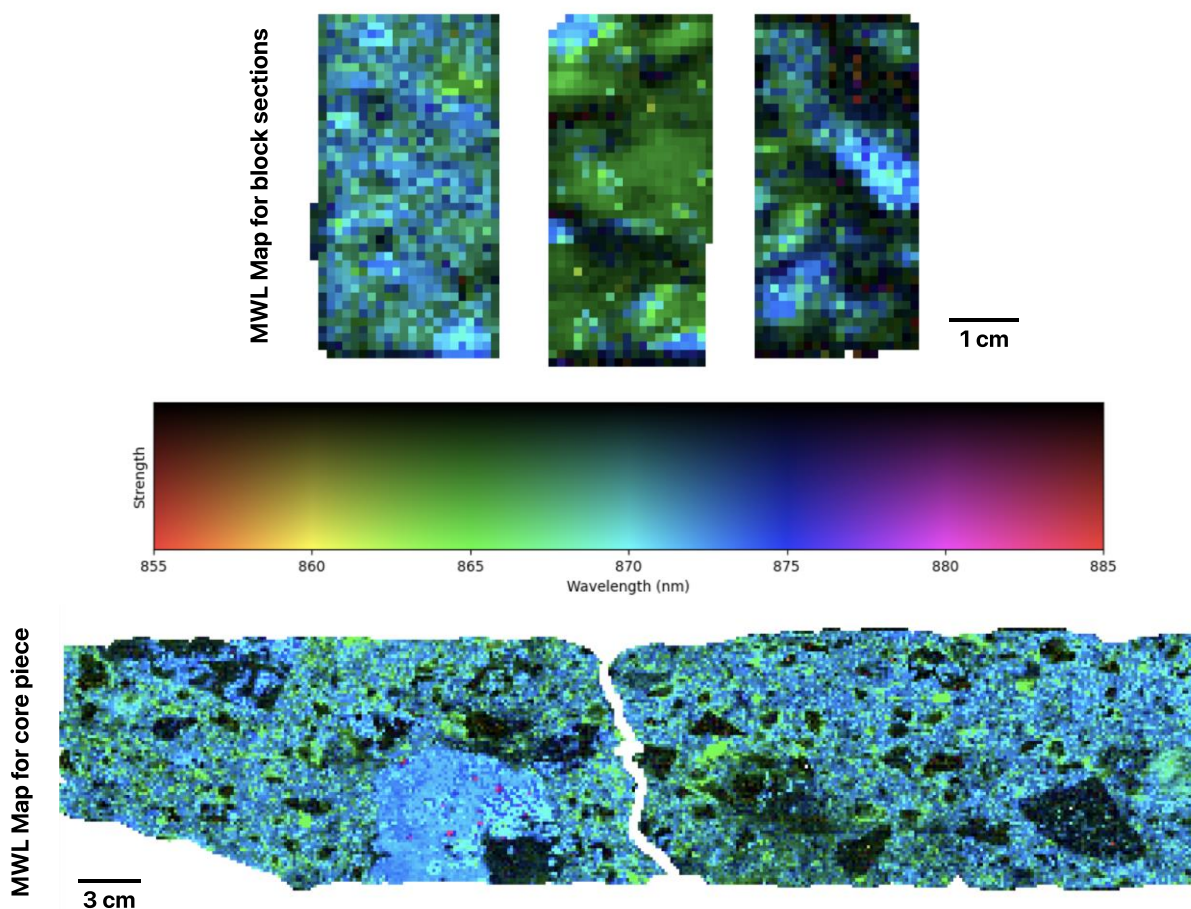


Figure 5.21: LiF minimum wavelength map identifying the peak between 855 – 885 nm range in the blocks and core pieces.

By comparing of the two minimum wavelength maps for the blocks with the false color images in Fig. 5.19, it is inferred that regions that exhibited similar behavior across the blocks and core pieces must belong to the same mineralogical zone. Regions that show ~865 nm (in Fig. 5.21) peak can be assigned as Zone A. Region that shows the ~597 nm peak (in Fig. 5.20) also displays a peak around ~870 nm (in Fig. 5.20) and can be assigned as Zone B. The other regions which show a peak at ~600 and ~607 nm (in Fig. 5.20) and ~872 nm (in Fig. 5.21) can be described as Zone C. These three zones defined in the blocks are correlated to the available mineralogical information. Zone A represents an ankerite carbonatite that is primarily contains in REE-fluorcarbonates with minor quantities of apatite whereas Zone B refers to the matrix of the intrusive breccia with significant quantities of apatite and REE-fluorcarbonates are dispersed. Zone C represents a regions with high accumulation of apatite.

Chapter 6 – Discussion

6.1 Discussion About the Storkwitz Carbonatite.

The results presented in this study demonstrate that most of the rock-forming and alteration minerals associated with the Storkwitz breccia can be mapped, at least qualitatively, using extended-range (VNIR-SWIR-MWIR-LWIR) for hyperspectral drill core scanning. This includes the recognition of different mineralogical variations that might not be evidently visible to the naked eye given the fine-grained texture of the Storkwitz breccia. The spectral lithologies identified through this workflow correlate well with the observations of texture and composition of the Storkwitz breccia by Loidolt et al. (2022). The first and second granitoid type clasts that are inferred to exist correspond to the coarse-grained granitoid clasts and the porphyritic granitoid clasts that are discussed by Loidolt et al. (2022). Loidolt et al. (2022) also identifies similar carbonatitic and other clasts within the matrix.

The effect of the alteration is prevalent and widely recognizable as demonstrated in the results and the subsequent interpretations. The major main alteration phases seen here are the fenitization, biotization and white mica-clay and ferric oxidation events. Due to the close inter relationship between the alkali amphibole, aegirine and biotite, it is not possible to accurately estimate the timing of biotization and fenitization events by solely using the mineral maps generated from the hyperspectral data. However, the complex intertwined association of fenitization minerals and biotite can indicate that fenitization and biotization at Storkwitz occurred in multiple stages and conforms with the multi-stage sequence events that Loidolt et al. (2022) suggest.

The white mica – clay alteration and the formation of ferric oxides within the drill core interval is correlated to some supergene alteration processes. These can be definitively linked to later stage events since they overprint a vast majority of the Storkwitz interval. As previously mentioned, the effect of the muscovitic and smectitic alteration of the granitoids and carbonatitic clasts is evidently extensive throughout the drill core. The evidence for ferric alteration is still seen in the drill core interval studied here although not as extensively widespread as in the upper zone of the breccia observed by Neigisch et al. (2020). Neigisch et al. (2020) attribute this extensive oxidation to supergene processes as the result of deeply percolating meteoric waters. Loidolt et al. (2022) argued that there is a decreasing influence of supergene processes with increasing depth and expected that the extent of supergene alteration within this interval would be minimal. However, the HSI results here indicate a more pervasive presence of the white-mica and clay within the samples and some lower quantities of ferric oxidation phases. This indicates that the effect of the supergene alteration processes is greater than previously considered which can be attributed to the percolating meteoric waters reaching deeper depths than originally thought. Due to the significantly high modal abundances of the white mica – clay class seen in the fault zone of the

drill core at the 435-437 m interval, it can be reasonably stated that the fault could have acted as a conduit for these meteoric waters and could explain the reason for the higher abundance of supergene altered products seen here. With the available results and subsequent interpretations here, only speculative conclusions about sequence and controlling factors of the alteration assemblages can be made.

An important point to consider here is that while the effect of ferric oxidation can be a part of the evolution of the Storkwitz drill core, these drill cores were extracted ten years ago and could have also undergone recent oxidation of the iron phases unrelated to the oxide amounts associated with the assemblages of the lithologies. This could lead to the appearance of widespread occurrence of the secondary ferric iron oxides within samples due to the increased Fe^{3+} signal

In the context of the LiF data, Lorenz et al. (2018) demonstrated that the ~870 nm peak feature that is observed in their samples belongs to Nd^{3+} and its position can shift depending on the host material. Within this context and other studies (Fuchs et al., 2021; Gaft et al., 2005), the 870 nm feature here is indicative of the presence of neodymium within the samples. As the 870 nm MWL map outlines (Fig 5.22, Fig. 5.23), two spectral regions exist with the emission peak at ~865 nm and ~872 nm. Based on the findings from Lorenz et al. (2018), these must correlate to difference in host material. The study suggested that the primary peak for bastnäsite is ~865 nm and for REE bearing phosphate is ~870 nm and that depending on the host mineral, a certain peak shape is also observed. The findings of the Lorenz et al. (2018) study about the peak shape and position can accurately be correlated to mineralogical information of the blocks (as seen in Fig 5.22). The regions with high REE-fluorcarbonate content i.e Zone A is shown with a peak position around ~865 nm whereas regions that contain apatite (Zone B and Zone C) have a peak around ~872 nm.

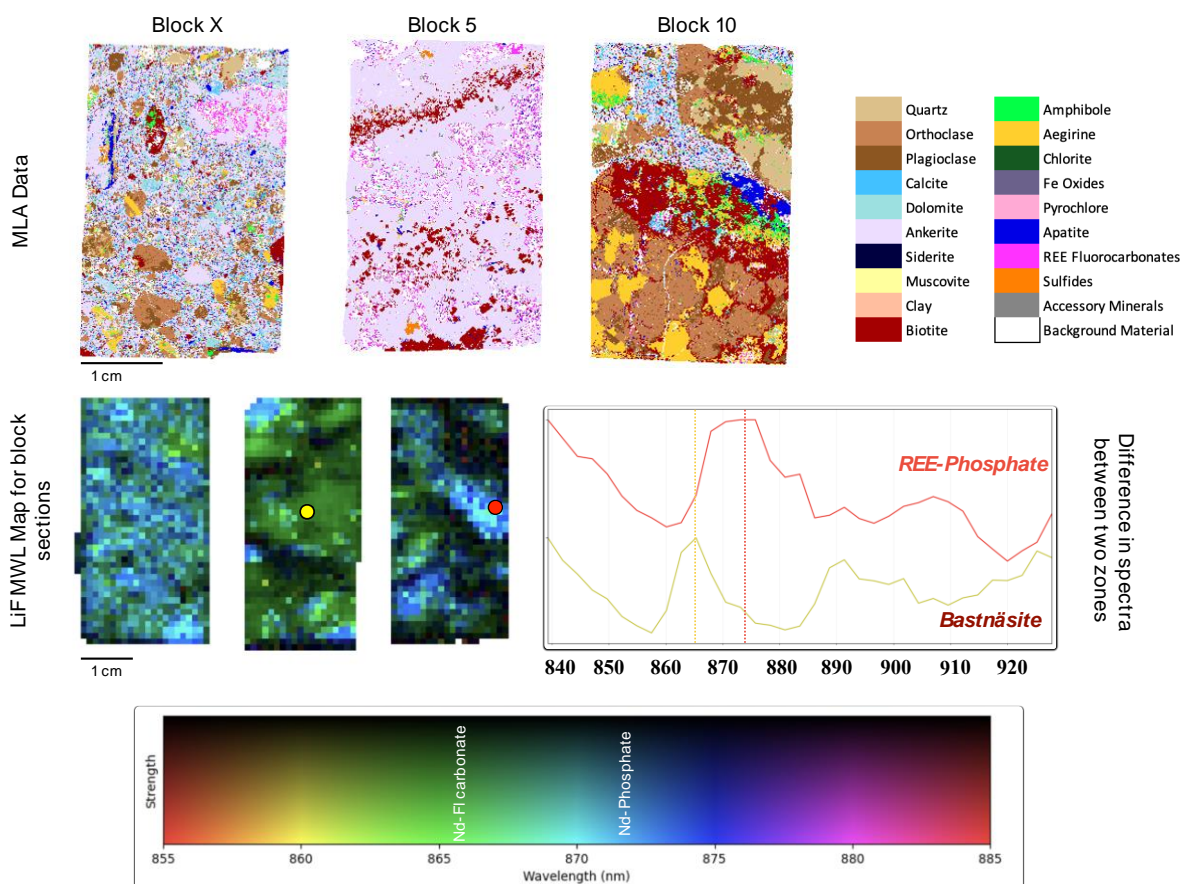


Figure 6.1: LiF 870 nm MWL map for blocks along with spectra from two different peak regions along with the MLA data to illustrate the REE-fluorcarbonate and apatite rich areas.

On examination of the core pieces in the 870 MWL map (see Fig 6.1), it is reasonable to infer the same mineralogy must exist in the core pieces if spectral behavior is similar to the blocks as observed. Following this assumption, the majority of the matrix of core pieces shows similar behavior as with Zone B in the blocks and are inferred as the groundmass of the core piece (breccia matrix) which contains dispersed amounts of REE-fluorcarbonates and apatite. The two clast zones that exist in the core piece can be correlated to Zone C since they display all the identified peaks (Fig 6.1, Fig 6.2). This leads to the interpretation that the two clasts are apatite rich. The FX50-SAM and OWL-SAM maps classify these regions as a carbonate clasts and by evaluating the Carbonate MWL map, these clasts can be identified dolomite carbonatite clasts (as seen in Fig 6.2). Subsequently, this finding implies that the dolomite carbonatite clasts seen here have high concentrated abundance of apatite which is associated with REEs.

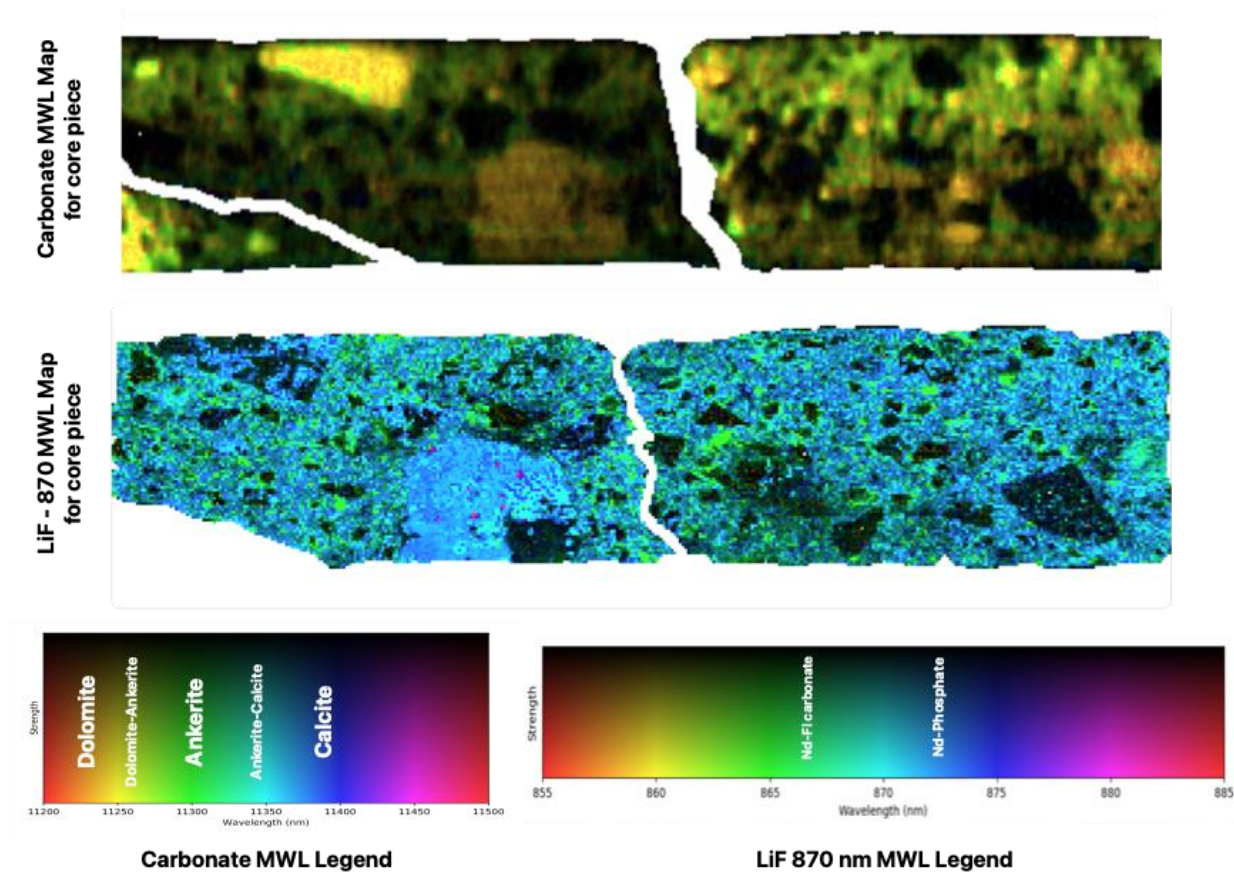


Figure 6.2: LiF 870 nm MWL map of core pieces with the correlating Carbonate MWL map illustrating the dolomitic composition of the two carbonatitic clasts.

In terms of the 600 nm MWL map (Fig 5.20), the intrusive breccia matrix containing apatite and REE-fluorcarbonates in the blocks and the core piece exhibits the peak around ~597 nm. However, since no peak features are observed in Zone A i.e region containing high concentration of REE-fluorcarbonates. This peak is attributed primarily to the apatite present in the intrusive breccia matrix. In case of the apatite-rich regions in the blocks and the clasts in the core piece, a peak is generally observed ~600 nm along with areas that exhibit a peak at ~606 nm. These features could potentially be attributed to Sm^{3+} and Pr^{3+} based on their typical behavior (Fuchs et al., 2021; Gaft et al., 2005).

Based on the LiF MWL results and interpretations, the primary REE bearing mineral assemblage in the Storkwitz breccia is apatite hosted in dolomite carbonatitic clasts followed by the REE fluorcarbonates predominantly bastnäsite in the ankerite carbonatite clasts and lastly the apatite and REE-fluorcarbonates present in the breccia matrix. However, a key point to note in this finding is that apatite grouping that is depicted in the MLA images also considers very minor amounts (~0.05% avg. vol) of monazite that were detected in the block sections. When discussing the REE bearing phosphates particularly within the core piece, the REEs could be hosted within the monazite phase or the apatite phase.

As seen from the HSI generated maps, the REE-fluorcarbonates are associated with the different carbonatitic clasts especially ankerite carbonatites and with aegirine and amphiboles. The REE fluorcarbonates are also dispersed within the breccia given the widespread cover of the carbonate-clay-REE-fluorcarbonate class across the FENIX abundance map. Based on the LiF results, REE bearing REE-fluorcarbonate particularly bastnäsite exists in in ankerite-carbonatite clasts and is widely dispersed in the groundmass of the breccia. Specifically, within the breccia matrix, the REE-fluorcarbonate is seen forming rims around other clasts.

Since no characteristic spectral features corresponding to apatite were identified in any of the endmembers across the three wavelength range datasets, a class containing apatite was not present in resulting maps. However, based on the previous study by Loidolt et al. (2022), some general constraints for the occurrences of these REE bearing phosphates can be applied. Loidolt et al. (2022) stated that apatite is abundant in dolomite carbonatites and the breccia matrix while monazite can be found in ankerite carbonatites. Müller et al. (2021) and Niegisch et al. (2020) observed REE-fluorcarbonates and monazite forming thin rims around clasts within the matrix. Therefore, the primary REE bearing phosphates within the dolomite-ankerite clasts is likely apatite but within the matrix of intrusive breccia, the REE bearing phase could be apatite or monazite but likely the latter. The minor quantities of REE phosphate that are found with the REE-fluorcarbonates in the ankerite carbonatite could possibly be monazite.

The findings from this project contradict the inferences from previous research by Loidolt et al. (2022) which studied a similar interval length and stated that the majority of the REEs are mainly hosted in a REE-fluorcarbonate mineral assemblage within the fine-grained ankerite-carbonatites with only minor quantities incorporated into primary magmatic phases like apatite and in REE-fluorcarbonates in the matrix. Alternatively, Niegisch et al. (2020) that examined the upper zone of the Storkwitz breccia classified all REE-containing phosphates as monazite with lesser but significant REE-fluorcarbonate mineralization. Based on the MLA data of the blocks studied by Loidolt et al. (2022), their study observed that REE-fluorcarbonates only exist in matrix in rare occurrences. However, the results from my LiF measurements indicate that the REE-fluorcarbonates and REE-bearing phosphates are abundant across the breccia matrix.

Within the Storkwitz breccia, the REE bearing apatite could be representative of the early mineral crystallizing out of the carbonatitic magma. According to Chakhmouradian et al. (2017), during the initial stages of crystallization, apatite can undergo early fractionation which can remove substantial amounts of REEs from the carbonatite melt. The composition of apatite is fundamentally determined by the presence of other rock-forming minerals, such as phlogopite, amphiboles, calcite, and dolomite, which have a limited ability to incorporate REE. While Niegisch et al. (2020) considered apatite as accessory minerals with very minor quantities of REEs and Müller et al. (2021) detected only low quantities of REE concentrations in apatite, Seifert et al. (2000) observed a greater variation in REE concentrations in apatite. It can be presumed that

the REE bearing apatite in the dolomite carbonatite clasts here have potentially formed during the earlier magmatic stages of evolution of the deposit.

In the context of the REE bearing phosphates in the matrix, Loidolt et al. (2022) discussed that the presence of these minerals in the matrix is correlated to minor syn- and / or post brecciation REE transport. This resulted in the local redistribution of REEs and is most likely to be the result of a hydrothermal fluid. This is also supplemented by Niegisch et al. (2020) who suggest that late-stage hydrothermal or supergene processes caused the recrystallization of primary REE minerals to secondary monazite and REE-fluorcarbonates in the matrix. Given that significant quantities of REE bearing minerals are found to exist around clasts within the matrix, the conclusion that the effect of supergene alteration goes deeper than previously thought can be further validated if the redistribution of REEs is confirmed to be associated with supergene processes as stated by Niegisch et al. (2020). This can also be true especially considering that the core pieces analyzed with the LiF set up are found at ~486.3 m, towards the end of the studied interval.

Ultimately, the exact identification and differentiation between the REE-bearing phosphates i.e apatite and monazite across the samples in the context of the available information is not possible within this discussion. Additionally, further detailed discussion about definitively correlating these new insights about REE-bearing phosphates and REE-fluorcarbonates to the broad geological evolution of Storkwitz breccia and the possible REE-enrichment processes that could have occurred is beyond the capabilities of the equipment and therefore outside the scope of this project.

In terms of the identification of specific REEs, given the peaks identified along with the excitation wavelength used, only speculative discussion about the existence of certain REEs can be made. The 870 nm can be definitively related to presence of Nd^{3+} as also confirmed by the hyperspectral data. This indicates that the apatite and REE-fluorcarbonates both host Nd^{3+} . Fuchs et al. (2021) and Gaft et al. (2005) indicate that Sm^{3+} can have peak features around ~598 nm and ~643 nm with blue-green excitation wavelengths. They also suggest that Pr^{3+} can have feature around ~600 nm and ~650 nm. Since 600 nm, 645 nm and 870 nm are identified as the primary REE emission peaks, Sm^{3+} , Pr^{3+} , Nd^{3+} are the main suspects exhibiting these peaks. It can also be argued that Eu^{3+} could also be present since it typically shows a feature ~601 nm. However, a prominent feature ~700 nm must also be evident. The minor peak observed at ~692 nm could be representative of this element, but insufficient information makes this conclusion highly speculative. In the end, it can be discussed that the REE-fluorcarbonate likely hosts Nd^{3+} and the apatite or generally the REE bearing phosphate is likely to contain Sm^{3+} , Pr^{3+} and/or Eu^{3+} . Although the existence of certain REEs could not definitively be suggested, the peaks were primarily correlated to elements that are grouped as light rare earth elements (LREE).

Additionally, no distinct peaks for any heavy rare earth elements (HREE) were observed, even Dy^{3+} which can typically have prominent features even in low concentrations similar to Nd^{3+}

(Seidel et al., 2019; Lorenz et al., 2018). This finding is also validated by the research by Niegisch et al. (2020) that suggesting that the Storkwitz carbonatites are chiefly LREE enriched instead of HREE enriched.

6.2 Features and Limitations of Proposed Workflow

The proposed workflow integrates the whole VNIR-SWIR-MWIR-LWIR range for analyses, by dividing the range into three datasets. As demonstrated through the validation of the results the maps, generated with the different techniques on these datasets using the endmembers extracted from the blocks, produced mixed results.

The product of the linear unmixing algorithm in the VNIR-SWIR range produced accurate individual abundance maps where the concentrations of the matrix endmember associated the low intensity background spectra was low. This implies that the endmember library used for the spectral unmixing for this dataset was adequately representative of the all the spectral variation within that dataset. Consequently, as a result of the low matrix class abundance, the final maximum classification map generated accurately depicted the distribution of the mineralogies associated with the visible and short-wave minerals based on the validation that was conducted. The FENIX classification map provides the most information about the distribution of the identified endmembers amongst the three maps since the matrix or background class is only present in small quantities. In contrast, the spectral unmixing results for the MWIR and LWIR datasets revealed sub optimal results. While the individual abundance maps for these endmembers revealed a good distribution of the actual mineral endmember classes, in both cases, the matrix endmember was the most predominantly abundant class. When creating the maximum classification map, this background class that is present in large quantities hides features that would otherwise be seen. Mineral associations between the endmembers can still be interpreted from the individual abundance maps but the maximum classification map for these revealed little information about existing mineralogical distribution and therefore do not provide any valuable information needed for the spectral characterization of the lithologies. Ultimately, OWL and FX50 classification map were excluded from any further evaluation.

While the exact reason for the dominant abundance of the matrix class is not known, a possible explanation can be that the selected endmembers were not representative of all the materials in those data ranges. Since spectral unmixing aims to find the best linear combination of endmembers to approximate the observed spectrum, the resulting pixels are computed to largely be composed of the low intensity background matrix values making that class the most abundant as a result. Although an intensive endmember selection process was undertaken, the endmembers could potentially not be representative of the data.

When assessing the results of the spectral angle mapping technique, an opposite trend is noticed. As demonstrated by the validation studies, the FENIX-SAM which was generated using the visible-shortwave endmembers misrepresents the actual distribution of the minerals within the sample. This is contrasted by the more accurate results that are generated from applying the endmembers to the other two datasets (FX50-SAM; OWL-SAM). A possible explanation for the poor spectral angle mapping result for the VNIR-SWIR dataset could be due to the higher noise within the dataset. Although the block data was smoothed before endmember extraction, no smoothing filter was applied to the whole drill core data. Spectral angle mapping as a technique is sensitive to noise in the data. If the shortwave data has a high level of noise or lower data quality compared to the other datasets, it can negatively impact the spectral angle mapping results, even if the endmembers are representative. On the other hand, spectral unmixing might be less affected by noise, leading to relatively better results. Conversely in the case for the MWIR and LWIR datasets, despite getting sub optimal results using the spectral unmixing technique, the respective maps generated with this method could be validated accurately. In the case of spectral unmixing despite these datasets not being considered as representative, since spectral angle mapping utilizes a different method where the angular difference between spectra is measured, the method leads to more robust results. These results could also be attributed to the fact that spectral angle mapping and spectral unmixing have different sensitivities to spectral similarity. The MWIR and LWIR datasets can contain minerals with similar or overlapping diagnostic features in the specific wavelength ranges. This is especially true for MWIR as discussed by Laukamp et al. (2021). In this case spectral unmixing might struggle to accurately estimate their abundances, whereas spectral angle mapping based on a different method can still provide reasonable results.

Despite some discrepancies in the mapping of the data, the results overall indicated that the application of the entire hyperspectral range (VNIR-SWIR-MWIR-LWIR) is beneficial for the spectral characterization process. Although the MWIR range containing spectral features for a wide variety of minerals like carbonates, amphiboles, micas, and quartz (Laukamp et al. 2021), it is still considered to be poorly understood in terms of its application for geological mapping. The results in this study not only suggest that the MWIR is suitable for mapping the carbonates and mica features for the Storkwitz carbonatite, but it is also found to be valuable for cross-validating absorption features observed in the SWIR and LWIR ranges. This results in a greater confidence in the suggested spectral interpretations and also helps to untangle the complex mixtures that can occur in the SWIR region. Within this geological environment, the 2300-2360 nm range in the SWIR was found to be too complex for accurate feature extraction due to the presence of features for carbonates, amphiboles, and biotite within this range. In this scenario, utilization of the MWIR and LWIR wavelength ranges was evidenced to be extremely beneficial.

The utilization of combined HSI-LIF approach followed here highlights the higher sensitivity of LIF data in providing clear distinct signals within the dataset in comparison to the HSI results. In HSI map features mainly related to Nd^{3+} dominate the spectra, whereas other REE ions exhibit no

substantial signal. This is clearly observed in the Fig 5.18 where only the prominent Nd features within the samples are observed. In contrast, the brightest feature observed ~600 nm could be correlated to the presence of Sm^{3+} or Pr^{3+} . No sharp absorption features are visible in the ~600 nm range in the hyperspectral map implying that the concentration of these elements must be below the detection limit of the sensor. Despite Nd^{3+} existing in the sample, the feature for Nd^{3+} in LiF data is hidden by the brighter Sm^{3+} or Pr^{3+} peak. In both the images the general local structures similar to the LIF map however, the individual REE signals are more pronounced in the latter image.

Chapter 7 – Future Outlook

This study is the first of this kind where REE bearing minerals in drill core have been mapped by the combined application of hyperspectral imaging across the extended wavelength range and an integrated line scan set up for laser induced fluorescence measurement set up for drill core samples. While this proposed workflow does require certain previous knowledge of the lithology and the type of mineralization and alteration present, it can aid geologists in making faster decisions for further structural, geochemical, and petrological investigations. This novel approach is meant to supplement geochemical studies by providing a quick qualitative discrimination of geological domains and a better identification and understanding of the REE-hosting minerals. Thus, this integrated approach of lithology and REE mineralization mapping using HSI and LiF has significant potential in its application in the exploration industry. This is due to its key advantage in providing a greater sensitivity to REE detection which also results in the fingerprinting of host minerals associated with certain REEs particularly Nd. This thereby provides additional information for performing geological logging and further geological interpretation. Additionally, LiF interpretation can also be extrapolated onto the drill core interval without the need for scanning extensive lengths of core with LiF set up.

A key distinct feature of the proposed workflow in this study includes the utilization of the MLA blocks for endmember extraction leading to the effective and quick creation of a reference endmember library used in further unmixing and mapping techniques. Typically, a sampling scheme is needed for drill cores where small samples are extracted for detailed analysis using e.g., transmitted light microscopy, MLA or XRD. Generally, performing endmember extraction using the hyperspectral data for the entire drill core interval can be time consuming and processing power intensive especially if long intervals of drill cores are to be evaluated. This issue is mitigated by the use of blocks can be effectively processed to produce representative endmembers. This thereby maximizing the amount of information that can be obtained from a small subset of the materials. Moreover, having the mineralogical information also provides the necessary validation for the identification of the extracted endmembers. It is important to consider that mixed quality results can be produced when using the extracted endmembers for mapping as seen here. However, with the use of different mapping techniques and performing visual validation of the rocks, accurate maps can still be produced which can be used for subsequent geological interpretations.

Through combined LiF approach, the REE rich zones that are identified through the hyperspectral data analysis can be initially analyzed to evaluate the behavior REEs. For the future implementation the results of initial set of laser induced fluorescence measurements can also guide the next stage of further LiF experiments. For instance: within the Storkwitz breccia, the main REE-bearing phosphates were found to be hosted primarily in dolomite carbonatites. This can lead to the next set of potential measurements to be focused on these clasts to better understand the

associated behavior of the hosted REEs. It is also important to note that all of the mineral maps produced are qualitative surface estimates and do not serve to provide any quantitative information about the REEs or associated mineralogies.

7.1 Recommendations

Some suggestions for the future prospects of studies in relation to hyperspectral imaging and laser induced fluorescence spectroscopy as well as the Storkwitz mineralization overall include:

1. In the future, for better endmember extraction, a different strategy for the endmember extraction where one endmember can be extracted from each meter of core and then manually checked for quality and added to the spectral library ensuring that pure good quality endmembers are used for further studies
2. Instead of using three datasets that would be complementary information for the same region, potentially identify endmembers that have the best features by combining the PCA wavelengths and choosing points that are unique across all wavelengths for better endmember extraction.
3. Developing a machine learning workflow that co-registers the hyperspectral data with smaller regions where laser induced measurements were taken to extrapolate that information to the entire drill core length allowing for qualitative representation of the behavior of the REEs across the drill core without the need for extensive scanning using the LiF setup. This can also be applied in cases where a region is scanned using preprogrammed raster that takes point measurements across a small region.
4. Implementing a more efficient workflow for the acquisition of LiF data using the integrated line scan set up to allow for scanning of the entire drill core length.
5. Conducting electron probe micro-analyzer (EPMA) analysis of the apatite and REE-fluorocarbonates to determine trace element and exact REE concentrations through which a more reliable and robust REE mineralization sequence can be suggested.

Chapter 8 – Conclusions

In conclusion, the proposed workflow integrating the entire VNIR-SWIR-MWIR-LWIR range for hyperspectral analyses has provided valuable insights into the spectral characterization and REE mineralization of the Storkwitz breccia. The results demonstrate both successes and challenges in utilizing different techniques for mineral characterization and mapping. Despite discrepancies, the application of the entire VNIR-SWIR-MWIR-LWIR range proved beneficial for spectral characterization, especially in mapping carbonates and mica features in the MWIR range, which otherwise remain poorly understood in geological mapping. The study also emphasized the higher sensitivity of LIF data in providing distinct signals within the dataset compared to HSI, allowing for better identification of light rare earth elements (LREE).

In terms of the Storkwitz breccia, the spectral interpretations using the combined HSI-LIF approach correlated well with previous observations of rock-forming minerals and alteration phases. The presence of fensitization, biotization, white mica-clay, and ferric oxidation events suggested multiple stages of fensitization and biotitization. The extensive presence of white mica-clay and ferric oxides in the drill core interval indicated a greater influence of supergene processes than previously considered, possibly due to deeper percolating meteoric waters potentially via fault conduits.

Regarding REE mineralization, the primary REE-bearing mineral assemblage in the Storkwitz breccia is apatite hosted in dolomite carbonatitic clasts, followed by REE-fluorcarbonates in ankerite carbonatitic clasts and in the breccia matrix. Contrary to previous studies, apatite, rather than REE-fluorcarbonates, is suggested to be the primary host of REEs. The apatite can potentially be formed as a result of early fractionation from the carbonatitic magma and the presence of REE-bearing minerals in the matrix may be attributed to deeper supergene processes.

The utilization of hyperspectral imaging and laser-induced fluorescence spectroscopy in the characterization of lithologies and rare earth element mineralization within the Storkwitz breccia has demonstrated its potential for applications in the exploration industry. This two-stage workflow proposed in this study was able to spectrally characterize the lithologies in the Storkwitz while identifying the key REE-bearing minerals. However, further research is required to definitively identify the REE-bearing phosphates and to understand the broader geological evolution and REE-enrichment processes in the Storkwitz deposit.

Appendix

A digital appendix is created for this project to best preserve the resolution of all the generated maps. The appendix can be accessed here:

<https://www.dropbox.com/sh/n5t51xcxdq6fj3g/AADhORtcAjD8XnCFVq4RaK1xa?dl=0>

The appendix provided here is divided into two primary sections.

- Appendix 1 - contains all the hyperspectral data acquired from the blocks.
 - Appendix 1.1 - Folder containing maps generated by the MLA software for all the blocks after the mineral reclassification was done. The folder also contains the color legends for all the mineral groups present in the MLA maps.
 - Appendix 1.2 - Folder containing the Fe-Oxide band ratio result for the blocks.
 - Appendix 1.3 - Folder containing the all the minimum wavelength map results for the blocks.
- Appendix 2 - contains all the maps created using hyperspectral data acquired from the entire drill core.
 - Appendix 2.1 - Three Mosaic files for the three wavelength datasets which contain all of the individual abundance maps for the respective endmembers along with the maximum classification map for that dataset.
 - Appendix 2.2 - Three files of the maximum classification map for that dataset. The folder also contains the respective legends identifying the endmember classes for each map.
 - Appendix 2.3 - Three files of the resulting maps from the spectral angle mapping (SAM) that was done for each dataset. The folder also contains the respective legends identifying the endmember classes for each map.
 - Appendix 2.4 - The Fe-Oxide band ratio map that is the combined result of the Fe^{3+} , Fe^{2+} , and Fe-OH band ratios.
 - Appendix 2.5 - Folder containing the resulting HSI minimum wavelength maps for REE (Nd) feature, ALOH feature, LWIR Carbonate feature and Quartz-Plag-Aegirine difference. The folder also contains the respective legends for each image.

References

- Abend, T., Sharma, S. K., Fuchs, M., Beyer, J., Heitmann, J., & Gloaguen, R. (2019). Line-scan detection system to identify rare earth elements in rocks. *2019 IEEE SENSORS*, 1–3. <https://doi.org/10.1109/SENSORS43011.2019.8956697>
- Acosta, I. C. C., Khodadadzadeh, M., Tolosana-Delgado, R., & Gloaguen, R. (2020). Drill-Core Hyperspectral and Geochemical Data Integration in a Superpixel-Based Machine Learning Framework. *IEEE J. Sel. Top. Appl. Earth Obs. Remote Sens.*, *13*, 4214–4228. <https://doi.org/10.1109/JSTARS.2020.3017242>
- Acosta, I. C. C., Khodadadzadeh, M., Tusa, L., Ghamisi, P., & Gloaguen, R. (2019). A Machine Learning Framework for Drill-Core Mineral Mapping Using Hyperspectral and High-Resolution Mineralogical Data Fusion. *IEEE J. Sel. Top. Appl. Earth Obs. Remote Sens.*, *12*, 4829–4842. <https://doi.org/10.1109/JSTARS.2019.2934366>
- Aliabadi, F. M. H., & Soboyejo, W. (Wole). (2023). *Comprehensive structural integrity* (Second edition.). Elsevier Science & Technology.
- Bankwitz, P., Schneider, G., Kämpf, H., & Bankwitz, E. (2003). Structural characteristics of epicentral areas in central Europe: Study case Cheb Basin (Czech Republic). *Journal of Geodynamics*, *35*, 5–32.
- Barker, S. D., Barker, S. L. L., Wilson, S. A., & Stock, E. D. (2020). Quantitative Mineral Mapping of Drill Core Surfaces II: Long-Wave Infrared Mineral Characterization Using mXRF and Machine Learning. *Econ. Geol.*, *116*, 821–836. <https://doi.org/10.5382/econgeo.4693>
- Bhatt, C. R., Jain, J. C., Goueguel, C. L., McIntyre, D. L., & Singh, J. P. (2018). Determination of Rare Earth Elements in Geological Samples Using Laser-Induced Breakdown Spectroscopy (LIBS). *Applied Spectroscopy*, *72*(1), 114–121. <https://doi.org/10.1177/0003702817734854>
- Boesche, N., Rogass, C., Lubitz, C., Brell, M., Herrmann, S., Mielke, C., Tonn, S., Appelt, O., Altenberger, U., & Kaufmann, H. (2015). Hyperspectral REE (Rare Earth Element) Mapping of Outcrops—Applications for Neodymium Detection. *Remote Sensing*, *7*(5), 5160–5186. <https://doi.org/10.3390/rs70505160>
- Booyesen, R., Jackisch, R., Lorenz, S., Zimmermann, R., Kirsch, M., Nex, P. A. M., & Gloaguen, R. (2020). Detection of REEs with lightweight UAV-based hyperspectral imaging. *Scientific Reports*, *10*(1), 17450. <https://doi.org/10.1038/s41598-020-74422-0>
- Booyesen, R., Lorenz, S., Thiele, S. T., Fuchsloch, W. C., Marais, T., Nex, P. A. M., & Gloaguen, R. (2022). Accurate hyperspectral imaging of mineralised outcrops: An example from lithium-bearing pegmatites at Uis, Namibia. *Remote Sensing of Environment*, *269*, 112790. <https://doi.org/10.1016/j.rse.2021.112790>

- Booyesen, Zimmermann, Lorenz, Gloaguen, Nex, Andreani, & Möckel. (2019). Towards Multiscale and Multisource Remote Sensing Mineral Exploration Using RPAS: A Case study in the Lofdal Carbonatite-Hosted REE Deposit, Namibia. *Remote Sensing*, 11(21), 2500. <https://doi.org/10.3390/rs11212500>
- Bozlee, B. J., Misra, A. K., Sharma, S. K., & Ingram, M. (2005). Remote Raman and fluorescence studies of mineral samples. *Spectrochim. Acta A*, 61, 2342–2348.
- Broicher, H. F. (1999). Ore and waste identification and quality control by means of laser induced fluorescence. *CIM Bull.*, 92(1034), 59–63.
- Buckley, S. J., Kurz, T. H., Howell, J. A., & Schneider, D. (2013). Terrestrial lidar and hyperspectral data fusion products for geological outcrop analysis. *Computers & Geosciences*, 54, 249–258.
- Calvin, W. M., & Pace, E. L. (2016). Mapping alteration in geothermal drill core using a field portable spectroradiometer. *Geothermics*, 61, 12–23.
- Cazenave, S., Chapoulie, R., & Villeneuve, G. (2003). Cathodoluminescence of synthetic and natural calcite: The effects of manganese and iron on orange emission. *Mineralogy and Petrology*, 78(3–4), 243–253. <https://doi.org/10.1007/s00710-002-0227-y>
- Ceritech. (2012). *Daten-CD der Bohrung SES-1/2012 mit Anlagen 4 bis 13 zum Abschlussbericht Erlaubnisfeld "Delitzsch."*
- Chakhmouradian, A. R., Reguir, E. P., Zaitsev, A. N., Couëslan, C., Xu, C., Kynický, J., Mumin, A. H., & Yang, P. (2017). Apatite in carbonatitic rocks: Compositional variation, zoning, element partitioning and petrogenetic significance. *Lithos*, 274–275, 188–213. <https://doi.org/10.1016/j.lithos.2016.12.037>
- Clark, R. N. (1999). Spectroscopy of rocks and minerals, and principles of spectroscopy. In *Remote sensing for the earth sciences: Manual of remote sensing, Vol. 3* (pp. 3–58). <https://doi.org/10.1111/j.1945-5100.2004.tb00079.x>
- Clark, R. N., King, T. V. V., Klejwa, M., Swayze, G. A., & Vergo, N. (1990). High spectral resolution reflectance spectroscopy of minerals. *Journal of Geophysical Research*, 95(B8), 12653. <https://doi.org/10.1029/JB095iB08p12653>
- Clark, R. N., Swayze, G. A., Livo, K. E., Kokaly, R. F., Sutley, S. J., Dalton, J. B., McDougal, R. R., & Gent, C. A. (2003). Imaging spectroscopy: Earth and planetary remote sensing with the USGS Tetracorder and expert systems: IMAGING SPECTROSCOPY REMOTE SENSING. *Journal of Geophysical Research: Planets*, 108(E12). <https://doi.org/10.1029/2002JE001847>
- Contreras Acosta, I. C., Khodadadzadeh, M., & Gloaguen, R. (2021). Resolution Enhancement for Drill-Core Hyperspectral Mineral Mapping. *Remote Sensing*, 13(12), 2296. <https://doi.org/10.3390/rs13122296>

- De La Rosa, R., Khodadadzadeh, M., Tusa, L., Kirsch, M., Gisbert, G., Tornos, F., Tolosana-Delgado, R., & Gloaguen, R. (2021). Mineral quantification at deposit scale using drill-core hyperspectral data: A case study in the Iberian Pyrite Belt. *Ore Geology Reviews*, 139, 104514. <https://doi.org/10.1016/j.oregeorev.2021.104514>
- Dieke, G. H. (1968). *Spectra and Energy Levels of Rare Earth Ions in Crystals*. John Wiley and Sons.
- Dieke, G. H., & Crosswhite, H. M. (1963). The Spectra of the Doubly and Triply Ionized Rare Earths. *Appl. Opt.*, 2(7), 675–686. <https://doi.org/10.1364/AO.2.000675>
- Fuchs, M. C., Beyer, J., Lorenz, S., Sharma, S., Renno, A. D., Heitmann, J., & Gloaguen, R. (2021). A spectral library for laser-induced fluorescence analysis as a tool for rare earth element identification. *Earth System Science Data*, 13(9), 4465–4483. <https://doi.org/10.5194/essd-13-4465-2021>
- Gaft, M., Reisfeld, R., & Panczer, G. (2005). *Modern Luminescence Spectroscopy of Minerals and Materials*. Springer.
- Gaft, M., Reisfeld, R., Panczer, G., & Dimova, M. (2008). Time-resolved laser induced luminescence luminescence of uv–vis emission of nd³⁺ in fluorite, scheelite and barite. *J. Alloys Compd.*, 451, 56–61.
- Géring, L., Kirsch, M., Thiele, S., De Lima Ribeiro, A., Gloaguen, R., & Gutzmer, J. (2022). *Spectral characterisation of hydrothermal alteration associated with sediment-hosted Cu-Ag mineralisation in the Central European Kupferschiefer* [Preprint]. Crustal structure and composition/Geochemistry, mineralogy, petrology, and volcanology/Mineralogy. <https://doi.org/10.5194/egusphere-2022-825>
- Goetz, A. F., Vane, G., Soloman, J. E., & Rock, B. N. (1985). Imaging spectrometry for Earth remote sensing. *Science*, 228, 1147.
- Gruner, B. (1990). *Ultramafische und Alkalilamprophyre im Lamprophyr-KarbonatitKomplex von Delitzsch*.
- Hecker, C., Van Ruitenbeek, F. J. A., Bakker, W. H., Fagbohun, B. J., Riley, D., Van Der Werff, H. M. A., & Van Der Meer, F. D. (2019). Mapping the wavelength position of mineral features in hyperspectral thermal infrared data. *International Journal of Applied Earth Observation and Geoinformation*, 79, 133–140. <https://doi.org/10.1016/j.jag.2019.02.013>
- Heinz, D. C. & Chein-I-Chang. (2001). Fully constrained least squares linear spectral mixture analysis method for material quantification in hyperspectral imagery. *IEEE Transactions on Geoscience and Remote Sensing*, 39(3), 529–545. <https://doi.org/10.1109/36.911111>
- Hernandez, E. A., & Filho, C. R. (2013, April). Spectral reflectance and emissivity features of PO₄-bearing carbonatitic rocks from the Catalão I and Tapira complexes: New constraints for

detection of igneous phosphates with remote sensing data. *Anais XVI Simpósio Brasileiro de Sensoriamento Remoto-SBSR*.

- Herrmann, S. (2019). Capacity of imaging spectroscopy for the characterisation of REO, REE bearing minerals and primary REE-deposits [PDF]. *Scientific Technical Report - Data ; 19/08*, 26 MB. <https://doi.org/10.2312/GFZ.B103-19089>
- Hunt, G. R. (1970). Visible and near-infrared spectra of minerals and rocks: I silicate minerals. *Modern Geology*, 1, 283–300.
- Hunt, G. R. (1971). Visible and near-infrared spectra of minerals and rocks: II carbonates. *Modern Geology*, 2, 23–30.
- Hunt, G. R. (1977). SPECTRAL SIGNATURES OF PARTICULATE MINERALS IN THE VISIBLE AND NEAR INFRARED. *GEOPHYSICS*, 42(3), 501–513. <https://doi.org/10.1190/1.1440721>
- Hunt, G. R. (1989). Spectroscopic Properties of Rocks and Minerals. In R. S. Carmichael (Ed.), *Practical Handbook of Physical Properties of Rocks and Minerals* (pp. 599–669). CRC Press.
- Hunt, G. R., & Ashley, R. P. (1979). Spectra of altered rocks in the visible and near infrared. *Economic Geology*, 74(7), 1613–1629. <https://doi.org/10.2113/gsecongeo.74.7.1613>
- Hunt, G. R., Salisbury, J. W., & Lenhoff, C. J. (1972). Visible and near-infrared spectra of minerals and rocks: V. Halides, phosphates, arsenates, vanadates and borates. *Modern Geology*, 3, 121–132.
- Hunt, G. R., Salisbury, J. W., & Lenhoff, C. J. (1973). Visible and near infrared spectra of minerals and rocks. VI. Additional silicates. *Modern Geology*, 4, 85–106.
- Jakob, S., Zimmermann, R., & Gloaguen, R. (2017). The Need for Accurate Geometric and Radiometric Corrections of Drone-Borne Hyperspectral Data for Mineral Exploration: MEPHySTo—A Toolbox for Pre-Processing Drone-Borne Hyperspectral Data. *Remote Sensing*, 9(1), 88. <https://doi.org/10.3390/rs9010088>
- Jones, S., Herrmann, W., & Gemmell, J. B. (2005). Short Wavelength Infrared Spectral Characteristics of the HW Horizon: Implications for Exploration in the Myra Falls Volcanic-Hosted Massive Sulfide Camp, Vancouver Island, British Columbia, Canada. *Economic Geology*, 100(2), 273–294. <https://doi.org/10.2113/gsecongeo.100.2.273>
- Kauppinen, T., Khajehzadeh, N., & Haavisto, O. (2014). Laser-induced fluorescence images and Raman spectroscopy studies on rapid scanning of rock drillcore samples. *International Journal of Mineral Processing*, 132, 26–33. <https://doi.org/10.1016/j.minpro.2014.09.003>
- Khodadadzadeh, M., & Gloaguen, R. (2019). Upscaling High-Resolution Mineralogical Analyses to Estimate Mineral Abundances in Drill Core Hyperspectral Data. *IGARSS 2019 - 2019 IEEE*

International Geoscience and Remote Sensing Symposium, 1845–1848.

<https://doi.org/10.1109/IGARSS.2019.8898441>

Kirillov, A., Mintun, E., Ravi, N., Mao, H., Rolland, C., Gustafson, L., Xiao, T., Whitehead, S., Berg, A. C., Lo, W.-Y., Dollár, P., & Girshick, R. (2023). Segment Anything. *ArXiv:2304.02643*.

Kirsch, M., Lorenz, S., Zimmermann, R., Tusa, L., Möckel, R., Hödl, P., Booyesen, R., Khodadadzadeh, M., & Gloaguen, R. (2018). Integration of terrestrial and drone-borne hyperspectral and photogrammetric sensing methods for exploration mapping and mining monitoring. *Remote Sensing*, *10*(9), 1366.

Koerting, F., Koellner, N., Kuras, A., Boesche, N. K., Rogass, C., Mielke, C., Elger, K., & Altenberger, U. (2021). A solar optical hyperspectral library of rare-earth-bearing minerals, rare-earth oxide powders, copper-bearing minerals and Apliki mine surface samples. *Earth System Science Data*, *13*(3), 923–942. <https://doi.org/10.5194/essd-13-923-2021>

Kokaly, R. F., Clark, R. N., Hoefen, T. M., Livo, K. E., Pearson, N. C., Swayze, G. A., & others. (2017). *USGS Spectral Library Version 7* (1035; Data Series). U.S. Geological Survey. <https://doi.org/10.3133/ds1035>

Kormeier, M., & Miroschnitschenko, W. (1979). *Informationsbericht über das Auftreten einer Seltenen Erden-Mineralisation im Gebiet Delitzsch*.

Krüger, J. C., Romer, R. L., & Kämpf, H. (2013). Late Cretaceous ultramafic lamprophyres and carbonatites from the Delitzsch Complex, Germany. *Chemical Geology*, *353*, 140–150. <https://doi.org/10.1016/j.chemgeo.2012.09.026>

Krupnik, D., & Khan, S. (2019). Close-range, ground-based hyperspectral imaging for mining applications at various scales: Review and case studies. *Earth-Science Reviews*, *198*, 102952.

Kruse, F. A., Bedell, R. L., Taranik, J. V., Peppin, W. A., Weatherbee, O., & Calvin, W. M. (2012). Mapping alteration minerals at prospect, outcrop and drill core scales using imaging spectrometry. *International Journal of Remote Sensing*, *33*(6), 1780–1798. <https://doi.org/10.1080/01431161.2011.600350>

Kruse, F. A., Lefkoff, A. B., Boardman, J. W., Heidebrecht, K. B., Shapiro, A. T., Barloon, P. J., & Goetz, A. F. H. (1993). The spectral image processing system (SIPS)—Interactive visualization and analysis of imaging spectrometer data. *Remote Sensing of Environment*, *44*(2–3), 145–163. [https://doi.org/10.1016/0034-4257\(93\)90013-N](https://doi.org/10.1016/0034-4257(93)90013-N)

Kurz, T. H., Buckley, S. J., & Howell, J. A. (2013). Close-range hyperspectral imaging for geological field studies: Workflow and methods. *International Journal of Remote Sensing*, *34*(5), 1798–1822.

Kwaśny, M., & Bombalska, A. (2022). Applications of Laser-Induced Fluorescence in Medicine. *Sensors*, *22*(8), 2956. <https://doi.org/10.3390/s22082956>

- Laakso, K., Turner, D. J., Rivard, B., & Sánchez-Azofeifa, A. (2019). The long-wave infrared (8-12 μm) spectral features of selected rare earth element—Bearing carbonate, phosphate and silicate minerals. *International Journal of Applied Earth Observation and Geoinformation*, 76, 77–83. <https://doi.org/10.1016/j.jag.2018.11.005>
- Laukamp, C., Rodger, A., LeGras, M., Lampinen, H., Lau, I. C., Pejčić, B., Stromberg, J., Francis, N., & Ramanaidou, E. (2021). Mineral Physicochemistry Underlying Feature-Based Extraction of Mineral Abundance and Composition from Shortwave, Mid and Thermal Infrared Reflectance Spectra. *Minerals*, 11(4), 347. <https://doi.org/10.3390/min11040347>
- Le Maitre, R. W., & International Union of Geological Sciences (Eds.). (2004). *Igneous rocks: A classification and glossary of terms: recommendations of the International Union of Geological Sciences, Subcommittee on the Systematics of Igneous Rocks* (2nd ed). Cambridge University Press.
- Littlefield, E., Calvin, W., Stelling, P., & Kent, T. (2012). Reflectance spectroscopy as a drill core logging technique: An example using core from the Akutan. *Geothermal Resources Council Annual Meeting 2012 - Geothermal: Reliable, Renewable, Global, GRC 2012*, 36(2), 1281–1283.
- Loidolt, C. (2018). *Petrographic characterisation of the Storkwitz carbonatite REE mineralisation for validation of hyperspectral drill core data* [Unpublished M.Sc. thesis]. University of Exeter, Camborne School of Mines.
- Loidolt, C., Zimmermann, R., Tusa, L., Lorenz, S., Ebert, D., Gloaguen, R., & Broom-Fendley, S. (2022). New Insights into the Rare Earth Element Mineralization of the Storkwitz Carbonatite, Germany. *The Canadian Mineralogist*, 60(6), 913–932. <https://doi.org/10.3749/canmin.2100061>
- Lorenz, S., Beyer, J., Fuchs, M., Seidel, P., Turner, D., Heitmann, J., & Gloaguen, R. (2018). The Potential of Reflectance and Laser Induced Luminescence Spectroscopy for Near-Field Rare Earth Element Detection in Mineral Exploration. *Remote Sensing*, 11(1), 21. <https://doi.org/10.3390/rs11010021>
- Michelsburg, M., & León, F. P. (2018). Spectral and spatial unmixing for material recognition in sorting plants. *Of Materials*, 179.
- Möckel, F. (2015). *Der Karbonatit-Komplex Delitzsch*.
- Müller, S., Meima, J. A., & Rammlmair, D. (2021). Detecting REE-rich areas in heterogeneous drill cores from Storkwitz using LIBS and a combination of k-means clustering and spatial raster analysis. *Journal of Geochemical Exploration*, 221, 106697. <https://doi.org/10.1016/j.gexplo.2020.106697>
- Murad, E., & Bishop, J. L. (2005). The visible and infrared spectral properties of jarosite and alunite. *American Mineralogist*, 90(7), 1100–1107. <https://doi.org/10.2138/am.2005.1700>

- Muraoka, K., & Maeda, M. (1993). Application of laser-induced fluorescence to high-temperature plasmas. *Plasma Physics and Controlled Fusion*, 35(6), 633.
- Neave, D. A., Black, M., Riley, T. R., Gibson, S. A., Ferrier, G., Wall, F., & Broom-Fendley, S. (2016). On the Feasibility of Imaging Carbonatite-Hosted Rare Earth Element Deposits Using Remote Sensing. *Economic Geology*, 111(3), 641–665.
<https://doi.org/10.2113/econgeo.111.3.641>
- Niegisch, M., Kamradt, A., & Borg, G. (2020a). Geochemical and mineralogical characterisation of the REE-mineralisation in the upper zone of the Storkwitz Carbonatite Complex from drill core SES1/2021. *Geoprofilheft Des LfULG, Heft 15/2020*.
- Niegisch, M., Kamradt, A., & Borg, G. (2020b). *The Upper Zone of the Storkwitz Carbonatite: Geochemical and Mineralogical Characterization of the REE-mineralisation in the Upper Zone of the Storkwitz Carbonatite Complex from Drill Core SES-1/2012*. Sächsisches Landesamt für Umwelt und Geologie. <https://books.google.co.uk/books?id=EZ0lzgEACAAJ>
- Nienhaus, K., & Bayer, A. K. (2003). Innovative systems for horizon control of mining machines by means of laser induced fluorescence (lif). *Mine Planning and Equipment Selection*, 1–7.
- Pejčić, B., Shelton, T., LeGras, M., Laukamp, C., Francis, N., & Lau, I. (2022). *Mid Infrared Spectral Reference Library* [dataset]. CSIRO. <https://doi.org/10.25919/E11N-Q040>
- Pontual, S., Merry, N., & Gamson, P. (1997). G-Mex Volume 1: Special interpretation field manual. *Ausspec International, Kew*, 55p.
- Reisfeld, R., Gaft, M., Boulon, G., Panczer, G., & Jørgensen, C. K. (1996). Laser-induced luminescence of rare-earth elements in natural fluorapatites. *J. Lumin.*, 69, 343–353.
- Rencz, Andrew. N. (1998). *Manual of remote sensing* (R. A. Ryerson & American Society for Photogrammetry and Remote Sensing, Eds.; 3rd. ed). J. Wiley.
- Röllig, G., Viehweg, M., & Reuter, N. (1990). The ultramafic lamprophyres and carbonatites of Delitzsch /GDR. *Zeitschrift f"ur Angewandte Geologie*, 36, 49–54.
- Rowan, L. C., Kingston, M. J., & Crowley, J. K. (1986). Spectral reflectance of carbonatites and related alkalic igneous rocks; selected samples from four North American localities. *Economic Geology*, 81(4), 857–871. <https://doi.org/10.2113/gsecongeo.81.4.857>
- Rowan, L. C., & Mars, J. C. (2003). Lithologic mapping in the Mountain Pass, California area using advanced spaceborne thermal emission and reflection radiometer (ASTER) data. *Remote Sensing of Environment*, 84, 350–366.
- Salisbury, J. W., Walter, L. S., & Vergo, N. (1987). *Mid-Infrared (2.1-25 μm) Spectra of Minerals* (Open-File Report 87–263). U.S. Geological Survey. <https://doi.org/10.3133/ofr87263>

- Saputra, D. M., Saputra, D., & Oswari, L. D. (2020). Effect of Distance Metrics in Determining K-Value in K-Means Clustering Using Elbow and Silhouette Method. *Proceedings of the Sriwijaya International Conference on Information Technology and Its Applications (SICONIAN 2019)*.
- Sriwijaya International Conference on Information Technology and Its Applications (SICONIAN 2019), Palembang, Indonesia. <https://doi.org/10.2991/aisr.k.200424.051>
- Savitri, K. P., Hecker, C., Van Der Meer, F. D., & Sidik, R. P. (2021). VNIR-SWIR infrared (imaging) spectroscopy for geothermal exploration: Current status and future directions. *Geothermics*, 96, 102178. <https://doi.org/10.1016/j.geothermics.2021.102178>
- Savitzky, Abraham., & Golay, M. J. E. (1964). Smoothing and Differentiation of Data by Simplified Least Squares Procedures. *Analytical Chemistry*, 36(8), 1627–1639. <https://doi.org/10.1021/ac60214a047>
- Schodlok, M. C., Green, A., & Huntington, J. (2016). A reference library of thermal infrared mineral reflectance spectra for the HyLogger-3 drill core logging system. *Australian Journal of Earth Sciences*, 1–9. <https://doi.org/10.1080/08120099.2016.1234508>
- Seidel, P., Lorenz, S., Heinig, T., Zimmermann, R., Booyens, R., Beyer, J., Heitmann, J., & Gloaguen, R. (2019). Fast 2D Laser-Induced Fluorescence Spectroscopy Mapping of Rare Earth Elements in Rock Samples. *Sensors*, 19(10), 2219. <https://doi.org/10.3390/s19102219>
- Seifert, W., Kämpf, H., & Wasternack, J. (2000). Compositional variation in apatite, phlogopite and other accessory minerals of the ultramafic Delitzsch complex, Germany: Implication for cooling history of carbonatites. *Lithos*, 53(2), 81–100. [https://doi.org/10.1016/S0024-4937\(00\)00010-4](https://doi.org/10.1016/S0024-4937(00)00010-4)
- Shahapure, K. R., & Nicholas, C. (2020). Cluster Quality Analysis Using Silhouette Score. *2020 IEEE 7th International Conference on Data Science and Advanced Analytics (DSAA)*, 747–748. <https://doi.org/10.1109/DSAA49011.2020.00096>
- Simandl, G. J., & Paradis, S. (2018). Carbonatites: Related ore deposits, resources, footprint, and exploration methods. *Applied Earth Science*, 127(4), 123–152. <https://doi.org/10.1080/25726838.2018.1516935>
- Snyder, C. J., Khan, S. D., Bhattacharya, J. P., Glennie, C., & Seepersad, D. (2016). Thin-bedded reservoir analogs in an ancient delta using terrestrial laser scanner and high-resolution ground-based hyperspectral cameras. *Sedimentary Geology*, 342, 154–164.
- Syakur, M. A., Khotimah, B. K., Rochman, E. M. S., & Satoto, B. D. (2018). Integration K-Means Clustering Method and Elbow Method For Identification of The Best Customer Profile Cluster. *IOP Conference Series: Materials Science and Engineering*, 336, 012017. <https://doi.org/10.1088/1757-899X/336/1/012017>

- Thiele, S. T., Bnoukacem, Z., Lorenz, S., Bordenave, A., Menegoni, N., Madriz, Y., Dujoncquoy, E., Gloaguen, R., & Kenter, J. (2021b). Mineralogical Mapping with Accurately Corrected Shortwave Infrared Hyperspectral Data Acquired Obliquely from UAVs. *Remote Sensing*, *14*(1), 5. <https://doi.org/10.3390/rs14010005>
- Thiele, S. T., Lorenz, S., Kirsch, M., Cecilia Contreras Acosta, I., Tusa, L., Herrmann, E., Möckel, R., & Gloaguen, R. (2021a). Multi-scale, multi-sensor data integration for automated 3-D geological mapping. *Ore Geology Reviews*, *136*, 104252. <https://doi.org/10.1016/j.oregeorev.2021.104252>
- Turner, D. J. (2015). *Reflectance spectroscopy and imaging spectroscopy of rare earth element-bearing mineral and rock samples* [PhD Thesis]. University of British Columbia.
- Turner, D. J., Rivard, B., & Groat, L. A. (2014). Visible and short-wave infrared reflectance spectroscopy of REE fluorocarbonates. *American Mineralogist*, *99*(7), 1335–1346. <https://doi.org/10.2138/am.2014.4674>
- Turner, D. J., Rivard, B., & Groat, L. A. (2016). Visible and short-wave infrared reflectance spectroscopy of REE phosphate minerals. *American Mineralogist*, *101*(10), 2264–2278. <https://doi.org/10.2138/am-2016-5692>
- Tuşa, L., Khodadadzadeh, M., Contreras, C., Rafiezadeh Shahi, K., Fuchs, M., Gloaguen, R., & Gutzmer, J. (2020). Drill-Core Mineral Abundance Estimation Using Hyperspectral and High-Resolution Mineralogical Data. *Remote Sensing*, *12*(7), 1218. <https://doi.org/10.3390/rs12071218>
- V. Kale, K., M. Solankar, M., & B. Nalawade, D. (2020). Hyperspectral Endmember Extraction Techniques. In J. Chen, Y. Song, & H. Li (Eds.), *Processing and Analysis of Hyperspectral Data*. IntechOpen. <https://doi.org/10.5772/intechopen.88910>
- Van Der Meer, F. (2004). Analysis of spectral absorption features in hyperspectral imagery. *International Journal of Applied Earth Observation and Geoinformation*, *5*(1), 55–68. <https://doi.org/10.1016/j.jag.2003.09.001>
- Van Der Meer, F., Kopačková, V., Koucká, L., Van Der Werff, H. M. A., Van Ruitenbeek, F. J. A., & Bakker, W. H. (2018). Wavelength feature mapping as a proxy to mineral chemistry for investigating geologic systems: An example from the Rodalquilar epithermal system. *International Journal of Applied Earth Observation and Geoinformation*, *64*, 237–248. <https://doi.org/10.1016/j.jag.2017.09.008>
- Van Ruitenbeek, F. J. A., Bakker, W. H., Van Der Werff, H. M. A., Zegers, T. E., Oosthoek, J. H. P., Omer, Z. A., Marsh, S. H., & Van Der Meer, F. D. (2014). Mapping the wavelength position of deepest absorption features to explore mineral diversity in hyperspectral images. *Planetary and Space Science*, *101*, 108–117. <https://doi.org/10.1016/j.pss.2014.06.009>
- Wagner, G. A., Coyle, D. A., Duyster, J., Henjes-Kunst, F., Peterek, A., Schroder, B., Stockhert, B., Wemmer, K., Zulauf, G., & Ahrendt, H. (1997). Post-Variscan thermal and tectonic evolution of

the KTB site and its surroundings. *Journal of Geophysical Research – Solid Earth*, 102(B8), 18221–18232. <https://doi.org/10.1029/96JB02565>

Waychunas, G. A. (1988). Luminescence, X-ray emission and new spectroscopies. In F. C. Hawthorne (Ed.), *Spectroscopic Methods in Mineralogy and Geology* (Vol. 18, pp. 639–698). Mineralogical Society of America.

Whitney, D. L., & Evans, B. W. (2010). Abbreviations for names of rock-forming minerals. *American Mineralogist*, 95(1), 185–187. <https://doi.org/10.2138/am.2010.3371>

Winter, M. E. (1999). *N-FINDR: An algorithm for fast autonomous spectral end-member determination in hyperspectral data* (M. R. Descour & S. S. Shen, Eds.; pp. 266–275). <https://doi.org/10.1117/12.366289>

Wulf, J. S., Rühmann, S., Rego, I., Puhl, I., Treutter, D., & Zude, M. (2008). Nondestructive Application of Laser-Induced Fluorescence Spectroscopy for Quantitative Analyses of Phenolic Compounds in Strawberry Fruits (*Fragaria x ananassa*). *Journal of Agricultural and Food Chemistry*, 56(9), 2875–2882. <https://doi.org/10.1021/jf072495i>

Yitagesu, F. A., Van Der Meer, F., Van Der Werff, H., & Hecker, C. (2011). Spectral characteristics of clay minerals in the 2.5–14 μ m wavelength region. *Applied Clay Science*, 53(4), 581–591. <https://doi.org/10.1016/j.clay.2011.05.007>

Zhang, X., Tong, X., & Liu, M. (2009). An improved N-FINDR algorithm for endmember extraction in hyperspectral imagery. *2009 Joint Urban Remote Sensing Event*, 1–5. <https://doi.org/10.1109/URS.2009.5137677>

Zimmermann, R., Brandmeier, M., Andreani, L., Mhopjeni, K., & Gloaguen, R. (2016). Remote Sensing Exploration of Nb-Ta-LREE-Enriched Carbonatite (Epembe/Namibia). *Remote Sensing*, 8(8), 620. <https://doi.org/10.3390/rs8080620>